Eidgenössische Technische Hochschule Zürich
Swiss Federal Institute of Technology Zurich

DEPARTMENT OF INFORMATION ENGINEERING
UNIVERSITY OF PADOVA

IIS Integrated Systems Laboratories & DEI Department of Information Engineering

Modeling, Development, and Testing of an Integral Dose Calorimeter for the Characterization of Electron Beam Crosslinking Processes in Industrial Environment

Supervisor UNIPD: Prof. Gaudenzio Meneghesso

Supervisor ETHZ: Dr. Mauro Ciappa, Dipl. Phys. Luigi Mangiacapra

Master Student: Alexandra Lupi

Matriculation Number: 601512 – IL

Master Degree in Electrical Engineering

Academic Year 2009-2010

ETH
Eidgenössische Technische Hochschule Zürich
Swiss Federal Institute of Technology Zurich

Institut für Integrierte Systeme
Integrated Systems Laboratory

Diplomarbeit im Studiengang
Elektrotechnik und Informationstechnologie
Frühling 2010

für

Alexandra LUPI
Erasmus student (University of Padova, Italy)

Modeling, Development, and Testing of an Integral Dose Calorimeter for the Characterizationof Electron Beam Crosslinking Processes in Industrial Environment

Supervisor ETHZ: Dr. Mauro Ciappa, Dipl. Phys. Luigi Mangiacapra
Supervisor UNIPD: Prof. Gaudenzio Meneghesso, University of Padova

Ausgabe: February 22, 2010
Abgabe: August 27, 2010

I. Introduction

One among the main challenges in electron beam processing of polymers is the set up the ideal irradiation conditions to deliver a uniform dose in the isolation layer of cables and thus to obtain the best degree of polymer crosslinking, which satisfy the required specifications. At the IIS, this problem is solved by three-dimensional Monte Carlo simulation.

Together with the accelerator geometry, electron beam energy is one of the main parameters that affect the final dose uniformity. During processing, cables are span through dedicated conveyors and pass several times across the irradiation field in different positions and fluence values. This involves several irradiations with different spatial dose distributions. For a fine dose calculation, the simulation has to be subdivided into multiple steps to reproduce the real geometry. Then, all contributions are added to obtain the spatial distribution of the cumulated dose. For this scope, a three-dimensional Monte Carlo simulation flow is used to calculate automatically the cumulated dose distribution for accelerator geometries of whatever complexity.

An iterative procedure have been already developed to calculate the beam energy for optimum dose uniformity. As usual in Monte Carlo simulations, the calculation time can become a relevant issue, unless proper parallelization schemes are used, which make possible to produce a solution within some few minutes.

In this framework, a major challenge is the calibration of Monte Carlo models by suitable experimental procedures.

II. Purpose

The present master thesis work consists of a first part, where an integral dose calorimeter has to be designed and manufactured, and of a second part, where the calorimeter is used in an industrial plant to measure the average energy of the electrons imping at the surface of the target.

In the first part, the material (e.g. C, Cu, Al H_2O, Polyethylene), the size, and the time constant of the calorimeter has to be optimized on the base of transient thermal (Ansys Workbench 14.0) and dose deposition (EBXLINK 1D/3D) simulations. A design has to be chosen that minimizes the heat losses and the electron energy absorption through the barrier layers. The sources of systematic errors have to be identified and procedures to correct the measurement developed accordingly. The overall measurement error after correction of the systematic contribution has to be less than 1%. The temperature acquisition system (datalogger, acquisition software, temperature sensor) has to be configured to cope with these specifications. Drawings have to be available as in a suitable form in order to be manufactured at the D-ITET workshop.

In the second part, measurements will be perfomed at an industrial plant, with the scope to assess the performance of the developed system. Cables and electronic systems have to be shielded properly in order to avoid degration through the ambient radiation (high energy electrons, X-rays). The obtained data have to processed and represented according to the standard protocols.

III. Tasks

The task breakdown of present Thesis work is as follows:

1. Get acquainted with the thermal simulator Ansys Workbench 14.0 and with EBXLINX1D/3D. Calculate the time to the steady-state for different materials (eventually by using also compact thermal models), geometries based on realistic dose distributions in the absorber.
2. Optimize the system design, in particular taking into account
    a. Package
    b. Absorber (material, geometry)
    c. Thermal isolation
    d. Select datalogger and related control software
    e. Select temperature sensor
    f. Conceive a dedicated forced convection system in the case of the water calorimeter
3. Prepare drawings to be forwarded to the mechanical workshop
4. Assembly and testing of the calorimeter
5. Identify and quantify systematic (to be corrected) and random error sourc
6. Develop the control software for the temperature acquisition system and find an accurate mathematical expression to convert the resistance value into temperature for the temperature sensor.
7. Plan, prepare, and execute two measurements campaign at a remote industrial site.
8. Process and discuss the experimental results
9. Writing of the Thesis

IV. Detailed Specifications

1. Integral Dose Calorimeter (non-standard)
2. Low Energy Range 0.5 – 2 MeV (usually over 4 MeV)
3. Overall Accuracy ± 1%
4. Typical Time Constant < 1 second
5. Remote PC Control (Operated within Shelter)
6. Use Tabulated Cp Data
7. Radiation Resistant (1000 kGy at 100 kGy/s)
8. Overall Thickness: 30 mm
9. Lateral Width: typ. 10 – 15 cm

V. Report and Presentation

The research activity and its results will be documented in a final report (2 copies for IIS). The contents of this report will be the topic of an oral presentation to be held at ETHZ. The receipt of the Thesis is acknowledged once the laboratory and the building keys are returned to the ETZ housekeeping manager.

Zürich, August 2010

Prof. Wolfgang Fichtner

Dr. Mauro Ciappa

Table of contents

Abstract

This work deals with the design and manufacture of an Integral Dose Calorimeter for the determination of the average electron beam energy in an industrial electron accelerator which is used for polymers crosslinking processes.

The whole project can be divided into two parts: modeling through simulations and experimental tests in industrial plant for the determination of the average energy of the electrons impinging at the surface of the target.

In the first phase the thermal, geometry, timing characteristics, and specifications of the calorimeter through simulation tools such as ANSYS Workbench 12.1 and EBXLINK 1D/3D for Monte Carlo simulations are carried out.

A proper design to minimize heat losses and the electron energy absorption through barrier layers is needed. The sources of systematic and random errors have been identified in order to correct the experimental measurements. The temperature acquisition system has been configured through a high resolution NTC thermistor and a data-logger with a remote PC-control given by LabVIEW SignalExpress interface. The developed system has 1% precision of the measured energy.

In the second phase the device has been tested in an industrial plant, verifying good agreement for the designed system and excellent performance in the electron beam energy measurements.

Sommario

Questo lavoro di tesi tratta in modo approfondito della progettazione e della realizzazione di un Calorimetro a Dose Integrale per la determinazione dell'energia media degli elettroni in un acceleratore di elettroni per la reticolazione di polimeri.

Il progetto consta principalmente di una parte dedicata all'ingegnerizzazione del calorimetro mediante tecniche simulative e di una seconda parte volta a caratterizzare sperimentalmente il dispositivo realizzato.

La prima fase prevede l'analisi e lo studio delle caratteristiche termiche e geometriche, delle costanti di tempo e delle specifiche del calorimetro. La modellizzazione è stata basata su strumenti standard (ANSYS Workbench 12.1, modelli termici compatti) e dedicati (EBXLINK 1D/3D).

Questa prima fase ha permesso di progettare un sistema che minimizzi la dispersione del calore depositato nel calorimetro e l'assorbimento degli elettroni incidenti sulle barriere termiche. Sono state inoltre identificate e quantificate le sorgenti degli errori sistematici e statistici per la correzione dei dati sperimentali. Il sistema di acquisizione della temperatura è stato realizzato con un sensore NTC ad alta risoluzione, congiuntamente ad un data-logger veloce pilotato in remoto con un'interfaccia programmata in LabVIEW SignalExpress. Il sistema così ottenuto presenta una precisione intrinseca dell'ordine dell'uno per cento dell'energia misurata.

Durante la seconda fase si sono verificate sperimentalmente le caratteristiche del calorimetro in ambiente industriale, constatandone un corretto funzionamento ed un'ottima precisione nell'acquisizione dell'energia del fascio elettronico.

Introduction

Radiation Dosimetry is a physical science, whose main aim is to evaluate the energy deposed on matter by radiation. One of most reliable and most common radiation measurement of all standard dosimetric methods is Calorimetry. This technique is basically employed in the determination of the Absorbed Dose in a small volume of an irradiated medium called absorber through its temperature increase.

In recent theses Dosimetry and Calorimetry are used for industrial applications, in particular for cables and wires crosslinking processes. Polymer crosslinking strongly depends on the deposited dose, which has to be optimized in order to obtain an improvement of: mechanical properties, lifetime, and reliability of the irradiated items.

Radiation sources in electron beam crosslinking are usually electrostatic accelerators, whose working conditions depend on the applications. Typical values for the crosslinking of cables and wires are $0.5 - 3\ MeV$ electron beam energy, up to $100\ mA$ beam current, and $50 - 100\ kW$ power.

Since a calorimeter has to be designed, all relevant components have to be identified and quantified. In particular, the calorimeter to be designed is intended to measure the average electron beam energy. In addition, the calorimeter will enable the user to quantitatively assess the behavior and performances of the accelerator.

This work, which is divided into five chapters, describes the modeling, development, and testing activities of a dedicated integral dose calorimeter.

Motivations and novelty of the approach are presented in the first chapter focusing on the necessity of an integral dose calorimeter.

The second chapter deals with the specifications of the absorber, whose chemical composition, thermal characteristics, and geometry are optimized on the base of transient thermal simulations carried out by ANSYS Workbench 12.1 simulation tool.

In the third chapter, 1D and 3D Monte Carlo dose simulation is used to quantitatively predict the response of the system.

Chapter four presents the final layout of the system, including the calorimeter itself, the temperature measurement, and the data acquisition flow. This is completed by the identification of the main sources of systematic and random experimental errors and the development of procedure for their correction.

Finally, chapter five is devoted to experimental measurement carried out under industrial conditions, as well as to the analysis and discussion of the experimental data.

Chapter 1 – Motivation and Novelty of the Work

Basic principles of heat transfer processes

The accuracy of the design of calorimeters strongly depends on knowledge of the mechanisms of heat transfer within and outside the absorber, on the definition of the relation between temperature increase and dose deposition, and on the technique of temperature used for the measurement of the instantaneous temperature of the absorber.

As in this work we have to carry out a thermal analysis of the calorimeter, it is useful to give a brief overview of heat transfer processes.

Heat transfer is a physical process [1], which involves the flow of energy due to the existence of a temperature gradient. Heat flows by three distinct mechanisms or modes, namely Conduction, Convection, and Radiation. Most real world heat transfer problems involve a combination of these mechanisms and the degree to which heat flows by each of these mechanisms is problem dependent. For example radiation heat transfer generally involves elevated temperature differences and in many common engineering problems the amount of heat transfer by radiation is negligible and can be safely ignored, so that one heat mechanism appears the most relevant than the others. This is not the case of present calorimeter.

Summarizing:

Conduction occurs inside a solid body from the high temperature region to the low temperature region.

Convection occurs when heat is transferred by movement of a heated fluid such as air or water.

Radiation occurs between a body and the surroundings without the presence of a medium.

Conduction

Conduction or heat flow in a solid body is governed by Fourier's law, which states that "The rate of heat flow per unit area in a solid is proportional to the temperature gradient in the direction normal to the heat flow", that can be mathematically expressed by (1).

$$\dot{q} = -k\frac{dT}{dx} \Rightarrow q = -kA\frac{\Delta T}{\Delta x} \quad (1)$$

where $\dot{q}$ is the heat flux $\left[\frac{W}{m^2}\right]$, q is the heat transfer rate $[W]$, k is thermal conductivity $\left[\frac{W}{m \cdot K}\right]$, and A is the surface area $[m^2]$.

Convection

Convection is the exchange of heat between a surface and the surrounding fluid, which is mathematically expressed by (2).

$$q = hA(T_w - T_a) \quad (2)$$

where q is the heat transfer rate $[W]$, h is the convection heat transfer coefficient $\left[\frac{W}{m^2 \cdot K}\right]$, A is the surface area $[m^2]$, T_w is the surface temperature $[K]$, and T_a is the ambient fluid temperature $[K]$.

Convection heat transfer can occur as natural, also referred to as free convection, or forced convection.

Natural convection occurs when the fluid is originally stationary and heat transfer to it causes it to expand and rise (if heat is removed from the fluid, the opposite situation occurs and the removal of heat from the fluid results in its contraction and increase in density). The decrease in the density of the fluid adjacent to the surface where the heat transfer occurs induces a natural motion whereby the heated fluid rises and is replaced by a fluid initially unaffected by the heat transfer process. This process induces a motion in the fluid adjacent to a solid body called natural or free convection.

Forced convection refers to situations where a fan or other means are used to cause the fluid to flow over a solid surface. The fluid exchanges heat with the solid surface as it flows over it, lowering or increasing the temperature of the fluid.

Radiation

Radiation heat exchange occurs between the surface of a body and the atmosphere and objects not in contact with the radiating body. The situation where a body with a surface temperature T_w is exchanging heat via radiation with the environment at T_a is shown with the equation (3):

$$q = \varepsilon\sigma A(T_w^4 - T_a^4) \qquad (3)$$

where q is the heat transfer rate $[W]$, ε is the emissivity, σ is Stefan Boltzmann constant $\left[\frac{W}{m^2 \cdot K^4}\right]$, A is the surface area $[m^2]$, T is the temperature $[K]$.

In present calorimeter, a corresponding countermeasure is considered for each heat transfer mechanism. In particular, an insulation layer is needed (expanded polystyrene) to limit the conduction, which takes place at the interface between absorber and the surrounding body of the calorimeter. Heat losses though convection that takes place mainly at the top surface of the absorber are eliminated by a barrier layer (mylar foil) at the calorimeter surface. Finally, heat losses through radiations from the absorber towards the surrounding environment are minimized by the use of an infra-red reflecting layer (aluminized mylar foil).

Radiation Dosimetry

Radiation Dosimetry is a physical science, which originates in the medical application of ionizing radiation, whose main purpose is to determine the radiation energy deposed in matter.

A very large field of application is certainly the clinical one (biological effects of radiation on tissues), but also in the industrial environment a lot of effort is made for different purposes. In fact in the industrial field one of the most important aims is to find out the effects of radiation in polymers because of the property of molecules crosslinking, where cross-links are bonds that link one polymer chain to another, so that a difference in the polymers physical properties is promoted. The cross-links can be formed by chemical reactions that are initiated by heat, pressure, or radiation. For example the more a polymer is irradiated, the more the crosslinking process is activated, in a way that the polymer network becomes stronger and more resistant, improving: mechanical properties, lifetime and reliability.

The word Dosimetry holds the meaning of the whole process of interaction between radiation and matter. The Dosimetry reference measure is the Absorbed Dose; its measure unit is Gray [Gy], whose name was given by the British physicist Hal Gray. Absorbed Dose identifies the energy deposed in a medium by ionizing radiation. One Gray deposits one Joule of energy in one kilogram of irradiated matter, mathematically expressed in equation (4):

$$1\ Gy = \frac{1\ J}{1\ kg} \qquad (4)$$

The usual dose absorption for industrial crosslinking processes is in $150 - 200\ kGy$ range (electron deposed dose), while for nuclear medicine, for instance for a thorax x-ray, the absorbed dose value is $0.1\ mGy$ (x-ray deposed dose). Comparing these two absorbed dose values we can observe that they differ in 6 orders of magnitude, so that a crosslinking process corresponds to two millions thorax x-rays.

Principles of Calorimetry

According to [2] Calorimetry is a basic method for the determination of the Absorbed Dose in a small volume of an irradiated medium. The radiation source considered in this thesis is an electron beam, whose acceleration energy can be set in the range from $0.5 - 3\ MeV$ and the beam current up to $70\ mA$.

The basic structure of a calorimeter is quite simple [3]. The system consists of three parts: the absorber, the temperature sensor with wiring, and the thermal insulation. The scope of the absorber, in which a temperature sensor is embedded, is to absorb the incident radiation and to convert it into heat possibly without losses. The temperature sensor can be a thermistor, a thermocouple, or a platinum resistance, that is supposed to detect the temperature rise in the absorber in conjunction with an accurate A/D converter coupled with a high-speed datalogger. Finally, the insulation material (usually plastic foam), which holds the role of envelope, also works as package of the system. In this respect, the shape of the isolation has to be chosen in such a way that it does not interfere with a correct temperature measurement. This is especially critical in the case of beam energies below 4 MeV.

The temperature of the absorber is detected both during irradiation, before and after irradiation. Furthermore, the instantaneous temperature of the absorber is influenced by the heat losses by the different mechanisms. This results into a time-dependent temperature level, which needs to be properly modeled and corrected.

Referring to [4], the fundamental relation of the average Absorbed Dose D $[Gy]$ in the calorimeter absorber is given by (5):

$$D = \frac{E}{m} \qquad (5)$$

where E is the energy absorbed in the calorimeter body $[J]$, and m is its mass $[kg]$. Assuming that all absorbed energy E is converted into heat, the temperature rise ΔT $[K]$ produced as a consequence of the E energy absorption is given by equation (6).

$$\Delta T = \frac{E}{m \cdot C_p} \qquad (6)$$

where C_p $\left[\frac{J}{kg \cdot K}\right]$ is the specific heat capacity of the calorimeter body material, i.e. the amount of energy required to raise 1 kg of material by the temperature of 1 K.

Thus the absorbed dose D can be calculated as the product of the temperature increase ΔT and the specific heat capacity C_p of the absorber, as shown in (7).

(7)

$$D = C_p \cdot \Delta T$$

However, in practice, equation (7) is only a starting point, because the radiation processing involves the heat transfer to and from the surroundings and different interactions among particles and matter (i.e. electron back-scattering, bremsstrahlung, secondary electrons emission). Further, the C_p value is often a function of temperature for many absorber materials, and the knowledge of this function may provide useful information when the calibration function of a calorimeter is evaluated.

Application of Standard Calorimetry Techniques

Calorimeters for measurements of absorbed dose have been constructed for a wide range of applications [2] and the materials used for the calorimeter absorbers have been chosen among different substances.

The traditional approach towards calorimeters, described in [3], consists of designing the absorber thickness less than the range of the irradiating electrons, typically not exceeding $1/3$ of the electron range for a specified material. This fact limits the variation of the dose gradients within the calorimetric body. This thin design is mandatory for the standard calorimetry application, as in the fine calorimetric body, the absorbed dose may be assumed to be constant. Consequently it can be achieved the initial absorbed dose value in the normalized absorbed dose curve.

Calorimeters have been employed to measure the activity of radioactive sources and to calibrate radiation chemical reaction yields [5]. Thus suitably designed calorimeters used for these purposes have the fundamental merit that they directly measure energy deposition. This fact obviously constitutes a primary advantage over other dosimetric methods that utilize secondary processes. Such methods require conversion factors that rest on physical interpretation of the absorption processes and involve such consideration as: geometry, dose rates, relative stopping power, incident radiation spectrum, local secondary electron spectrum, atomic number, and density.

In the design of a calorimeter the geometry and the composition of its elements are determined and are greatly limited by the features of absorption processes.

Industrial Accelerators

In Figure 1 a sketch of an industrial electron accelerator is drawn.

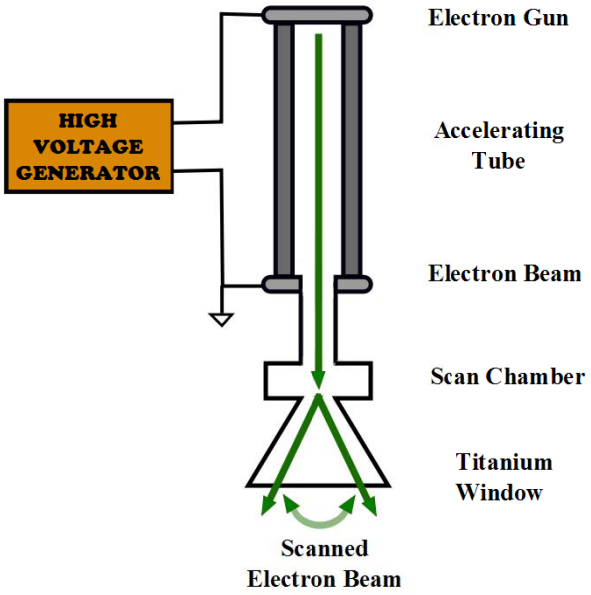

Figure 1 – Sketch of an industrial electron accelerator. In the plot are represented the most important accelerator parts. In green color is drawn the electron beam that is scanned through the scan chamber by a magnet and that is spread over the titanium window.

As we can observe in Figure 1, the high voltage generator provides an adequate voltage supply to produce accelerated electrons through thermionic emission. The accelerated electrons run through the accelerating tube, where at the end of it they are focused for building the electron beam. Afterwards there is a magnet in the scan chamber, whose usual working frequency is between and , that has the important function to scan the electrons over the titanium window. At the end of the entire system the spread electrons determine the final particle radiation. The whole inner system is in vacuum conditions.

The accelerator we deal with has a $40\ \mu m$ titanium scanner window and the scanning area is $120 \times 4.5 = 540\ cm^2$. During the crossliking processes cables pass under the electron beam at a speed of several m/s, while our calorimeter will be passing under the accelerator window at about $18\ cm$ distance, set on a conveyor with a constant speed of 3.3 $\frac{m}{min}$, that is 5.5 $\frac{cm}{s}$.

Simulation Tool: ANSYS Workbench 12.1

Engineers routinely use Solid Modelers together with the Finite Element Method (FEM) to solve everyday problems of modeling for form/fit/function, stress deformation, heat transfer, fluid flow, electromagnetic, etc. using commercial as well as special purpose software. ANSYS Workbench is one of the most versatile and widely used of the commercial solid modeling, simulation and optimization programs, as we can see in [1].

Finite element analysis, on which ANSYS WB is based on, is a computer-based numerical technique that is used to solve stress analysis, heat transfer, fluid flow and other types of engineering problems. It is based on solving a system of equations that describe some parameters over the domain of a continuous physical system. The real power of the finite element method lies in its ability of analyzing physical parts that are of any shape or size having arbitrarily located loads and supports.

As the name implies, finite element analysis involves the partitioning (also called discretizing) of a structure into a finite number of elements. Elements are connected to one another at their corner points. These corner points are called nodes or nodal points. Each element is a simple geometric shape, such as a triangle or a quadrilateral. Being a standard shape (triangle, quadrilateral) facilitate the development of the governing equations that relate to displacement and stress behavior within the element.

In order to completely determine a finite element model, nodal points, elements, loads, supports and element related data (such as material properties) must be defined. Once these data have been defined, they are submitted to a finite element program for the actual computational process. The program then formulates a set of simultaneous equations, which

are the equilibrium equations corresponding to each degree of freedom (directions in which movement can occur) at each nodal point. A nodal point can have up to six degrees of freedom – translation in the x, y and z directions and rotation about each of these axes.

In ANSYS WB there are a lot of useful applications, but, as the use of this software has the aim to perform thermal simulations, only the Design Modeler – to sketch the geometric model – and the Mechanical Simulation – which performs the thermal simulation – are relevant functions for the considered system.

Thermal Analysis in ANSYS Workbench

A thermal analysis calculates the temperature distribution and related thermal quantities in a system or component. Typical thermal quantities of interest are:

- Temperature distributions;
- Amount of lost or gained heat;
- Thermal gradients;
- Thermal fluxes.

The first step in setting a thermal analysis is to understand whether the simulation loads vary over time or not. If the imposed magnitudes are kept constant, the analysis that should be selected is the steady-state one; otherwise the transient thermal is needed. ANSYS WB supports both steady-state and transient analyses, which are briefly described in the following paragraphs. We have to specify that the first approach towards the resolution of the thermal problem has been of steady-state type. But, to give the simulations a more realistic view and to reproduce the physical aspects of the electron beam (source of irradiation in the experiment), the final run simulations are of transient thermal type. In the end we need transient thermal simulations, as the calorimeter does not have a fixed position, in facts it is moved past the electron beam window by a conveyor, so that we can think that the calorimeter moves with a constant speed (3.3 $\frac{m}{min}$ or 5.5 $\frac{cm}{s}$).

Steady-State Thermal Analysis

A steady-state thermal analysis calculates the effects of steady thermal loads on a system or on a component. Engineers and analysts often perform a steady-state analysis before doing a transient thermal one, to help establish initial conditions.

A steady-state thermal analysis can be used to determine temperatures, thermal gradients, heat flow rates and heat fluxes in an object. All these properties are caused by thermal loads that do not vary over time. Such loads include the following:

- Convection;
- Radiation
- Heat flow rate;
- Heat flux (heat flow per unit area);
- Heat generation rate (heat flow per unit volume).

A steady-state thermal analysis may be either linear, with constant material properties, or nonlinear, with material properties that depend on temperature.

Transient Thermal Analysis

A transient thermal analysis determines temperatures and other significant thermal quantities that vary over time. Engineers commonly use temperatures that a transient thermal analysis calculates, as input to structural analyses for thermal stress evaluations.

A transient thermal analysis basically follows the same procedures as a steady-state one. The main difference is that the applied loads are functions of time.

In ANSYS Workbench to specify time-dependent loads, we have to enter the number of steps in the “Analysis Settings” menu and we have to write the duration of each step in the respective “Tabular Data”. Afterwards we need to attribute the correct load values to each step.

Novelty of the Approach

As defined in [5], the calorimetric method, which is analyzed in this work, is a quasi-adiabatic system. By thermodynamic definition, an object is in adiabatic equilibrium if there is no net heat exchange with its environment. In principle a situation whereby there is no net heat exchange can be achieved if the temperatures of the object and its surroundings are in equilibrium all the time. In our case the absorber is at first heated more than the surrounding envelope, so that we can talk about a quasi-adiabatic system, where the heat losses are reduced as much as possible thanks to the insulation layers.

The standard approach towards radiation dosimetry through calorimetry is to measure the superficial dose with a very thin absorber, as previously explained. This goal can be achieved, because the normalized deposed dose shape is represented by a known fit curve, driven by experimental data. This experimental curve is the starting point for standard calorimetry, through which the radiation characteristics can be reconstructed. Indeed, when the superficial dose has been achieved, i.e. the value that can be set as initial value of the normalized absorbed dose, the most relevant characteristics of interaction between matter and radiation driven by the fit curve are known. Instead of using the traditional method of the fitting curve, we use EBXLINK 1D/3D Monte Carlo simulator, which means that we impose the general characteristics of the radiation system, such as the geometry and material properties, so that we get the right information concerning the absorbed dose by matter.

Our approach is different from the usual one, as our key aim is to measure the net average electron beam energy originated from the accelerator source. Therefore we do not need a thin calorimeter; on the contrary our method may be called “Integral dose calorimeter”. This name renders the new idea of our calorimetric system. In fact we need to have information about the integral absorbed dose curve, which means that we require the area defined by the absorbed dose curve, i.e. the average dose, so that we can obtain the average electron beam energy, using equation (7). Eventually our calorimeter is totally absorbing, meaning that its thickness is greater than $1/3$ of the electron range.

The most evident difference between the standard method and ours consist of the thickness of the calorimetric body, but also on the new scope, which we deal with. In fact the thicknesses

of our absorbers, anticipating what is described in the next chapter, are evaluated considering a reasonable thickness value, for which the absorbed dose falls to zero (electron range estimate) – data obtained by simulation of the absorbed dose material that may constitute the calorimetric body.

In these circumstances we want to establish the energy characteristic of the electron beam through the temperature rise within the absorber body and the general accelerator behavior related to the radiation, as we want to provide the accelerator main features.

Chapter 2 – Specifications for a new calorimeter

Calorimeter Geometry

At the beginning of the entire problem analysis one of the first questions that has to be answered consists of the shape of the calorimetric body.

For the choice of the absorber shape, we base our considerations regarding some articles available in the radiation dosimetry field, such as [3], [6], [7], [8], [9], achieving that the most used model is defined by a circular shape, so that the absorber is a solid cylinder.

Our problem may be considered one dimensional, in the thickness direction (z axis), because the most important part of the whole system is the absorbed dose in the third dimension. If we assume that the calorimeter is wide enough to consider small boundary effects, the two longitudinal dimensions have only little relevance in the whole subject matter, because of the integral approach. For this reason we can select the geometry of the absorber without any constraints concerning the solution itself, but we can choose its shape taking into account other features for the modeling, such as practical realization and compatibility with the entire system that has to be built – for instance wires, connections, and temperature sensors.

As one dimension problem, we decide to test the simplest geometrical shapes that can be constructed: we simulate both the cylinder and the parallelepiped as absorber bodies. There is no apparent difference between the two shapes, but, as one of the absolute reference calorimeter is the water one – the water is put in a vessel, usually a Petri dish, whose shape is round – we settle on modeling a cylinder absorber. Another reason for this choice can be found in the fact that the circular symmetry is more suitable to a more uniform heat distribution in reaching the steady-state.

Monte Carlo Simulations for longitudinal dimensions

One issue in the definition of the calorimetric system consists of the longitudinal dimensions of the absorber body. To discuss this matter we decide to compare two square models with $1\ cm$ and $10\ cm$ side, $0.92\ cm$ thick, at $1\ MeV$ and at $4\ MeV$ electron beam energy and see how the system reacts in order to quantify the boundary effects. We evaluate it through Monte Carlo simulations, comparing the absorbed dose value in the middle and at the sides of the model, in both cases the calorimeter is centered in 0 coordinate of x axis – Monte Carlo methods are a class of computational algorithms that rely on repeated random sampling to compute their results.

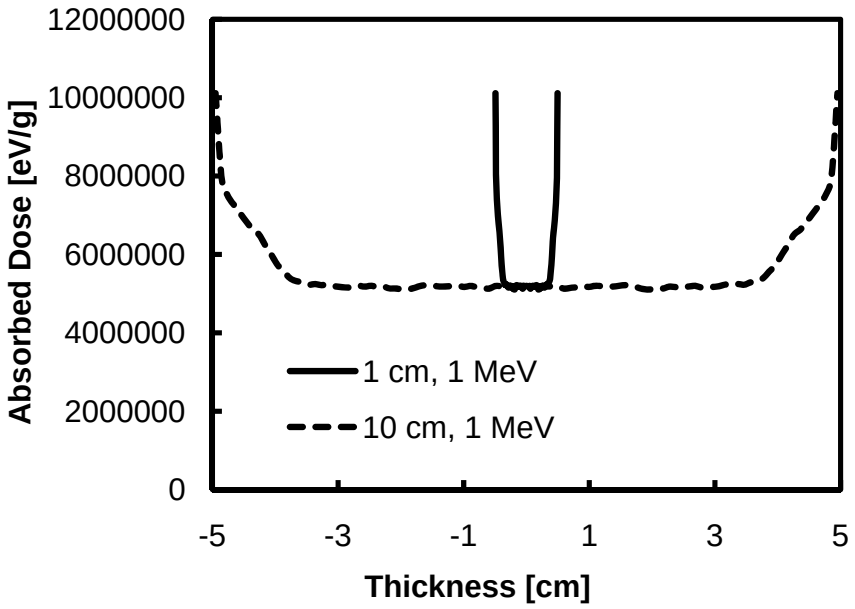

Figure 2 – Absorbed dose versus thickness at 1 MeV electron beam energy for an aluminum square model with 1 cm and for 10 cm side.

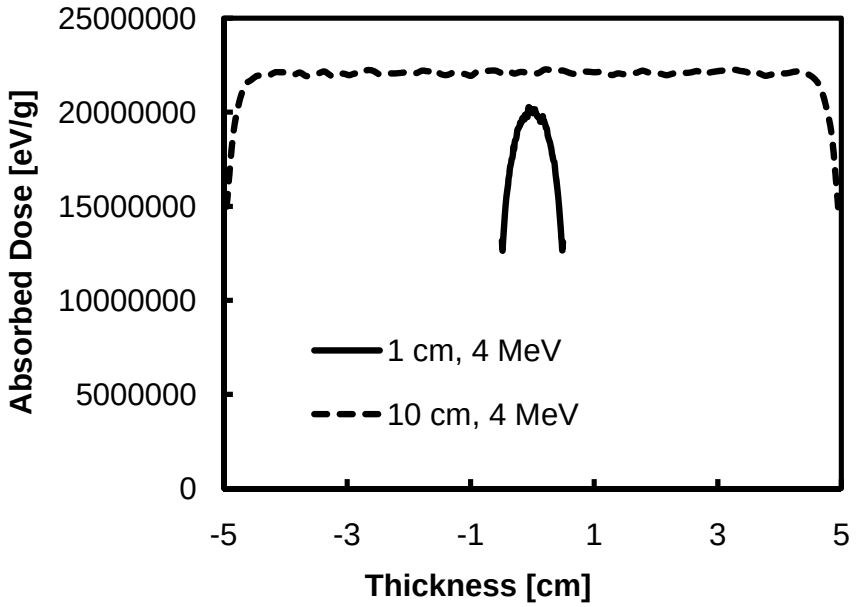

Figure 3 – Absorbed dose versus thickness at 4 MeV electron beam energy for an aluminum square model with 1 cm and for 10 cm side.

As we can see in Figure 2 and in Figure 3 the two models (1 cm and 10 cm side) have an opposite behavior at the two considered energies: at 1 MeV the absorbed dose on the lateral sides is higher than in the middle of the system, whereas at 4 MeV the opposite behavior is shown. In addition we can say that from the two figures above the boundary escapes are more evident for 1 cm model than for the 10 cm one. This fact happens because when the target is small the most evident contribution of electrons is due to the lateral dose, as the electrons impinge the target almost with an oblique trajectory, whereas in the bigger model the majority of the electrons fall almost straight on the absorber and only some of them are scattered outside the calorimeter.

Analyzing the dose data obtained by the simulations, we observe that the boundary escape phenomenon is rather complex because it concerns both the body dimensions and the electron beam energy. Thus, as we need to test our calorimeter in the $0.5 - 2\ MeV$ energy range, we have to choose proper dimensions to guarantee the energy losses due to boundary effects lower than 3%, a loss value that should be negligible if compared to the total energy amount.

Thereby we opt for a cylinder model with 9 cm diameter, to render the boundary escapes as small as possible.

Absorber Materials

Even though any material could be selected as calorimetric absorber, we find out that the most used materials are: water, polystyrene and graphite – as we can see in several references: [3], [4], [6], [7], [8], [9], [10], [11].

In [3] are described the calorimeters used for industrial electron accelerators: they are constructed in graphite, polystyrene or with a Petri dish filled with water as calorimetric body. In addition polymeric materials other than polystyrene may be used for calorimetric measurements, but polystyrene is usually chosen because it is known to be resistant to radiation and because no exo- or endothermic reactions take place.

The typical water, graphite, and polystyrene calorimeter equipments, illustrated in [3], have similar features. Both the graphite and the polystyrene calorimeters are composed of a disc placed in a thermally-insulating material such as foamed plastic. A calibrated thermistor or thermocouple is embedded inside the disc. A water calorimeter is a sealed polystyrene Petri dish filled with water and placed in thermally-insulating foamed plastic. A calibrated temperature sensor (thermistor) is placed through the side of the dish into the water.

At first we leave the water calorimeter aside – since the water absorber is the reference model because it has the most well-known and stable C_p – and we decide to test through Ansys WB simulator five different materials that could constitute the final calorimeter absorber. The chosen elements are: graphite, aluminum, copper, polyethylene, and polystyrene. Among all the different materials that could have been selected we decide to investigate the just mentioned materials for the following reasons:

- Graphite (Union Carbide AGOT) [4] is used because its irradiation does not lead to chemical reactions that consume or release significant energy and its atomic number is comparable to water. Furthermore its thermal diffusivity leads to an even distribution of heat in the calorimeter absorber, and the graphite is easy to machine;

- Aluminum is suggested by [12], as their results agree quite well with simulations;
- Copper is tested because is another metal, like aluminum, that can be easily found and bought (in this case we want to stress the practical matter of constructing the final object);
- Polyethylene (PE) is taken into account since it is another polymeric material which is easily available, above all in the industrial field (for instance cable insulation);
- Polystyrene (PS) is tested because there is plenty available quantities of it and for its properties described by [3].

Analytical ΔT expression

Before approaching the simulative part, it is necessary to have an analytical confirmation of the temperature difference. The analytical expression we deal with is derived and rearranged through (7), where we have to insert the accelerator and calorimeter parameters; the formula is given by (8):

$$\Delta T = \frac{V \cdot I \cdot \Delta t}{A_{irr} \cdot C_p \cdot t_{cal} \cdot \rho} \qquad (8)$$

where ΔT is the difference of temperature $[K]$, V is the beam voltage [V], I is the beam current [A], A_{irr} is the irradiated area defined by the scanner $[cm^2]$, t_{cal} is the calorimeter thickness $[cm]$, and ρ is the material density $\frac{g}{cm^3}$.

In the next chart of Figure 4 (8) formula trend is depicted, which stands for the mathematical mean to estimate the difference of temperature values.

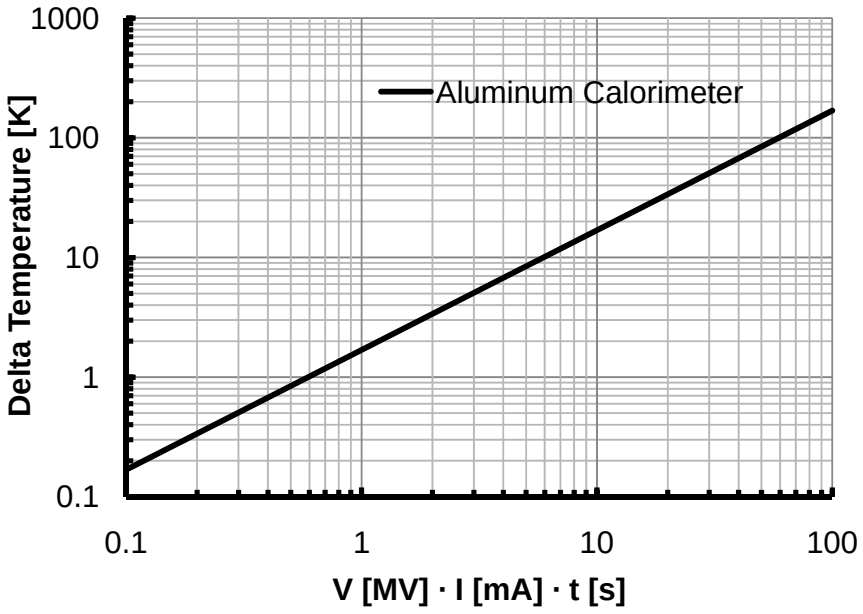

Figure 4 – Analytical representation of the reference equation (8) in logarithmic scale.

As shown in Figure 4 the dependent variable is indeed the difference of temperature, whereas the independent variable is represented by the product of three parameters that can be set in the accelerator system: the electron beam voltage, the beam current, and the time due to the conveyor movement under the accelerator. This graph may be useful if the uncertainties of the different parameters are not well-known, so that we can establish in a more accurate way only the final product of the three quantities. The slope of the straight line is defined by the calorimeter characteristics: irradiated area, specific heat capacity, thickness and density, as clearly expressed by equation (8). We set logarithmic axes, because in this way we may appreciate better the range we deal with. Our working point is namely $V = 1\,MV,\ I = 10\,mA,\ t = 0.82\,s$. Thus our x coordinate in Figure 4 is $8.2\,MV \cdot mA \cdot s,$ to which corresponds a delta temperature $\Delta T = 13.84\,K$.

Thermal Simulations through Ansys WB

At the beginning of the thermal behavior investigation of the above mentioned materials we focus on a quite large energy range: from $1\,MeV$ to $4\,MeV$. This energy range does not

concern really high energies, because this range usually involves energies beyond 5 MeV, but at the same time is not extremely low, because some research go below 1 MeV, as in [12] where it is described $80 - 120$ keV range.

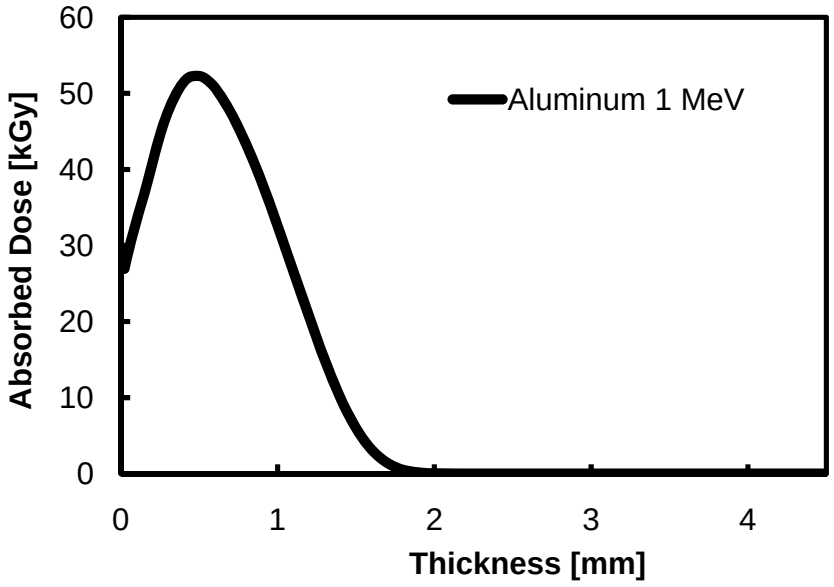

Figure 5 – Absorbed dose curve in an aluminum absorber 0.45 cm thick at 1 MeV electron beam energy.

The next step is to establish the calorimeter thickness in order to consider the absorbed radiation for the whole energy range. To make this argument we consider the typical absorbed dose curve, represented in Figure 5 for an aluminum absorber at 1 MeV electron beam energy: as our system has to absorb the integral dose, we need a thickness value for which the absorbed dose falls to zero. For the thickness estimate we decide to use the CSDA (Continuous Slow Down Approximation) range for the analyzed materials at different energies; even though the CSDA range is an overestimation of the electron range. [1]

The calorimeter is collocated on a conveyor moving under the electron beam at a constant speed of 5.5 $\frac{cm}{s}$, meaning that the electron irradiation is progressive: before irradiation the whole calorimeter is at the same room temperature, then each part of our device is gradually

[1] The CSDA graphs are evaluated through ESTAR software developed by NIST (National Institute of Standards and Technology – Physics Laboratories) and are presented in Appendix – A.1.

irradiated (reaching a temperature peak), and at last the calorimeter temperature is equalized (steady-state). As this process is quite complicated to model, we need to simplify it: we consider a cylinder calorimeter, whose plot is represented in Figure 6, that is simultaneously irradiated from the top layer with a uniform electron dose deposition.

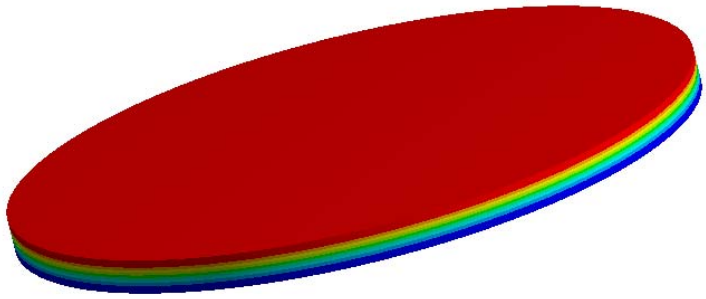

Figure 6 – Ansys thermal model: representation of the cylinder calorimeter heating.

When we have to reproduce the electron beam behavior in Ansys WB, there is no application that may represent the electron transit from the accelerator towards the calorimeter – the software is used in mechanical branches, where engineers have to simulate physical loads in a way that involves machines or mechanical engines – so that we have to convert the electron energy into a heating source. For this reason in Ansys thermal analysis palette we have to define the "Internal Heat Generation", but, as the measure unit of this function is $\left[\frac{W}{cm^3}\right]$, we have to convert the beam energy to a power per unit volume. Therefore we decide to link the energy range, the absorber calorimeter thickness, and the heat generation in the following way: we determine that the calorimeter must have a global thickness of CSDA range at 4 MeV, so that we cover the worst case radiation penetration (upper threshold energy), but, to characterize the internal heat source, we select a thinner source volume on the absorber, whose thickness is the CSDA range at 1 MeV (lower threshold energy). Hence we have the heating source that is represented by the first few millimeters of the calorimeter.

In the conversion from the accelerator energy to the power heating we use the following expression (9) (rearranging (8)):

$$P = \frac{V \cdot I}{A_{irr} \cdot t_s} \quad \left[\frac{W}{cm^3}\right]$$

where P is the internal heat source $[W]$, V is the beam voltage $[V]$, I is the beam current $[A]$, A_{irr} is the irradiated area defined by the scanner $[cm^2]$, and t_s is the source calorimeter thickness $[cm]$.

For each simulation the starting temperature is set at $22\ °C$, and, as a consequence of what has just been explained, for our high energy range analyses, the parameters are set in the following way:

- $V = 1\ MV$;
- $I = 10\ mA$;
- $A_{irr} = 540\ cm^2$;
- t_s $[cm]$ is defined for each material by the CSDA range at $1\ MeV$.

In Figure 7 the internal heat generation, as we need a transient thermal analysis, is shown. It is the aluminum simulation, and the maximum constant power value is $88.2\ \frac{W}{cm^3}$. The duration of the power pulse is $0.82\ s$ (the power pulse starts at $1s$) as we have to reproduce the conveyor movement under the electron beam (before, during, and after radiation phases). The internal heat radiation for each material is set with the same radiation pulse, where the power value is related to the considered element through (9).

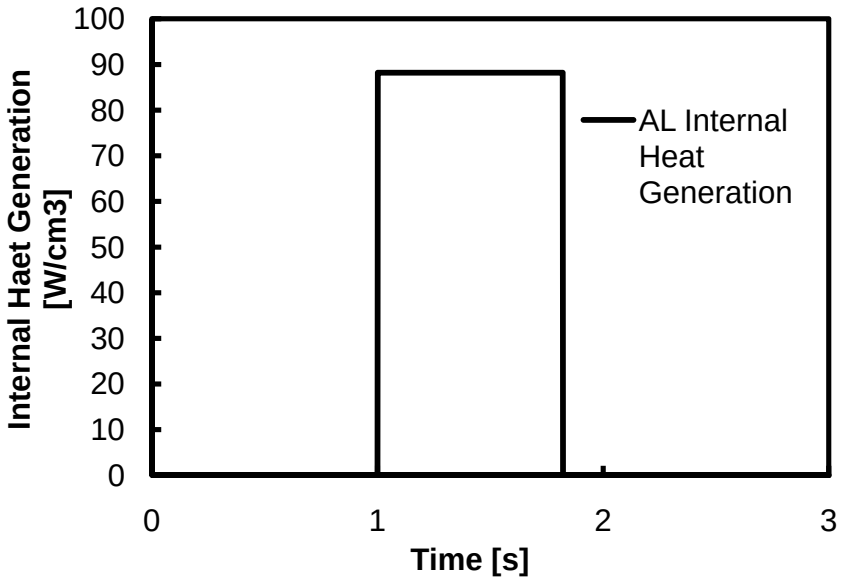

Figure 7 – Representation of the Internal Heat Generation. It is a power pulse per unit of volume, which duration lasts 0.82s.

This first general analysis is needed to find out the timing properties of the different materials, so that we can make the best choice not to wait a too long time to reach the steady-state.

In order to know only the absorber thermal performance, we simulate the calorimetric body alone, without any envelope, and with perfectly insulated sides, so that every boundary condition builds an ideal system.

When defining different materials in Ansys, we have to set their properties such as density, thermal conductivity, and specific heat capacity. Although thermal characteristics such as the specific heat capacity and the thermal conductivity may vary over temperature, constant values are assumed to render a simple model and for the temperature range we deal with, we can assume constant values.

In Table 1 we summarize the material properties we use to simulate our systems.

Table 1 Material Parameters.

Material	CSDA 1MeV	CSDA 4MeV	Specific Heat Capacity C_p	Density ρ	Internal Heat Generation	Thermal Conductivity k
	cm	cm	$\frac{J}{kg \cdot K}$	$\frac{g}{cm^3}$	$\frac{W}{cm^3}$	$\frac{W}{m \cdot K}$
Graphite	0.29	1.37	724.28	1.7	63.86	150
Aluminum	0.21	0.92	900	2.7	88.2	237
Copper	0.07	0.31	380	8.96	264.5	401
PE	0.44	2.09	2300	0.94	42.1	0.28
PS	0.42	1.98	1340	1.06	44.1	0.15

Through the data gathered in Table 1, we present the simulations run by Ansys. The two curves shown in each of the following graphs (Figure 8, Figure 9, Figure 10, Figure 11, Figure 12) depict the average trend of the maximum and minimum temperature in the solid body, while the heat is distributed over the entire calorimeter in reaching an uniform equilibrium temperature.

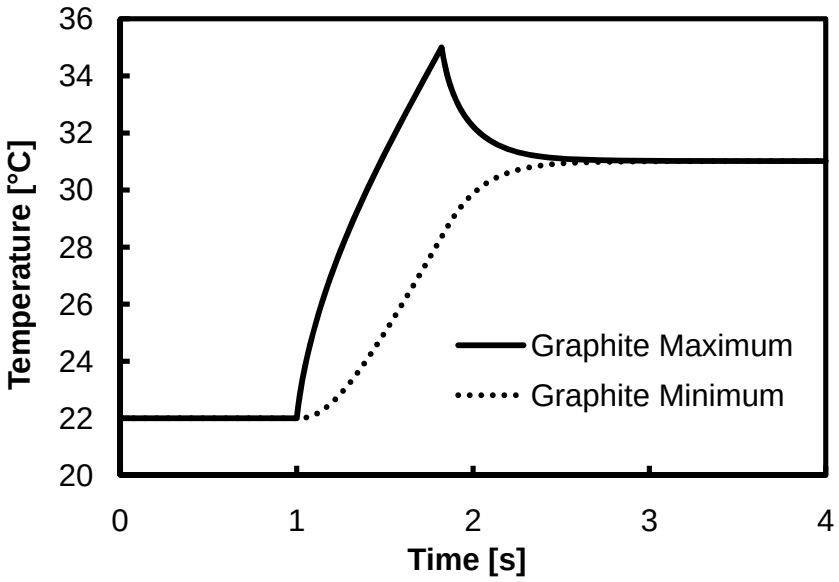

Figure 8 – Graphite Maximum and Minimum Temperature trends in the calorimeter.

The first analyzed material is graphite. From the simulation shown in Figure 8, we notice that the timing properties are compatible with our goal, but there are still two problems: the first consists of the unknown exact graphite specific heat capacity value, and the second consists of the difficult availability of Graphite Union Carbide: this leads to the conclusion that graphite is not suitable for our system.

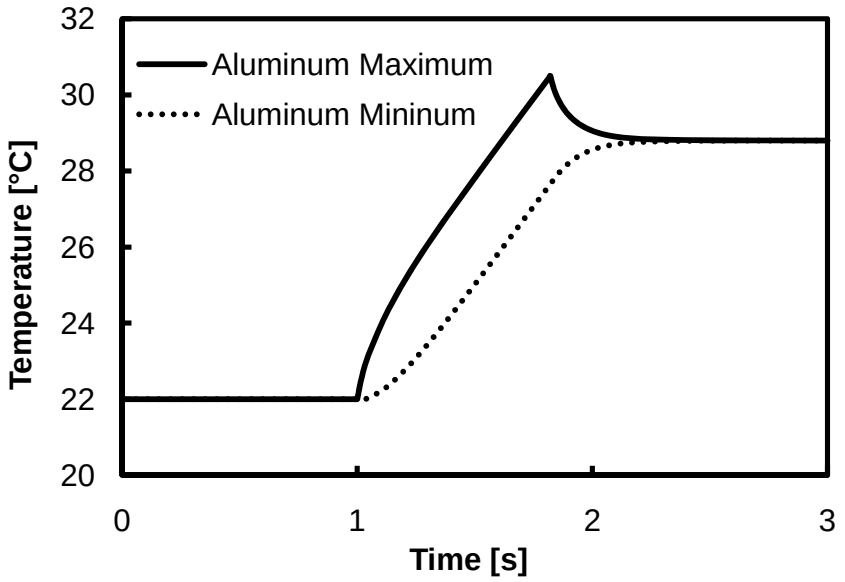

Figure 9 – Aluminum Maximum and Minimum Temperature trends in the calorimeter.

In Figure 9 the aluminum temperature trends are represented. We observe that this material reaches the steady state quickly, so that it may be our candidate for the calorimetric system. Aluminum has a reaction behavior very close to graphite, but it easier to find and buy.

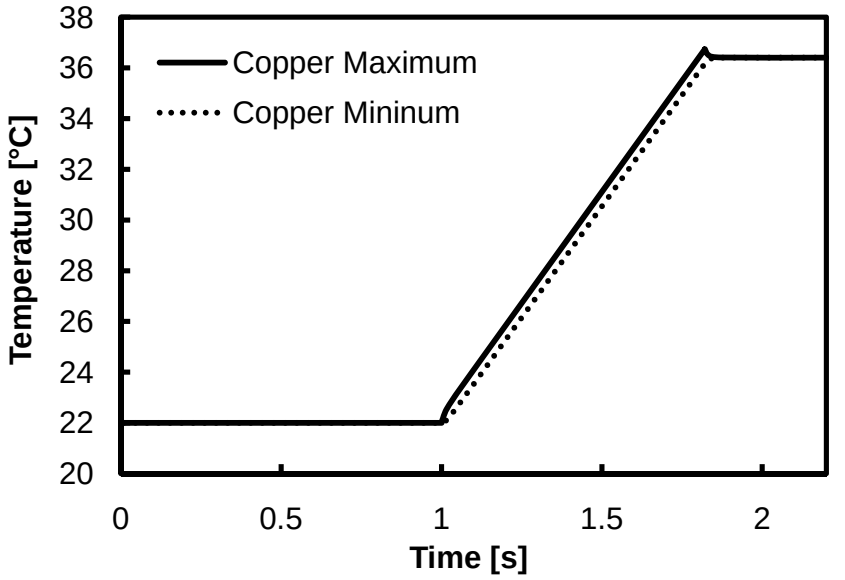

Figure 10 – Copper Maximum and Minimum Temperature trends in the calorimeter.

In Figure 10 the copper simulation is plotted. Also this metal has a very rapid time reaction; the only fact that prevents us going further with this model is that copper is a material with quite a high atomic number (heavy element), so that there could be some problems concerning x-ray emissions.

In Figure 11 and Figure 12 the polyethylene (PE) and polystyrene (PS) simulations are shown. We can notice that in both cases the simulations have to run for a very long time ($3500\ s$) and that there is an anomalous non physical behavior just after the power pulse, probably due to the numerical analysis and maybe to the high thermal resistivity value.

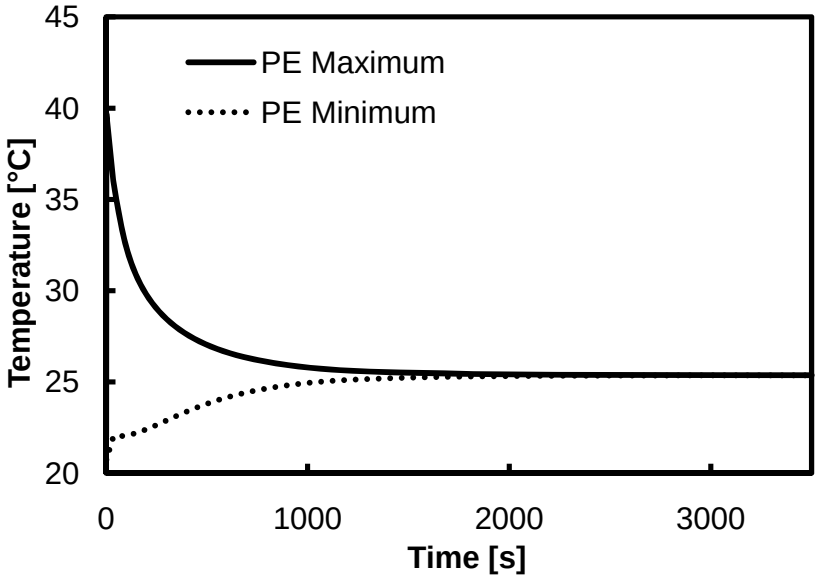

Figure 11 – Polyethylene (PE) Maximum and Minimum Temperature trends in the calorimeter.

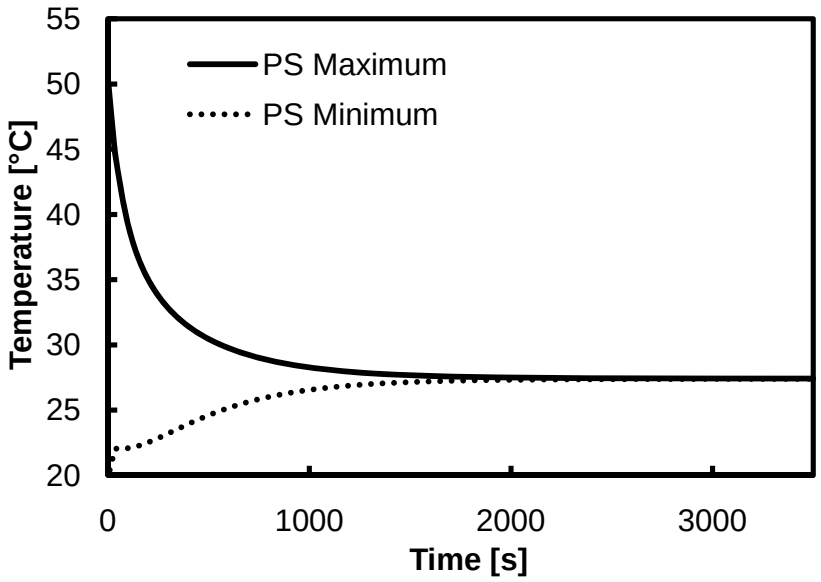

Figure 12 – Polystyrene (PS) Maximum and Minimum Temperature trends in the calorimeter.

Thanks to the previous analyses we discover that these polymers are not consistent for our purpose, because of the extremely long time constants. In fact if the materials had a too long time constant, they would cool down before reaching the steady-state, completely altering the temperature measurement.

In Table 2 all the data from the former graphs are collected.

Table 2 Temperature and Timing parameters.

Material	Analytical ΔT K	Simulated ΔT K	Final Simulated Temperature $°C$	Peak Temperature $°C$	Simulated Time Constant s	Simulation Duration s
Graphite	9.002	9.014	31.014	34.998	0.517	4
Aluminum	6.792	6.802	28.802	30.5	0.295	3
Copper	14.387	14.404	36.404	36.741	0.035	2.2
PE	3.361	3.368	25.368	39.696	795.34	3500
PS	5.4	5.412	27.412	50.301	875.63	3500

In the end we decide for an aluminum calorimeter, which should be a good compromise among all the properties previously listed.

Final Simulation: Aluminum Calorimeter

A specification limit of the accelerator we use for the experimental test is the 2 MeV upper threshold energy. Thus we fit the general analysis for the selected material and the selected energy range to the final model: we settle that the solid calorimetric body is an aluminum cylinder of 9 cm diameter, with a thickness of 0.45 cm (CSDA electron range in aluminum at 2 MeV electron beam energy), so that it may afford an energy radiation up to 2 MeV, even though our reference energy is 1 MeV or below it.

In Figure 13 the simulations of the final aluminum model through Ansys WB are depicted, where we observe that the temperature peak is $T_{max} = 36.385℃$ and a global temperature difference of $\Delta T = 13.906\ K$.

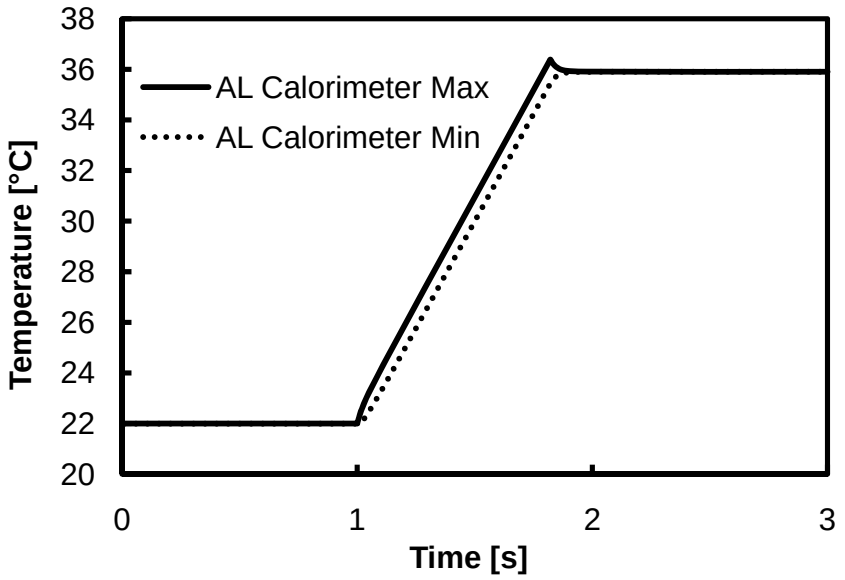

Figure 13 – Aluminum Maximum and Minimum Temperature trends in the final model calorimeter.

As we need to proceed as accurately as possible, we measure the final aluminum disc (real object), obtaining the following dimensions:

- Thickness $0.45\ cm$;
- Diameter $9\ cm$;
- Weight $77.5\ g$.

With these physical dimensions and knowing that the disc has an internal cylindrical hole (thermal sensor container), whose diameter is $0.16\ cm$ and length is $3\ cm$, we obtain the density of the material we deal with: $\rho = 2.71\ \frac{g}{cm^3}$.

Material Time Constants

Through Ansys analyses we find out the simulated material time constants. After the power pulse, the temperature decrease does not follow a real exponential curve, so that we cannot extrapolate the time constant in the usual way. For this reason we consider the difference

between 95% and 5% value of the maximum and equilibrium temperatures. Figure 14 represents the simulated points, and a power trendline, through which we can give a rough idea of the time constants for other different materials that may be tested, knowing thermal properties, i.e. thermal conductivity and specific heat capacity.

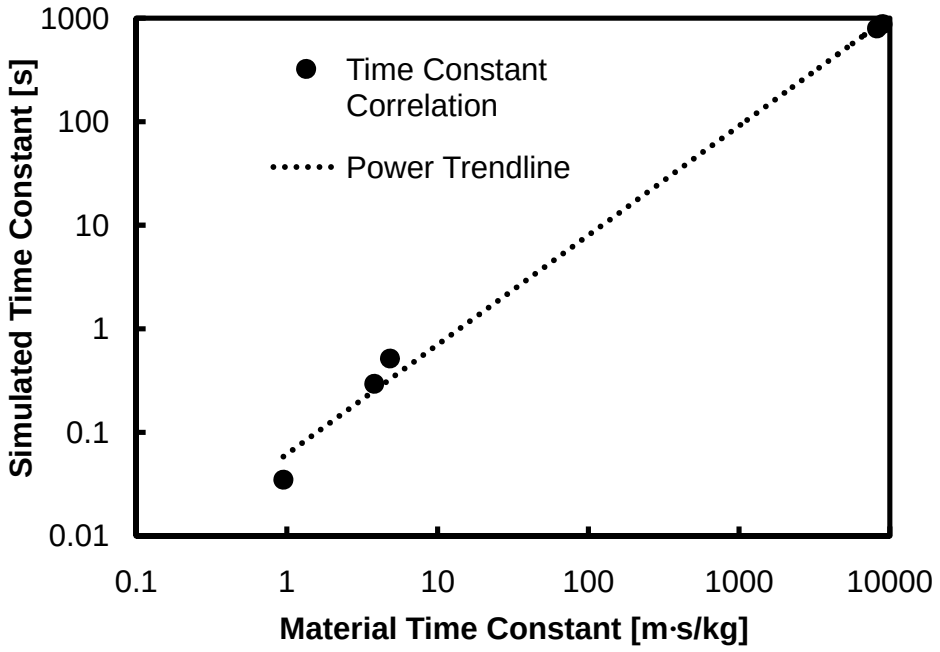

Figure 14 – Physical material time constants versus simulated time constant. The solid markers represent the material physical characteristic, while the dot line describes a power law trend extrapolated through the simulated data.

The experimental power law (power trendline) of Figure 14 is represented in (10):

$$\mathrm{T} = 0.017 \cdot \left(\frac{C_p}{k}\right)^{1.0562} \qquad (10)$$

where T is the experimental time constant $\left[\frac{m \cdot s}{kg}\right]$, C_p is the specific heat capacity $\left[\frac{J}{kg \cdot K}\right]$, and k is the thermal conductivity $\left[\frac{W}{m \cdot K}\right]$.

The calculated points of Figure 14 are shown in Table 3.

Table 3 Esteemed Timing data.

Material	Simul. Time Constant s	$\frac{C_p}{k}$ $\frac{m \cdot s}{kg}$
Graphite	0.517	4.829
Aluminum	0.295	3.797
Copper	0.035	0.948
PE	795.34	8214.3
PS	875.63	8933.3

Through Figure 14 we can remark that the experimental power law is only an estimate of the real time constant, while comparing the markers and the trendline. We also calculate how big the error could be, if we relate the power law and the simulated data. Therefore we establish that the biggest difference is met within copper, with almost 40% error. As previously written this is not a precise evaluation, since the aim of the trendline is to render a rough estimate of the material time constant.

Equivalent Compact Thermal Model

As Ansys is a complex simulation tool and our thermal problem is a one-dimensional one, we examine the thermal analysis as an electrical problem. We determine an electrical compact equivalent model, shown in Figure 15, where the thermal parameters are converted to electrical equivalents. This conversion is possible because every thermal parameter has an electrical equivalent: power becomes current, thermal capacity becomes electrical capacitance, and thermal resistance becomes electrical resistance. The program used for the simulations is Spice, whose simple circuit describes the charge distribution of the two capacitors (they represent the 1 MeV and 4 MeV CSDA thicknesses of Ansys model).

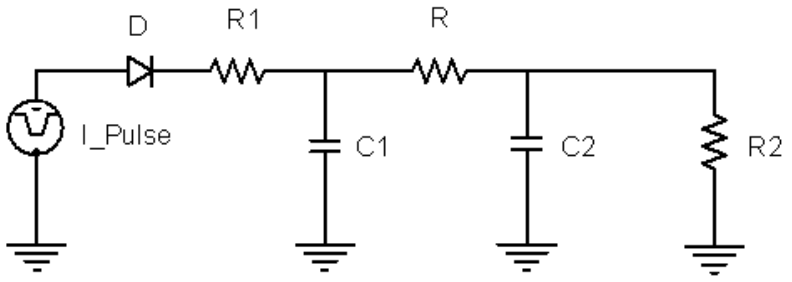

Figure 15 – Equivalent compact thermal model.

The devices used in the spice model are: a current pulse generator, which represents the power pulse in Ansys, an ideal diode to prevent the current reflux back to the source, $R_1 = 10\,\mu\Omega$ and $R_2 = 10\,E\Omega$ resistances are used for convergence needs (numerical problems), and the other resistance and capacitors, whose dimensioning derives from the thermal and physical properties of the calorimeters, are listed in Table 4.

To simplify the analysis we concentrate on a $1\,cm^2$ calorimetric body, so that the power pulse is equal for each material, as the expression (11) shows:

$$P_a = \frac{V \cdot I \cdot \Delta t}{A_{irr}} \quad \left[\frac{W}{cm^2}\right] \qquad (11)$$

where $V = 1\,MV$ is the beam voltage, $I = 10\,mA$ is the beam current, $\Delta t = 0.82\,s$ is the time scanning, and $A_{irr} = 540\,cm^2$ is the irradiated area. Inserting the mentioned values in the previous formula we obtain $P_a = 18.5\,\left[\frac{W}{cm^2}\right]$.

As previously explained we divide the calorimeter in two parts: the source, which represents the CDSA range at $1\,MeV$, and the base, whose thickness consists of the difference between CDSA range at $4\,MeV$ and $1\,MeV$. This procedure is evaluated for each material apart from aluminum, whose higher energy is $2\,MeV$ instead of $4\,MeV$, as we decided that aluminum is our future calorimeter. In this way we model the two capacitors of the electric model with reference to the two volumes of different thicknesses. The material parameters such as thicknesses, thermal conductivity, and density have been listed in Table 1.

Table 4 Electrical circuit parameters.

Material	C_1	C_2	R
	$\frac{J}{K}$	$\frac{J}{K}$	Ω
Graphite	0.3569	1.3293	0.4567
Aluminum	0.5103	0.5832	0.0949
Copper	0.2383	0.8172	0.0387
PE	0.9513	3.5673	373.21
PS	0.5966	2.2158	660

Equivalent Electrical model: Spice simulations

When simulating the compact model, we can observe that the thermal analysis and the electrical one correspond with an accuracy of $\pm 2\%$ through the following graphs, thus showing the equivalence of the two methods. The little differences in the temperature values are shown in Table 5. To simplify the analysis we define the initial temperature at $0℃$ for each electrical model so that the delta temperature coincides with the steady-state temperature. We arrange Ansys data removing the initial temperature constant ($22℃$,) from the already acquired data and the initial time analysis starting with the power pulse at $0\ seconds$.

In Figure 16 we report the maximum and the minimum temperature trends of the electrical circuit representing the aluminum calorimeter. We can notice that the temperature behaviors are similar to the ones depicted in Figure 13 (Ansys model). The only little differences we can appreciate are gathered in Table 5 and consist of the maximum peak temperature and of the steady-state temperature.

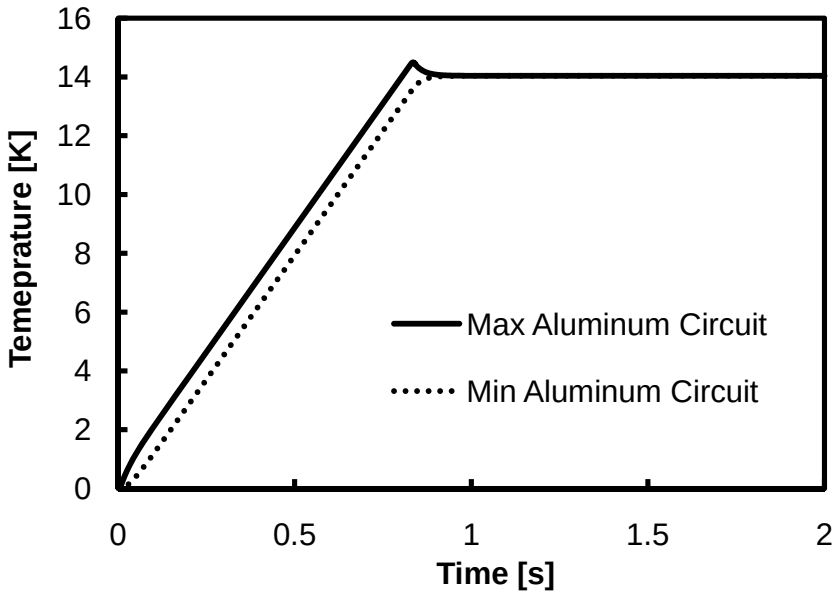

Figure 16 – Aluminum Maximum and Minimum temperature trends of the electrical circuit.

In Figure 17 we can notice the graphite comparison between the thermal Ansys model and the compact model. In this case the round marker (Ansys) and the straight line (compact model) do not match during the first part of the simulation that coincides with the heat pulse. However the final steady-state temperature is practically the same, as reported in Table 5.

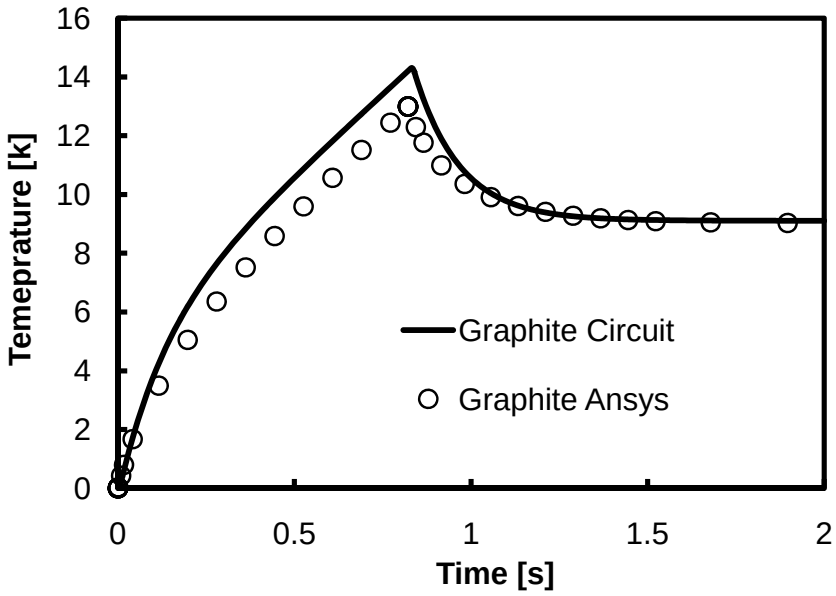

Figure 17 – Graphite comparison between thermal Ansys model and electrical circuit model.

In Figure 18 and Figure 19 are respectively depicted the aluminum and the copper comparisons (only maximum temperature trends) between thermal Ansys model and electrical circuit model. From these simulations we see that the round markers (Ansys) and the straight line (compact model) match almost completely, giving proof of the equivalence between thermal and electrical models.

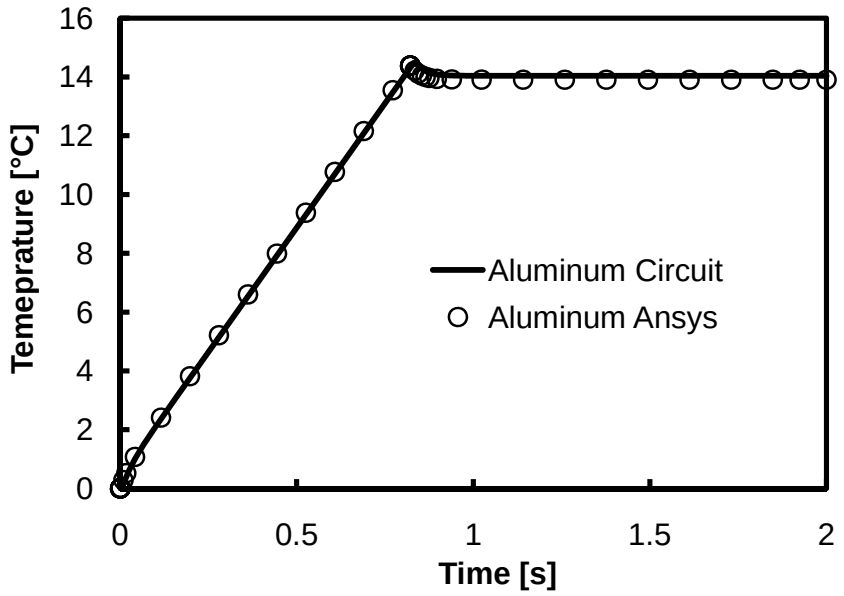

Figure 18 – Aluminum comparison between thermal Ansys model and electrical circuit model.

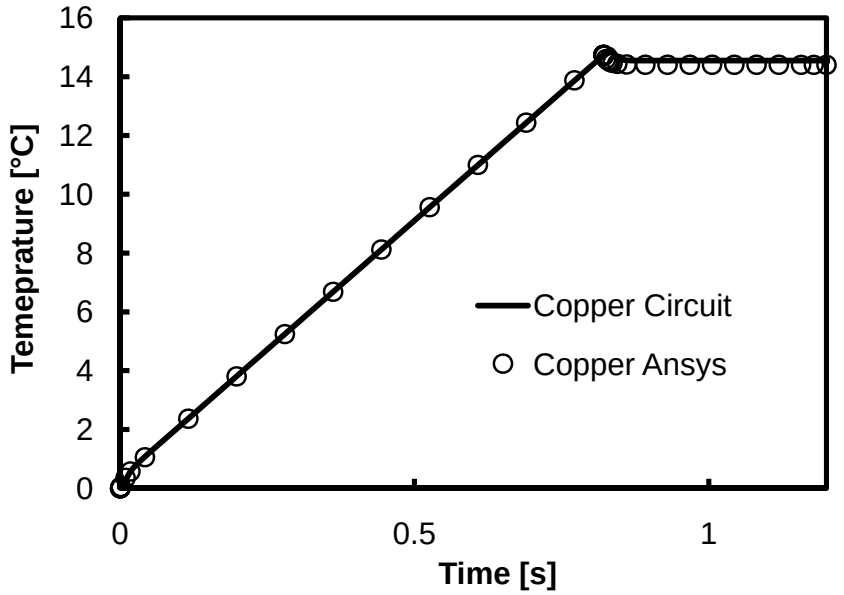

Figure 19 – Copper comparison between thermal Ansys model and electrical circuit model.

In Figure 20 and in Figure 21 the maximum temperature trends of respectively PE and PS are plotted. In these cases we can observe that there are some differences between compact and thermal models: Ansys model gives a higher temperature peak, and just after the power (current) pulse the two trends do not match completely, but the steady-state temperature reached is practically the same value, as seen in the graphs and summarized in the Table 5.

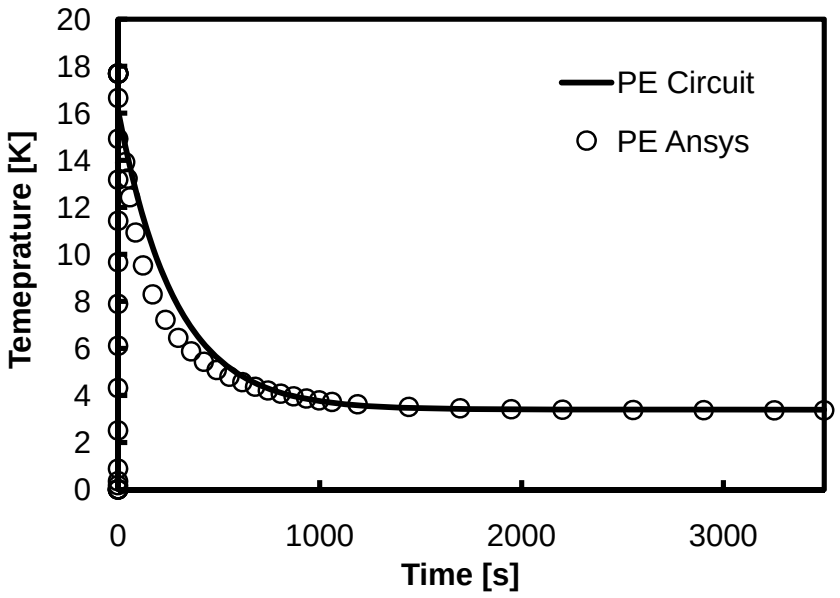

Figure 20 – Polyethylene (PE) comparison between thermal Ansys model and electrical circuit model.

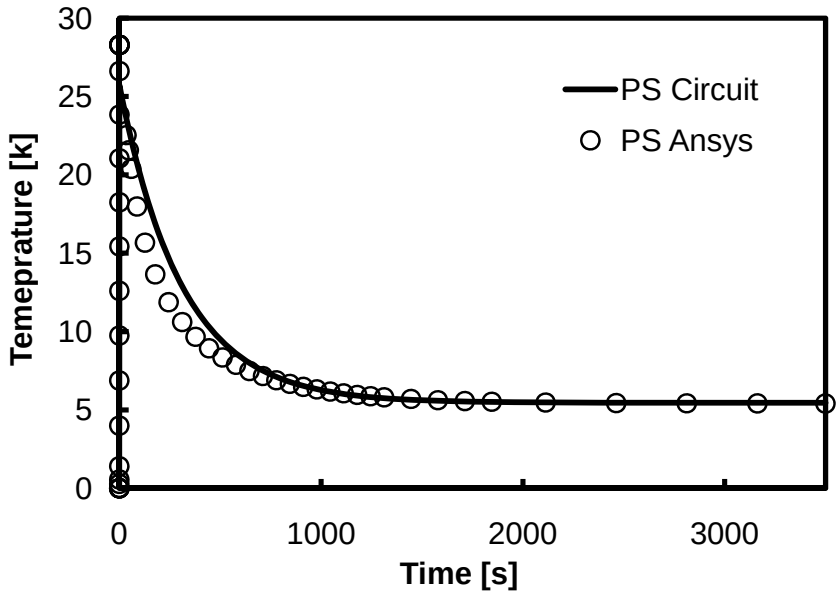

Figure 21 – Polystyrene (PS) comparison between thermal Ansys model and electrical circuit model.

Table 5 Comparison between thermal and electrical model.

Material	Thermal ΔT	Electric ΔT	Peak Thermal Temperature	Peak Electric Temperature
	K	K	$°C$	$°C$
Graphite	9.014	9.11	12.998	14.305
Aluminum	13.906	14	14.385	14.498
Copper	14.404	14.5	14.741	14.911
PE	3.368	3.398	17.696	16.12
PS	5.412	5.459	28.301	25.708

From all the graphs containing the electrical and the thermal simulation we find out that they completely match only for the metal cases (aluminum and copper), whereas for the other materials there are some differences, probably due to the particular thermal conductivity and specific heat capacity values.

Chapter 3 – Hardware Design through Monte Carlo Simulations

Design Assisted by Dose Simulations: Monte Carlo simulator

After considering the most significant part of the calorimetric system, i.e. the absorber body, we have to consider the insulator envelope.

A lot of references [3], [4], [6], [8] suggest a complete wrapping up of the calorimetric body in an insulator box, when analyzing a quite high energy range; whereas the [12] reference, that deals with a $80 - 120\ keV$ energy range, work without complete thermal insulation because of the short range of electrons. As our energy case is in-between we decide to examine the entire system with insulation on all sides. From these simulations we have to establish the envelope dimension.

At first we concentrate on a wide energy range: $1 - 5\ MeV$, just to appreciate the differences in the absorbed dose behavior.

To render the simulation less complicated, we use the following parameters for the geometrical shapes. The envelope consists of an expanded polystyrene cylindrical box $8\ cm$ thick with $20\ cm$ diameter. The expanded polystyrene foam (abbreviation EPS) is considered with a density $\rho = 0.03\ \frac{g}{cm^3}$ and a specific heat capacity $C_p = 1.34\ \frac{J}{g \cdot K}$. In the inside centre there is an aluminum cylinder calorimeter $0.5\ cm$ thick with $10\ cm$ diameter.

The following figures represent the simulations evaluated by EBXLIKN 3D Monte Carlo simulator. These pictures are in three dimensions (3D), because in the x axis it is plotted one horizontal dimension, in the z axis it is plotted the vertical dimension and the colored scale of the whole sketch describes the absorbed dose state in the $\left[\frac{eV}{g}\right]$ measure unit, which is

converted through the electron charge $q = 1.6e^{-19}\,C$ to the absorbed dose in $[kGy]$: $\left[\frac{eV}{g}\right] \times q = \left[\frac{J}{g}\right] = \left[\frac{kJ}{kg}\right] = [kGy]$.

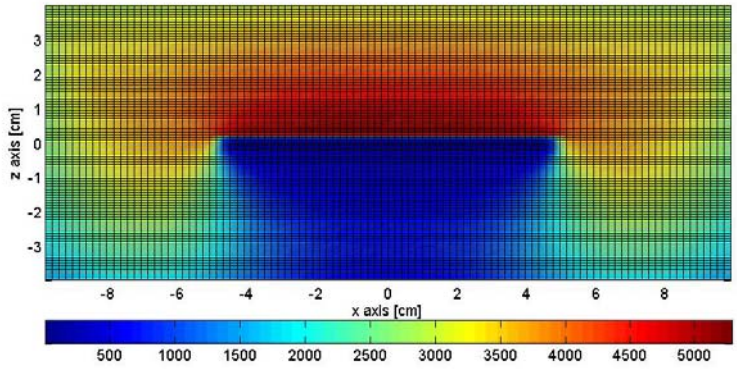

Figure 22 – Absorbed Dose profile at 1 MeV energy simulation.

From Figure 22 it is obvious that the absorbed dose peak is achieved outside the calorimeter body, namely in the upper part of the insulator layer (red color), which means that a very high energy value is absorbed within the top polystyrene layer, leaving the calorimeter essentially not irradiated.

The absorbed dose peak is reached in the expanded polystyrene foam $D_{peak} = 55.65\,kGy$, which corresponds to a difference of temperature $\Delta T = 41.3\,K$; in the aluminum absorber the average absorbed dose is $\overline{D} = 8.09\,kGy$, which corresponds to $\Delta T = 8.99\,K$. The conversion from dose to temperature is carried out through equation (7). From the colored scale of Figure 22 we can also observe the presence of an almost unirradiated area under the calorimeter. This blue zone may be called “radiation shadow”, which means that the radiation is not able to penetrate the entire box system under the calorimeter.

Already from Figure 22 we understand that for our purpose and for our reference energy we cannot have an upper insulation layer, otherwise the absorber is almost not irradiated. However, to give proof for our assumptions, we analyze and plot in Figure 23 the absorbed dose in EPS versus the thickness layer. For this reason we run the simulations from 1 MeV to 5 MeV, with 1 MeV step.

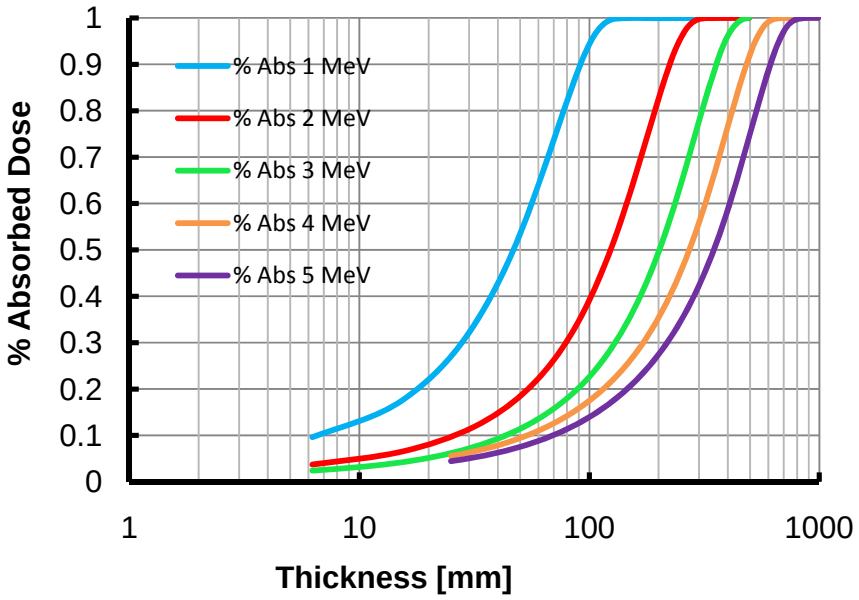

Figure 23 – Representation of the Normalized Absorbed Dose trends in the EPS top layer versus its thickness. As the legend shows, we plot the Absorbed Dose percentage at 1 MeV, 2 MeV, 3 MeV, 4 MeV, and 5 MeV electron beam energy to evaluate the EPS absorption behavior.

If we look at the 1 MeV curve (light blue), we can notice that for the considered thickness, i.e. 4 cm, the absorbed dose percentage is almost 45%. This is the reason why we cannot use a top polymeric layer, like the one we have simulated, because almost half of the incident radiation is already absorbed in the EPS layer instead of heating the calorimeter, so that we may not have good measurements.

If on one side the absorbed dose in EPS top layer is very high at 1 MeV energy, on the other the absorbed dose percentage at 5 MeV (purple curve) is about 6%, that means an acceptable energy loss, as we can see from the curves presented in Figure 23. This is the reason why,

when dealing with high energy ranges, the globally used insulator envelope may be quite thick, as for instance in [6] reference.

As in Figure 232 (1 MeV beam energy) and later in Figure 26 (5 MeV beam energy) the Monte Carlo data are presented from a thermal 3D point of view, we convert these data in a 2D graph in Figure 24, where we plot the absorbed dose versus the analyzed thickness, so that we can compare the absorbed dose profile for the considered threshold energies, i.e. 1 MeV and 5 MeV. We can also observe from the depicted curves in Figure 24 that there is a big dose gradient at 1 MeV beam energy, due to the major radiation absorption in the upper expanded polystyrene layer.

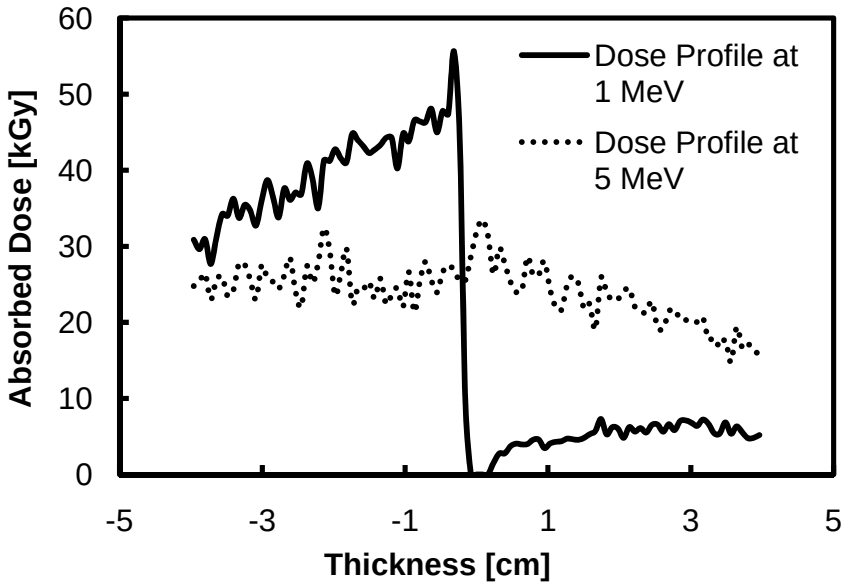

Figure 24 – Absorbed Dose profile at 1 MeV and at 5 MeV beam energy.

As a consequence of the absorbed dose curves in Figure 24, we derive the delta temperature profile in the calorimetric model at 1 MeV and at 5 MeV beam energy, as shown in Figure 25. For the conversion from absorbed dose to temperature we always refer to (7), where we have to specify that the temperature profile in EPS is considered punctual because it is an insulator, whereas the aluminum temperature is constant because the heat distributes in the whole volume.

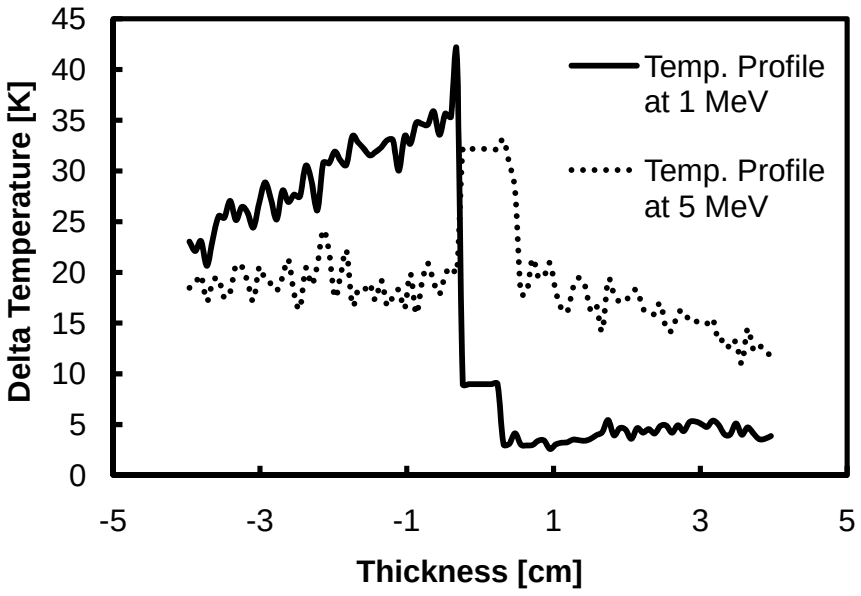

Figure 25 – Delta Temperature profile at 1 MeV and at 5 MeV beam energy.

In Figure 26 the absorbed dose profile for 5 MeV beam energy is presented. Looking at this picture we can immediately notice through the colored scale that the electron beam goes through the aluminum body, where the maximum dose value is reached. In this high energy case the electrons are not stopped within the calorimeter. The reason why it happens is because the aluminum thickness is less than the CSDA range at 5 MeV energy. While in Figure 22 the shadow effect is evident, in Figure 26 this effect is not interesting because of dealing with a high energy case. In this sketch it is worth remarking the presence of lateral scattering, which appears on both the absorber body sides from the calorimeter boarders to the bottom system. This phenomenon is relevant because we have to take into account also the fact that with higher beam energy the electrons deviate with a larger spreading angle from the straight direction, so that they cannot be imprisoned in the aluminum body (lateral impinging electrons).

The absorbed dose peak in Figure 26 is reached within the aluminum body $D_{peak} = 33.5\ kGy$, while the average absorbed dose within the calorimeter is $\overline{D} = 29\ kGy$, which corresponds to a temperature difference of $\Delta T = 32.2K$.

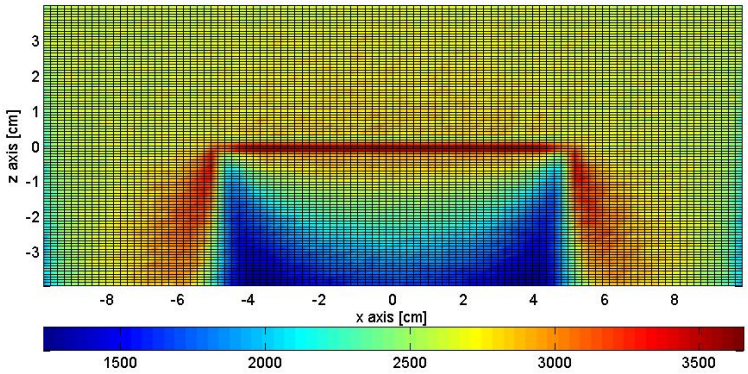

Figure 26 – Absorbed Dose profile at 5 MeV energy simulation.

For the sake of completeness we show in Figure 27 the absorbed dose profile at $3\,MeV$ electron beam energy, which describes the absorbed dose behavior in a case between the two considered threshold energies. We can notice that the dose peak is reached in the aluminum body, $D_{peak} = 36.6\,kGy$, and the average aluminum dose is $\overline{D} = 25\,kGy$, which corresponds to a temperature difference of $\Delta T = 27.8\,K$. We also point out that there is an evident blue radiation shadow under the aluminum absorber, as if the lower part of EPS under the calorimeter were almost unirradiated.

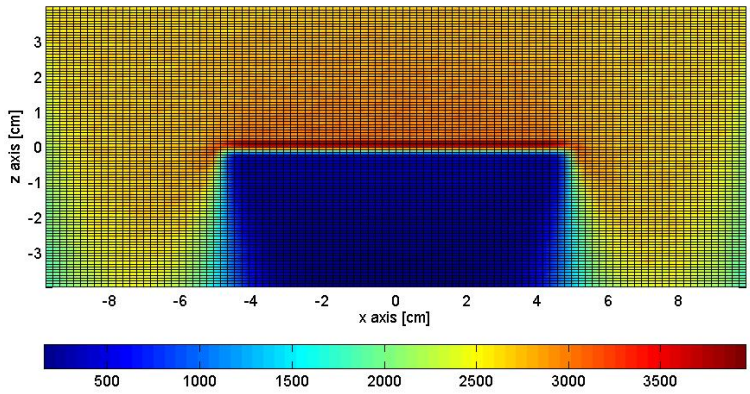

Figure 27 – Absorbed Dose profile at 3 MeV energy simulation.

As a consequence of the whole analysis carried out above, we decide to remove the upper part of the insulation layer, as in [12], because of a low energy range. In fact even though the absorber calorimeter is usually thermally insulated on all sides, as demonstrated in [3], calorimeters for low energy electrons must work without top thermal insulation because of the shorter electron range.

Always inspired by reference [12], as we need an insulation barrier anyway, we establish to seal the top of the cylindrical calorimeter with a very thin aluminized mylar film, whose chemical composition is polyethylene terephthalate, another kind of plastic insulator, and whose density is $\rho = 1.4\ \frac{g}{cm^3}$.

In the end our calorimetric model consists of an absorber body which is wrapped up in an EPS layer only on the lower side and the above system side is covered by an aluminized mylar foil. The $6\ \mu m$ thin mylar foil has a double function: on one side it is an insulator layer, which has to prevent both conduction and convection separating the calorimeter and the above air layer, on the other side it prevents the x-ray penetration due to the accelerated

electron flux; the aluminized characteristic of the mylar foil also prevents the in and out-going of infrared, i.e. heating, very important fact for the right temperature maintenance and measurement.

Monte Carlo simulations: final model

In this paragraph we present the final model evaluated by the Monte Carlo simulator. As we have previously said, we build a calorimeter with a solid absorber body, whose material is aluminum, but as the specific heat capacity could be a changing factor for the different temperatures, we decide to test another reference calorimeter, whose absorber body consists of water, as its specific heat capacity is known with high precision, i.e. $C_{p,H_2O} = 1\ \frac{cal}{g \cdot K} = 4.186\ \frac{J}{g \cdot K}$.

For the aluminum calorimeter we only need an external cover with a mylar foil – aluminized mylar foil thickness is fixed at $6\ \mu m$ – for the whole system, whereas for the water calorimeter we need two foils. The water calorimeter needs one more mylar foil than the aluminum calorimeter, because water is in liquid state and it must be put in a vessel (Petri dish) which has to be covered by a lid, represented in our case by the second aluminized mylar foil. Since the Petri dish has a $89\ mm$ diameter, we set a $9\ cm$ aluminum diameter to render the analysis more similar for the dimension aspect.

In the next two subparagraphs we present the simulations for the two different calorimeters at $1\ MeV$ and $2\ MeV$ electron beam energies.

The following simulations focus only on the thermal analysis within the calorimeter body, because this is the part whose behavior we need to know to get the thermal measurements.

Aluminum Calorimeter

The geometry of the entire system consists of a $5\ cm$ EPS layer thick, where it is embedded in the above centre an aluminum disc, whose diameter is $9\ cm$ and whose thickness is $0.45\ mm$. This thickness is enough to afford the CSDA range at both $1\ MeV$ and $2\ MeV$

energy – namely the CSDA thickness is $0.21\,cm$ at $1\,MeV$ and $0.45\,cm$ at $2\,MeV$. The system is covered by a $6\,\mu m$ aluminized mylar film.

The following Monte Carlo representations of the absorbed dose focus on the calorimeter body and its closer layers: at first there is the aluminized mylar foil ($6\,\mu m$), at second the aluminum calorimeter ($0.45\,cm$) and at last the first millimeters of the EPS layer.

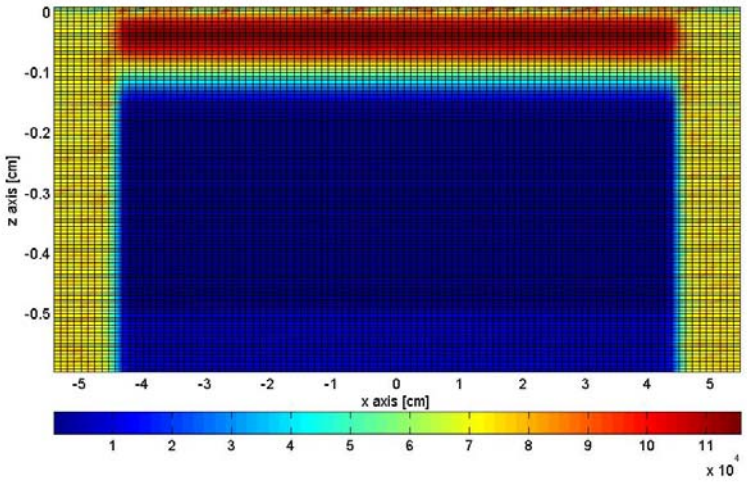

Figure 28 – Absorbed dose profile in the aluminum calorimeter at 1 MeV beam energy (3D plot).

From the colored legend we can see that the absorbed dose peak is reached in the first few millimeters of aluminum. This absorbed dose radiation result is expected, as we model our system for this purpose, so that there is a dark radiation shadow under the aluminum calorimeter, as the graph in Figure 28 gives this hint.

On both lateral sides we can see the first parts of the EPS box; their color is yellow, so that we can understand that this material also absorbs quite a relevant quantity of electrons.

In Figure 29 we extrapolate the dose trend from Monte Carlo data and we remark that the absorbed dose shape of the curve is the typical one in the Radiation Dosimetry field.

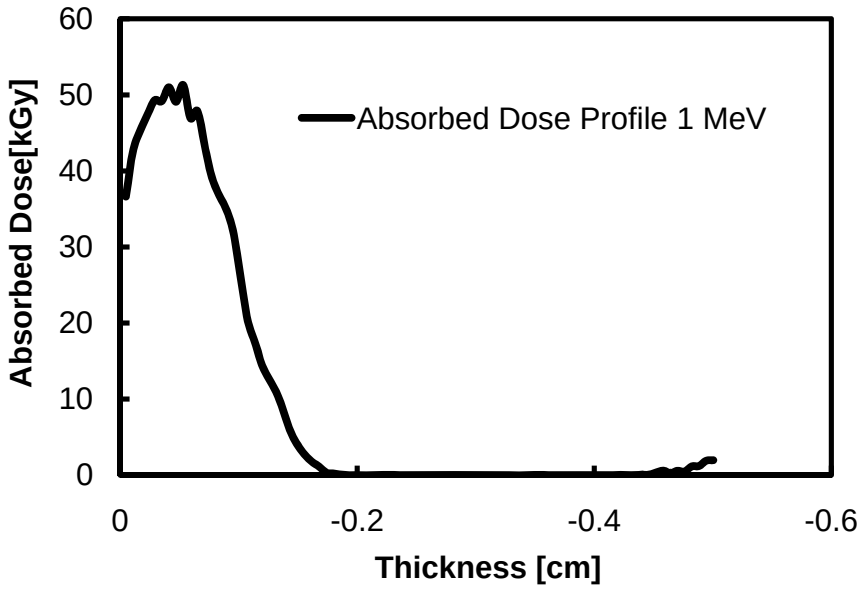

Figure 29 – Absorbed Dose profile versus Thickness in the aluminum calorimeter at 1 MeV beam energy.

The consequence that we can carry out looking at Figure 29, is that the radiation is entirely absorbed within 0.2 cm, where the dose value is close to zero, according to the CSDA range at 1 MeV energy.

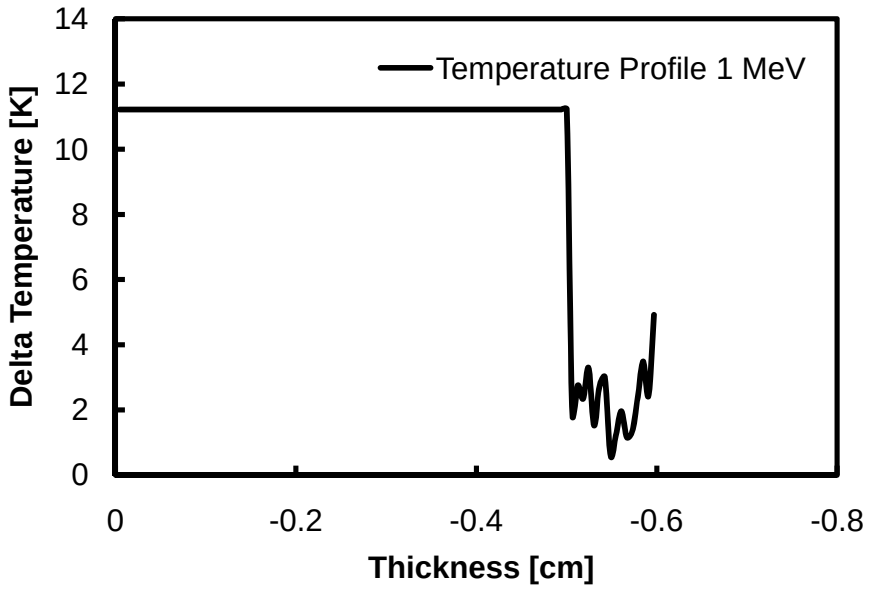

Figure 30 – Delta Temperature Profile versus Thickness in the aluminum calorimeter at 1 MeV beam energy.

In Figure 30 we sketch the average temperature in the aluminum body and the punctual temperature in the first part of expanded polystyrene. We can observe that the average aluminum temperature is constant, as we assume that the difference of temperature distributes in the entire cylinder while reaching the steady-state. The difference of temperature within the absorber is $\Delta T = 11.22\ K$.

Now we analyze the $2\ MeV$ energy case.

The graph in Figure 31 shows the absorbed dose profile at $2\ MeV$ beam energy. Also in this case the dose peak is reached in the first millimeters of the aluminum calorimeter (red color), but a difference with the previous system is that we observe that the hotter electrons impinge a thicker layer of aluminum. This is as we expect because of the higher energy and the bigger CSDA electron range.

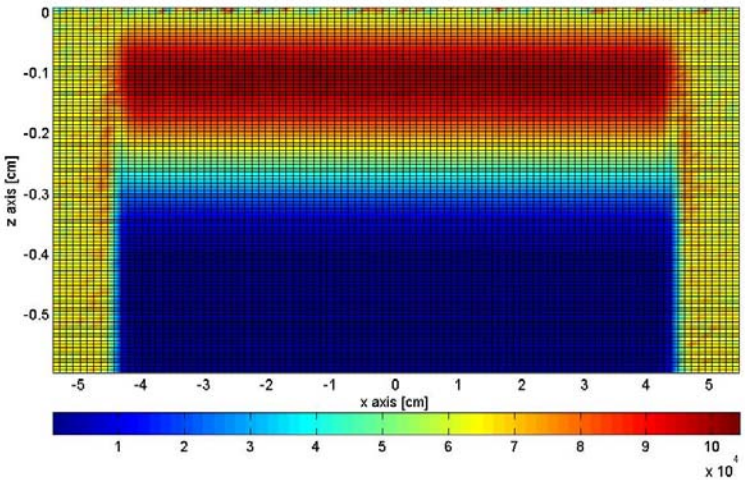

Figure 31 – Absorbed dose profile in the aluminum calorimeter at 1 MeV beam energy (3D plot).

In Figure 32 we extrapolate the dose trend from the Monte Carlo data in Figure 31 at 2 MeV electron beam energy.

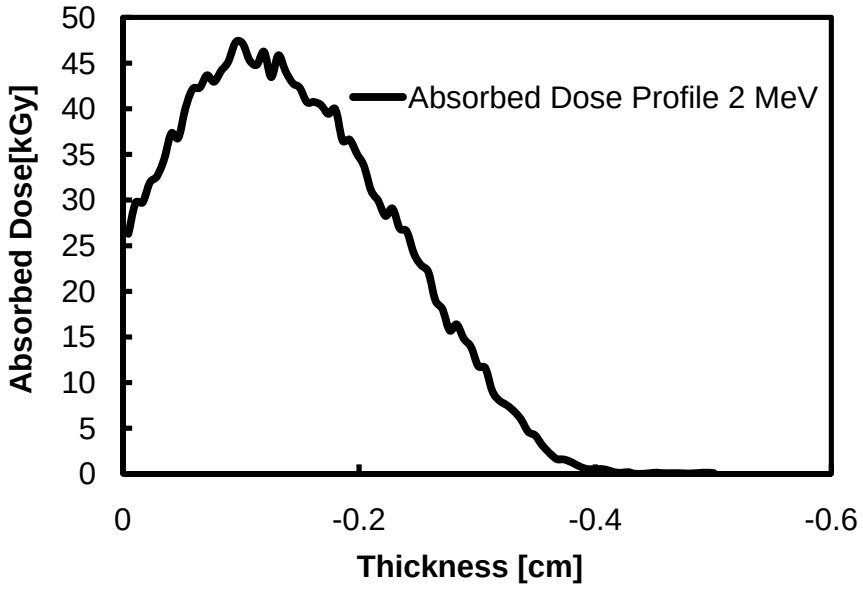

Figure 32 – Absorbed Dose profile versus Thickness in the aluminum calorimeter at 2 MeV beam energy.

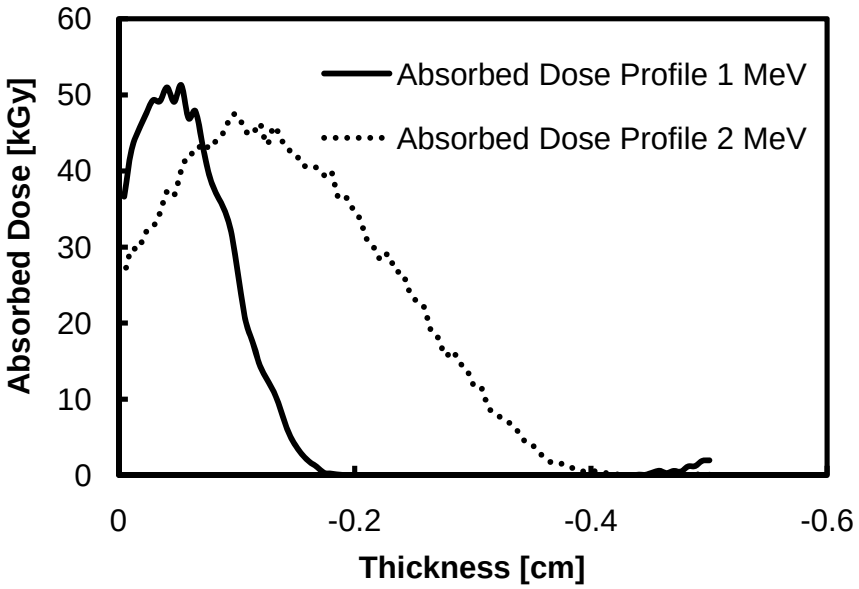

Figure 33 – Absorbed Dose profile Comparison in the aluminum calorimeter at 1 MeV beam energy (solid line) and at 2 MeV beam energy (dot line).

In Figure 33 we plot the absorbed dose profile both at 1 MeV and at 2 MeV electron beam energy. We can notice that the dose trends are the usual ones that are obtained by fitting experimental data. From this graph it can be seen that there is a larger radiation penetration within the calorimeter with increasing beam energies, which means that electrons stop within a deeper layer.

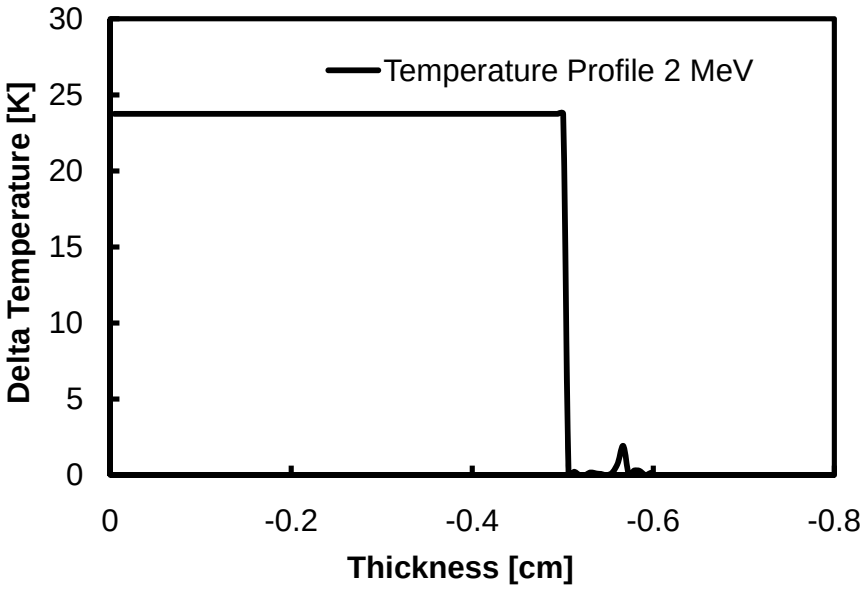

Figure 34 – Delta Temperature Profile versus Thickness in the aluminum calorimeter at 2 MeV beam energy.

As with the previous energy case, in Figure 34 we sketch the average temperature in the aluminum body and the punctual temperature in the first part of expanded polystyrene. The average difference of temperature within the aluminum absorber is $\Delta T = 23.75\ K$.

Since Monte Carlo simulations reproduce the final calorimetric system, it is useful to see the difference between the idealized case (Ansys simulations) and the more realistic one (Monte Carlo data). In Table 6 we summarize the delta temperatures collected by the different data.

Table 6 Comparison of Delta Temperatures between Monte Carlo simulation and Ideal Model for the Aluminum Calorimeter.

Beam Energy	Simulated ΔT	Ideal ΔT	Difference
MeV	K	K	%
1	11.22	13.84	18.9
2	23.75	27.67	14.2

We can observe from Table 6 that the estimated ΔT difference is higher for the lower energy case, as the idealized ΔT only considers the idealized absorber body, without any other parameter losses.

Water Calorimeter

The geometry of the water calorimeter consists of a polystyrene Petri dish, $89\,mm$ diameter, $15.6\,mm$ thick, and $1.06\,\frac{g}{cm^3}$ density, where the water is collocated with $12\,mm$ thickness. As with the aluminum calorimeter, the water absorber is embedded on the bottom part of an EPS layer $5\,cm$ thick. As already explained we have to put two mylar foils: one has the same function as in the aluminum calorimeter, i.e. it has to cover and protect the whole system, while the other mylar foil only covers the Petri dish, so that it works as a lid for the vessel and as an avoider of water bubbles.

The water thickness is more than enough to afford the CSDA range at both $1\,MeV$ and $2\,MeV$ energy because the computed CSDA ranges are: $0.437\,cm$ at $1\,MeV$ and $0.9785\,cm$ at $2\,MeV$, the real problem in this case is the Petri dish thickness.

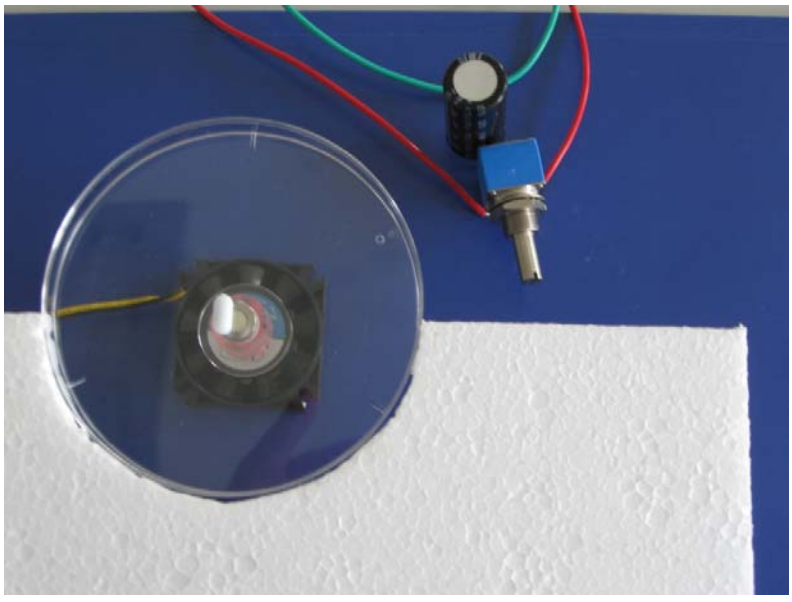

Figure 35 – Water calorimeter design with miniature magnetic stirrer. The focus is on the Petri dish, which contains the permanent magnet and water, on the DC motor (1000 rpm), which makes the magnet spin, and on the starter capacitor that makes the motor drive (rash current).

As shown in Figure 35, the real water calorimeter has quite a complicated structure, as it needs an active forced convection mode for hot and cold water mixing (hot water is due to electron radiation) and a magnet stirrer that has to spin water for the steady-state temperature detection. The water calorimeter design has been completed including a dedicated miniature magnetic stirrer as can be seen in Figure 35.

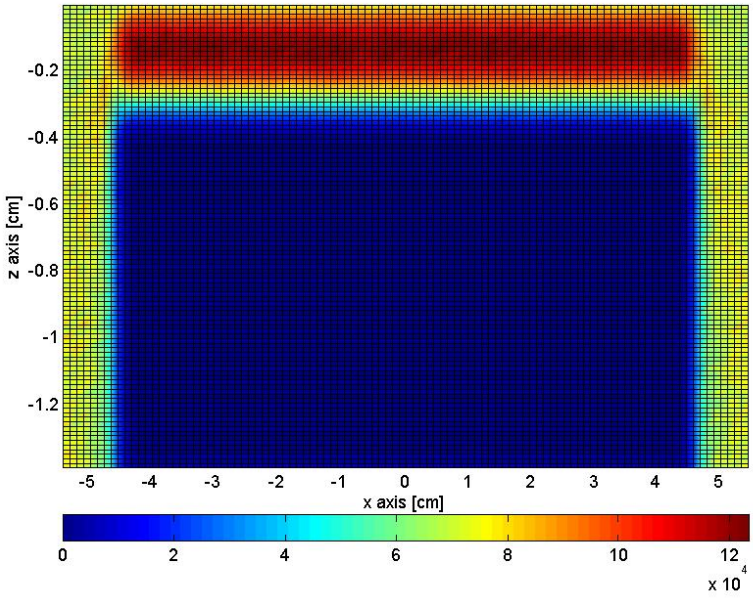

Figure 36 – Absorbed dose profile in the water calorimeter at 1 MeV beam energy (3D plot).

Through the colored legend of Figure 36 we can see that electrons are totally absorbed within 0.4 cm thickness, (according to the CSDA range at 1 MeV); the absorbed dose peak (red) is reached in the first millimeters of water.

In Figure 37 we extrapolate the absorbed dose profile versus the system thickness through the data obtained by Figure 36 (Monte Carlo calculations).

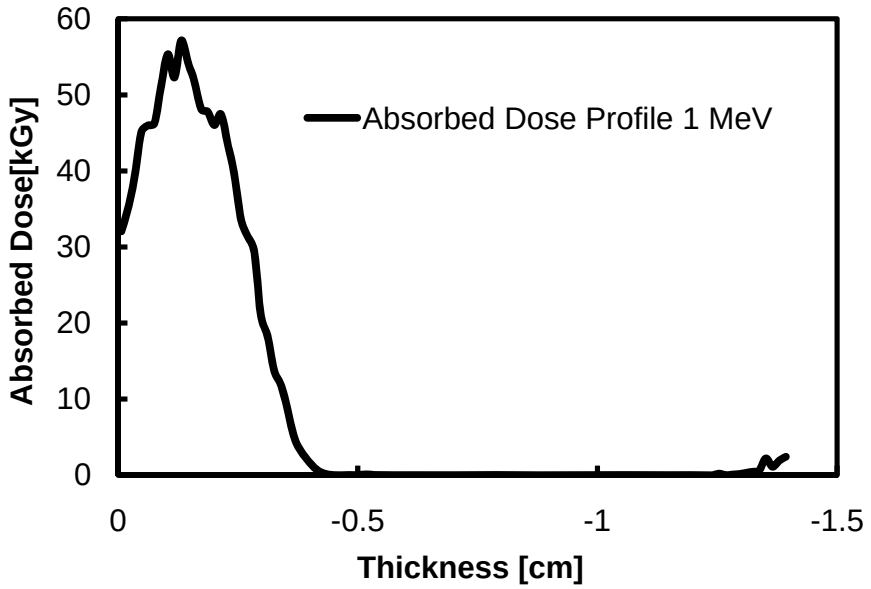

Figure 37 – Absorbed Dose profile versus Thickness in the water calorimeter at 1 MeV beam energy.

In Figure 38 we sketch the average temperature in the water absorber and the punctual temperature in the first part of expanded polystyrene. We can observe that the average water temperature is constant, as we assume that the difference of temperature distributes in the entire cylindrical vessel to reach the steady-state. The difference of temperature within the absorber is $\Delta T = 2.8\,K$.

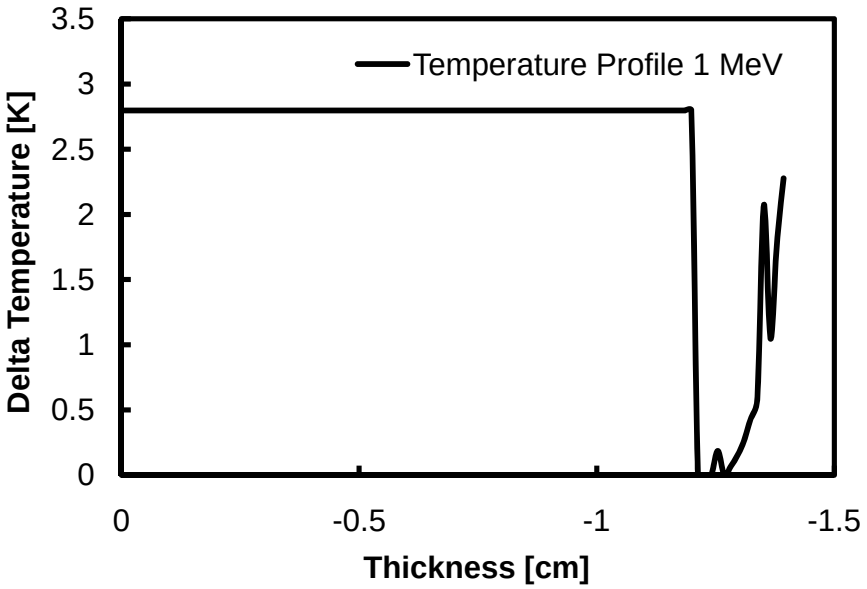

Figure 38 – Delta Temperature Profile versus Thickness in the aluminum calorimeter at 1 MeV beam energy.

Now we analyze the 2 MeV energy case.

The graph shown in Figure 39 represents the 3D absorbed dose profile in the calorimetric system at 2 MeV beam energy. Through the color scale we notice that the electrons are totally absorbed within 0.8 cm thickness (CSDA range in water at 2 MeV) , and the absorbed dose peak (red) is reached in the first millimeters of water.

In Figure 40 we extrapolate the absorbed dose profile versus the system thickness through the data shown in Figure 39.

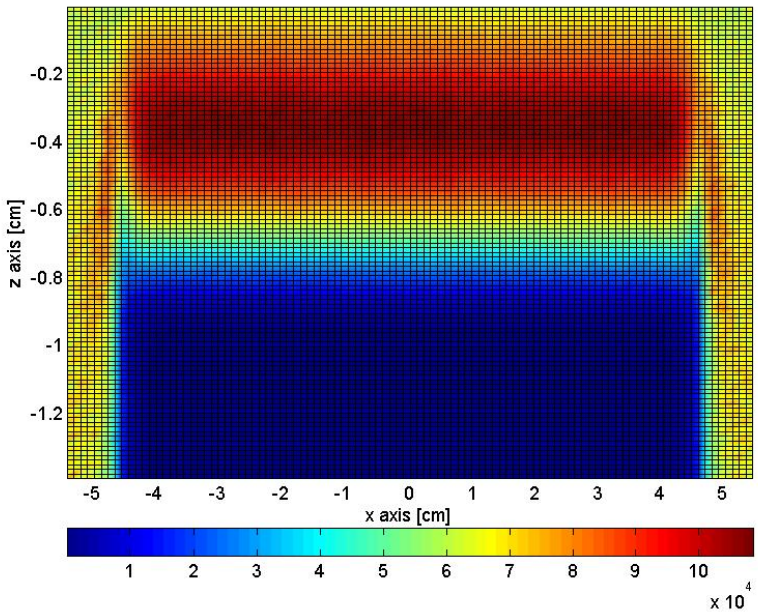

Figure 39 – Absorbed dose profile in the water calorimeter at 2 MeV beam energy (3D plot).

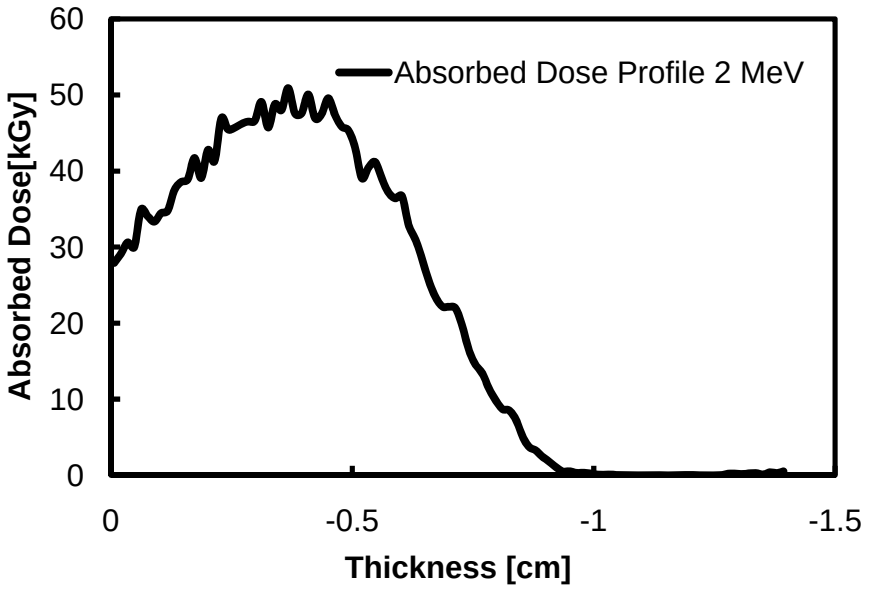

Figure 40 – Dose profile versus Thickness in the water calorimeter at 2 MeV beam energy.

In Figure 41 we plot the absorbed dose profile both at 1 MeV and at 2 MeV electron beam energy. We underline that the dose trends are the characteristic ones that are obtained by fitting experimental data. From this graph it can be seen that there is a larger radiation penetration within the calorimeter with increasing beam energies, which means that electrons stop within a deeper layer.

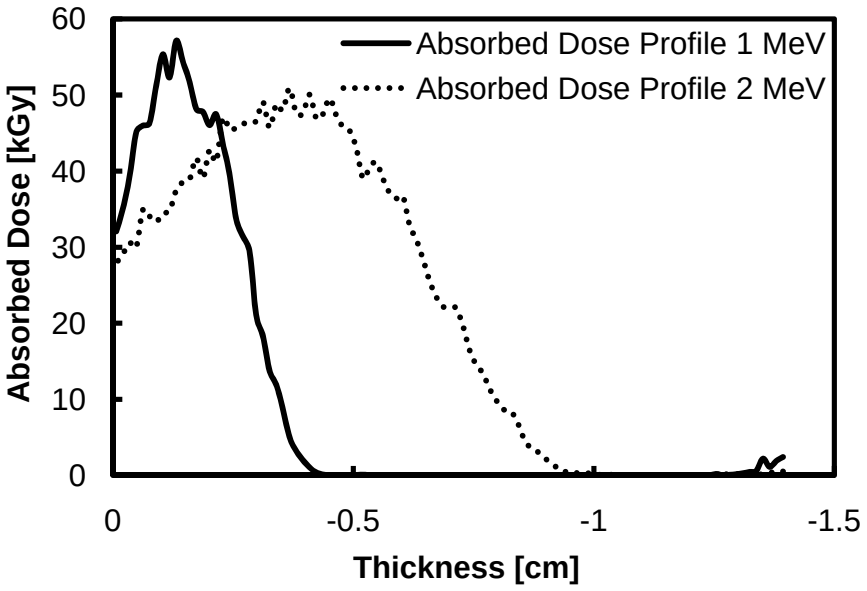

Figure 41 – Absorbed Dose profile Comparison in the water calorimeter at 1 MeV beam energy (solid line) and at 2 MeV beam energy (dot line).

As with the previous energy case, in Figure 42 we sketch the average temperature in the water body and the punctual temperature in the first part of EPS. The average difference of temperature within the absorber is $\Delta T = 5.95\ K$.

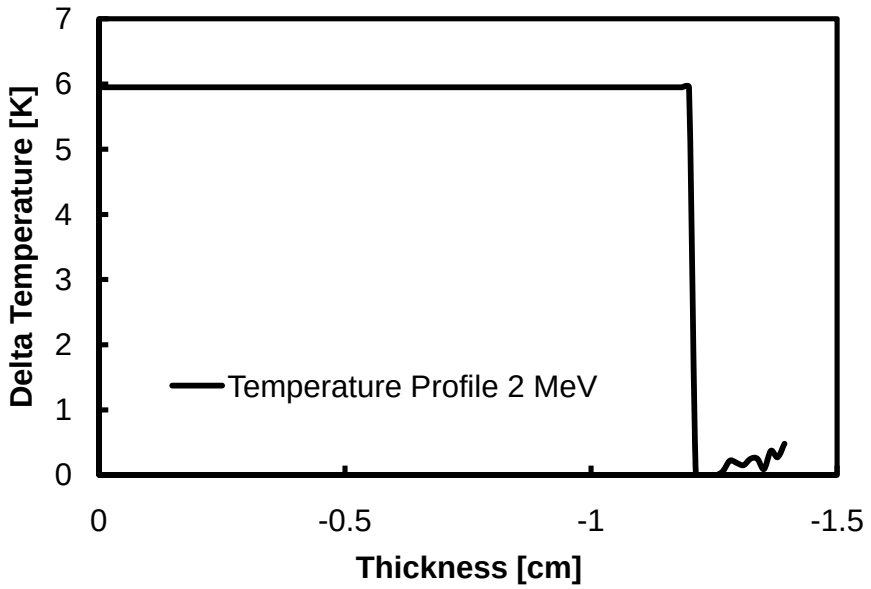

Figure 42 – Delta Temperature Profile versus Thickness in the water calorimeter at 2 MeV beam energy.

Since Monte Carlo simulations reproduce the final calorimetric system, it is worth seeing the difference between the idealized case (Ansys simulations) and the more realistic one (Monte Carlo data), summarized in Table 7.

Table 7 Comparison of the Delta Temperatures between Monte Carlo simulation and Ideal Model for the Water Calorimeter.

Beam Energy	Simulated ΔT	Ideal ΔT	Difference
MeV	K	K	%
1	2.8	3.69	24.1
2	5.95	7.37	19.3

Just as for the aluminum case, for the water case we compute a higher temperature difference for the lower energy case, as reported in Table 7.

Chapter 4 – Global System Design

Hardware design

The global system we physically have to design is composed of an aluminum absorber (9 cm diameter) and an EPS envelope where the calorimeter is embedded, whose physical model and exploded view are collected in Figure 43. Since we need to transport our system for the experimental tests, we need a package (wooden box), which has to include the entire system.

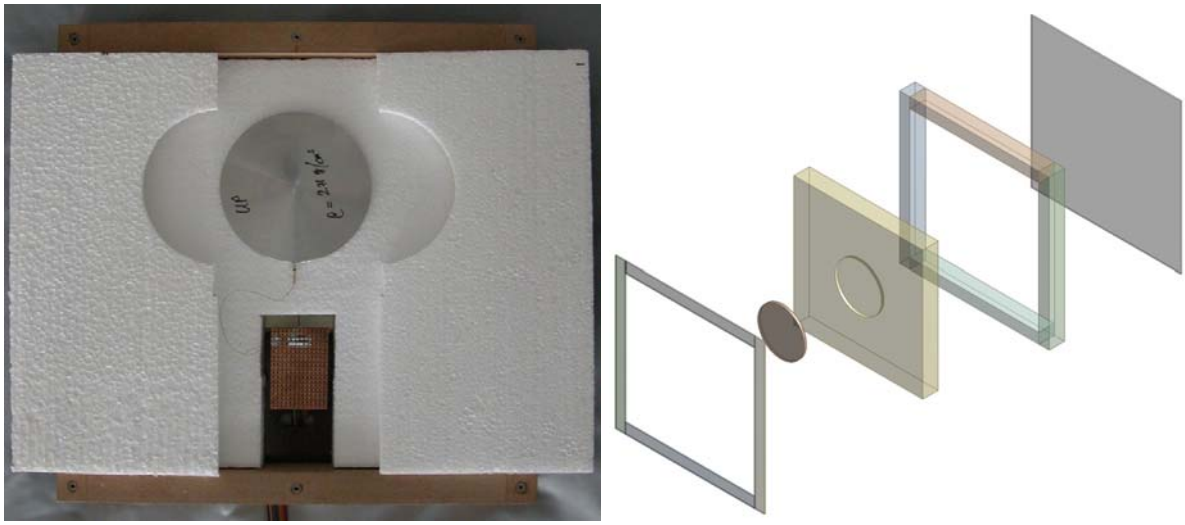

(a) (b)

Figure 43 – (a) Internal view of the calorimetric system: wooden box expanded polystyrene layers, aluminum cylinder absorber. (b) Exploded view of the integral dose calorimeter.

The wooden box is $29\,cm \times 29\,cm$ large, it has a $2\,mm$ thick bottom and a $2\,cm$ large lateral edge, so that the internal area results $25\,cm \times 25\,cm$. The overall wooden box thickness is $3\,cm$, in order to build a suitable system to let the calorimeter pass under the

scanner window. The large lateral edge is necessary for the calorimeter closure: the lid consists of a square frame with $29\,cm$ external side and with $25\,cm$ internal side. To complete the enclosure, we add eight holes at the vertices and at the half sides of both the lid and the box, as we need to seal the calorimeter with eight screws by joining the aluminized mylar foil between the lid frame and the box.

The design of the aluminum absorber has already been discussed in Chapter 2, but now we have to describe how the thermal sensor has been embedded inside the calorimeter. As the thermistor probe is extremely small and sensitive, whose dimensions are collected in Figure 44, we decide to insert it in a plastic capillary ($1.5\,mm$ diameter) and make a hole in the absorber of $3\,cm$ length (departing from the circular boarder) and $1.6\,mm$ diameter to insert the probe within the aluminum. To protect the thermal sensor as much as possible, we collocate the capillary next to the CSDA range at $1\,MeV$ electron beam energy in the thickness direction, i.e. $1.7\,mm$ far from the upper aluminum surface, so that the sensor should not be damaged by the electron radiation.

For the insulation layer we use two square slabs $2\,cm$ and $1\,cm$ thick. In order to reduce the contribute of conductive heating, we do not place the aluminum absorber just above the first $2\,cm$ thick EPS slab, but we make it lay on three nails; the second EPS slab has a circular hole to fit the aluminum disc.

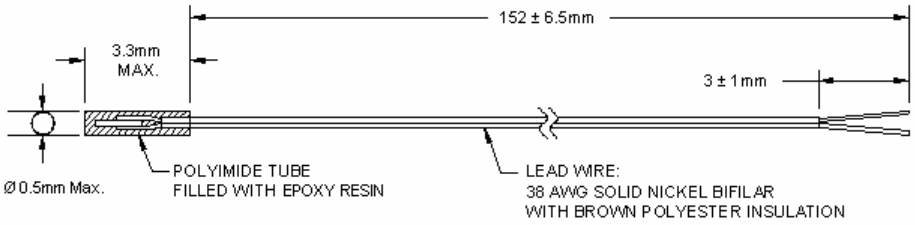

Figure 44 – Micro-BetaCHIP thermistor probe: materials and dimensions.

The Cad sketches used to build the calorimetric system are reported in Appendix – A.2.

Instrumentation Description

In this paragraph we outline the characteristics of the instrumentation and the connections needed during the data collection.

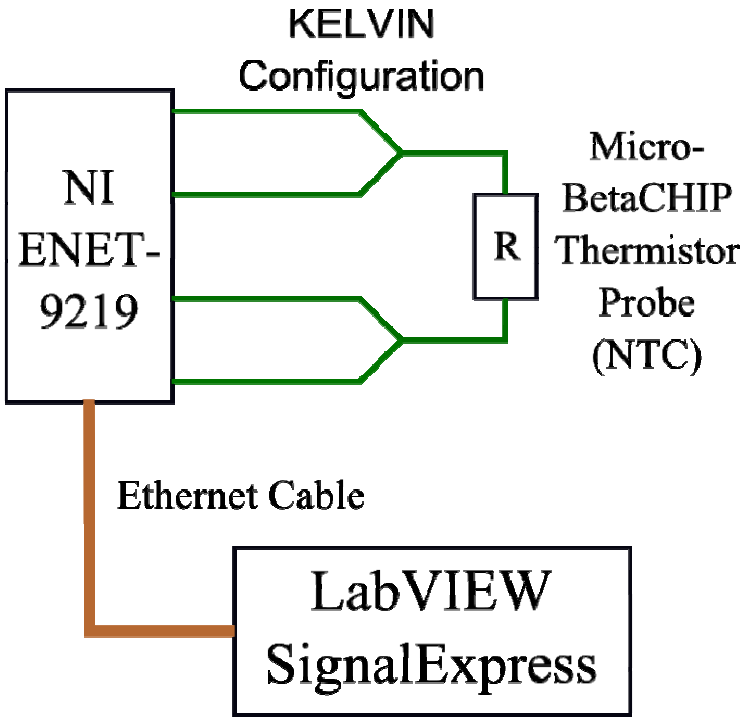

Figure 45 – Block diagram of the electronic instrumentation connections.

In Figure 45 we sketch a block diagram of the entire system connections. The measurement begins with the Micro-BetaCHIP Thermistor probe, which is connected to the data-logger NI ENET-9219 through four wires for a Kelvin configuration measure (in order to neglect the resistance wires contribute). Finally, to acquire the temperature data through a software remote control (as the calorimeter is in the accelerator shelter), the acquisition data device is linked through a long Ethernet cable to a PC, which is user interfaced through LabVIEW SignalExpress software.

Micro-BetaCHIP Thermistor Probe MCD series

The thermal sensor [13] we have chosen is a Micro-BetaCHIP Thermistor, which is a NTC (Negative Temperature Coefficient) thermistor, whose value at 25℃ is $10\ k\Omega$. From Figure 44 we see the small dimensions of the probe and its construction materials.

We have chosen this sensor for different reasons, that may be found in the device datasheet [13]: the first is the dimension, as we cannot employ too much space inside the cylinder absorber (otherwise this term is not negligible compared to the rest mass contribute), the others are that it has a rapid time constant ($200\ ms$ in liquids), it has a wide temperature range from -40℃ to $+125$℃, the guaranteed tolerance is ± 0.2℃ from 0℃ to 70℃, and it has a dissipation constant in air at 25℃ of 0.3 $\frac{mW}{℃}$. In addition the small mass of the unit allows the sensor to respond very rapidly to temperature changes.

The thermistor measures a resistance value, which has to be converted into a temperature one: in its datasheet is provided the resistance versus temperature table at 1℃ step. As during the measuring process we need a continuous curve to obtain a simultaneous temperature value, we have to derive an interpolation curve expression, given in equation (12):

$$T[℃] = 10^{[A\cdot(log_{10}R)^2 + B\cdot(log_{10}R)+C]} - 273.15 \qquad (12)$$

where $A = 0.0053$, $B = -0.1196$, and $C = 2.8682$ are proportional coefficients established for the resistance to temperature conversion.

The two final extremely thin BetaCHIP wires are connected to an electrical board where the two wires become four in a flat ribbon cable, as we want to carry out a 4-wires measure (Kelvin configuration), since it is more accurate than the 2-wires one, because it avoids the wire-resistance contribute computation.

NI ENET-9219

Figure 46 – On the left is represented the calorimetric system covered by the aluminized mylar foil. On the right is represented NI ENET-9219 data logger with relative connections.

Our data acquisition instrument is a NI ENET-9219, depicted in Figure 46, by National Instruments [14], which is an Ethernet 4-channels universal input device that can acquire several data types. It includes four simultaneously universal measurement channels for multipurpose testing, such as strain gages, RTDs, thermocouples, load cells, and other power sensors. In our system, NI ENET-9219 has the function of acquiring data from the Micro-BetaCHIP thermistor, through which is connected by a flat cable.

From the datasheet characteristics of the DAQ (Data Acquisition acronym) device [14], we have to point out that the maximum input range of the 4-wires resistance is up to 10.5 $k\Omega$, so that we need a minimum temperature of 24℃ to reveal any measure, because otherwise the instrument saturates.

NI ENET-9219 has different methods for data acquisition: high speed (20 ms), best 60 Hz rejection (120 ms), best 50 Hz rejection (140 ms), and high resolution (510 ms). For the resistance measurement the internal peak current provided by the instrument is 500 μA and, as we need a quite fast and accurate data collection (we acquire the data during the

calorimeter irradiation), we compare the high resolution and high speed ways, considering: data speed sampling, self heating thermistor, and resolution matters. In the high resolution acquisition the current pulse is $510\ ms$ long, while in the high speed it is $20\ ms$ long. The main difference lies in a longer current pulse for the high resolution case, whereas in the high speed case the current pulse is shorter, but it is repeated more frequently to get a faster measurement. Since we need quite a rapid sampling, we impose to collect one value every $200\ ms$, so that we must use the high speed acquisition mode evaluating a 10% duty cycle. Even for the self heating of the thermistor the high speed mode appears the most suitable mode, as its duty cycle characterization (10% high speed versus 100% high resolution) lets us estimate an overheating peak of $8.7 \cdot 10^{-2} K$, while for the high resolution mode it would be $8.7\ K$, causing intrinsic problems in the calorimeter temperature evaluation. Concerning the resolution we have tested the instrument with some easy models, carrying out that the high speed mode has a sufficient resolution for our aim.

The calorimetric system and NI ENET-9219 are located in the accelerator shelter. In order to prevent electron radiation damage we provide a shielded box where the DAQ system is assembled, and in order to acquire data through a remote control we provide a $30\ m$ Ethernet cable for the data-logger to PC connection, as the computer is collocated outside the accelerator shelter.

Remote Control Software: LabVIEW SignalExpress

The software that we use for the data acquisition process is LabVIEW SignalExpress (National Instruments), which is needed for the project configuration and for the data logger settings. Through LabVIEW SignalExpress we acquire the resistance value through the thermistor probe, and the temperature value for the resistance to temperature conversion using equation (12). The data logger is finally connected to a computer where we define the project and where we collect all the temperature data through a $30\ m$ Ethernet cable.

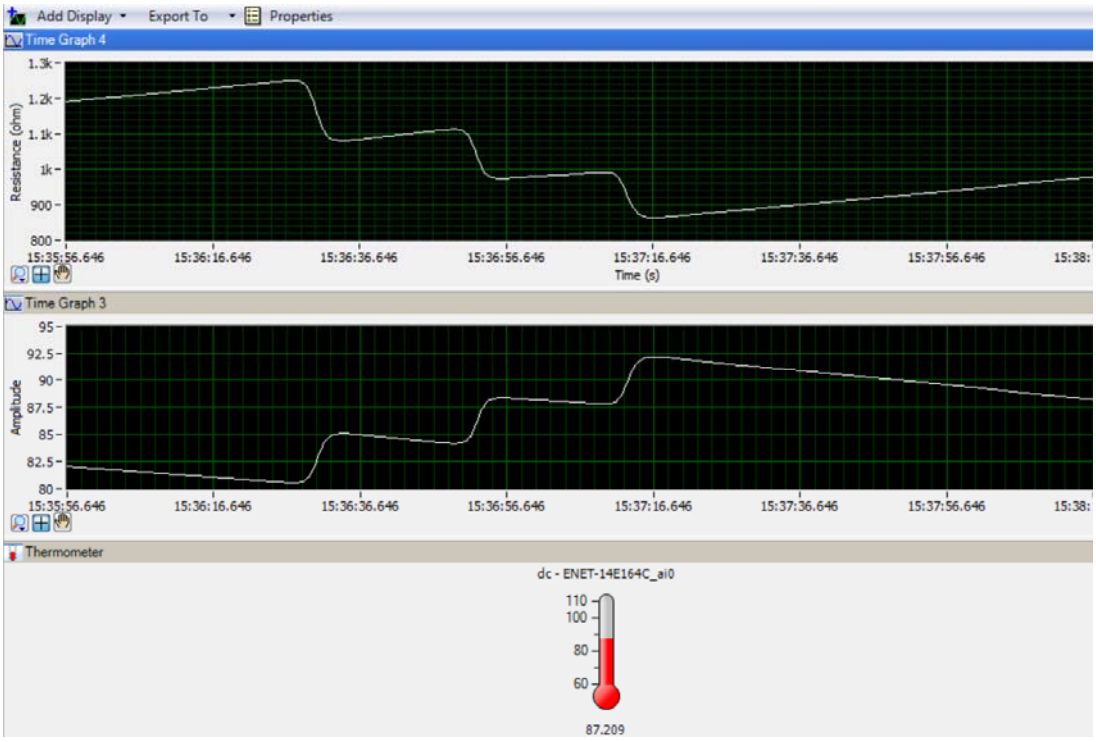

Figure 47 – LabVIEW SignalExpress screen shoot is divided into three parts: the first panel represents the resistance values acquisition, the second the temperature conversion, and the third is a thermometer for the instantaneous temperature indication.

In Figure 47 we enclose a LabVIEW SignalExpress screen shoot, where a measure example is represented. We want to point out the three panels division: the first acquired value is the resistance one (first black panel), then we convert it into a temperature value through equation (12) (second black panel), and in the end we insert a thermometer, which has the function of revealing the instantaneous Celsius temperature during data acquisition. We have to underline two details shown in Figure 47: the first is that we can observe that the calorimeter passes under the electron beam three times, as there are three steps, the second consists of the negative thermal coefficient of the thermistor, as we can see that if the resistance value decreases, the temperature value increases. As shown in Figure 47, when the calorimeter has a higher temperature than its surrounding environment, the thermal sensor measures a temperature decrease, the cooling slope effect, which must be corrected and compensated during the data analysis phase.

Thermal Sensor Calibration

The Micro-BetaCHIP thermistor probe, as thermal sensor, requires a calibration test, to check if the temperature we acquire through the thermal sensor inside the calorimeter is the same of another imposed heat source. To prove this fact, we need an already calibrated instrument as heating source; the one we use is a “Thermochuck”.

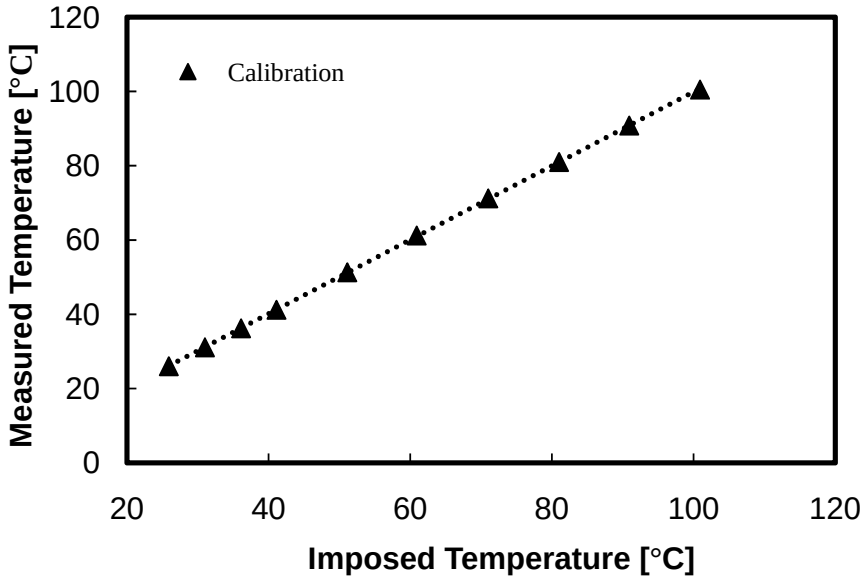

Figure 48 – Calibration curve of the Micro-BetaCHIP thermal sensor. In triangle markers are plotted the experimental data, connected with a straight line (dots).

In Figure 48 we plot the Calibration curve of the Micro-BetaCHIP sensor, which describes the correlation between the imposed temperature of the heat source and the measured one. As we can see from Figure 48, the experimental markers (triangle) are perfectly matched in a straight line (dots), whose expression is $y = 0.9954x + 0.3339$, and whose minimum square term is equal to one $R^2 = 1$, so that all the data lie on this line. The evaluated slope $m = 0.9954$ is almost one and the difference of these two values is less than 1%; we can explain this behavior taking into account the stochastic tolerance of the probe, whose value is $\pm$ 0.2 ℃. Since the experimental thermistor data match with the heat source, we are able to assert that the thermistor works in the right temperature range and it does not need any other calibration or correction factors.

Electron Energy Extrapolation

Basically starting from the measured difference of temperature through the calorimeter we want to reconstruct the impinging electron energy. To achieve this goal, we write a Matlab file, attached in Appendix – A.3, in which we rearrange the mathematical expression (8) to obtain the interested energy values. Besides the energy values, we estimate the possible error sources, which are the subject of the following paragraph.

Rearranging equations (6) and (8) for 1 cm^2 area, we obtain (13).

$$E_{TOT} = C_p \cdot m_{TOT} \cdot \Delta T_{TOT} = C_p \cdot t_{TOT} \cdot \rho \cdot \Delta T_{TOT} = \frac{E_B \cdot I_B \cdot \Delta t}{A_{irr}} \quad (13)$$

where E_{TOT} is the total energy absorbed energy $[J]$, C_p specific heat capacity $\left[\frac{J}{g \cdot K}\right]$, ΔT_{TOT} total difference of temperature $[K]$, ρ material density $\left[\frac{g}{cm^3}\right]$, A_{irr} irradiated scanned area $[cm^2]$, I_B beam current $[mA]$, Δt scanning time $[s]$, and E_B beam voltage/electron energy $[kV]$ at the calorimeter surface.

Finally the detected electron energy evaluation (without error corrections) is reported in equation (14).

$$E_B = \frac{A_{irr}}{I_B \cdot \Delta t} \cdot C_p \cdot t_{TOT} \cdot \rho \cdot \Delta T_{TOT} \quad (14)$$

In the case of the aluminum calorimeter in conjunction with standard measurement procedures equation (14) becomes (15):

$$E_B = 722.8 \cdot \frac{\Delta T_{TOT}}{I_B} \quad (15)$$

Systematic and Random Errors

Every experimental measurement is affected by an inevitable degree of uncertainty, which does not depend on the accuracy of the measuring method. For this reason, when acquiring

experimental data, we have to take into account the main error contributes of the system we build.

There are two principal groups of errors: the systematic and the stochastic ones. The systematic errors are the ones that are always committed during the measurement and can be deeply predicted analyzing the system under discussion; whereas the stochastic ones, as they are random, are committed by chance.

The main contributes to systematic errors in the calorimeter are:

- Mylar Absorption
- Electron Backscattering
- Boundary Escapes
- Bremsstrahlung Emission.

While the stochastic errors are represented by:

- Micro-BetaCHIP thermistor Tolerance
- Interpolation Error.

All the estimated errors are discussed in the following subparagraphs and are collected in a Matlab file in Appendix A.3.

Mylar Absorption

The first error contribute we have to take into account is the mylar absorption, as the aluminized mylar foil covers the aluminum calorimeter. We compute this error through ESTAR data Software: knowing mylar Stopping Power $\left[\frac{MeV \cdot cm^2}{g}\right]$ at different energy values and its thickness (our foil is 6 μm thick) $t_m = 1.5 \times 10^{-3}\ \frac{g}{cm^2}$, so that multiplying these two terms we obtain the energy loss due to mylar absorption. To render easier the analysis we derive a sixth degree polynomial trendline that we plot in Figure 49 and whose expression is $y = 0.0502x^6 - 0.5607x^5 + 2.5471x^4 - 6.0688x^3 + 8.1083x^2 - 5.851x + 4.357$ (x is the electron beam energy and y is the mylar energy loss in keV), which approximates the

data state quite well, as the minimum square coefficient is $R^2 = 0.9999$. From Figure 49 we want to underline the fact that the mylar absorption describes a very low energy loss, as we could find a very thin foil.

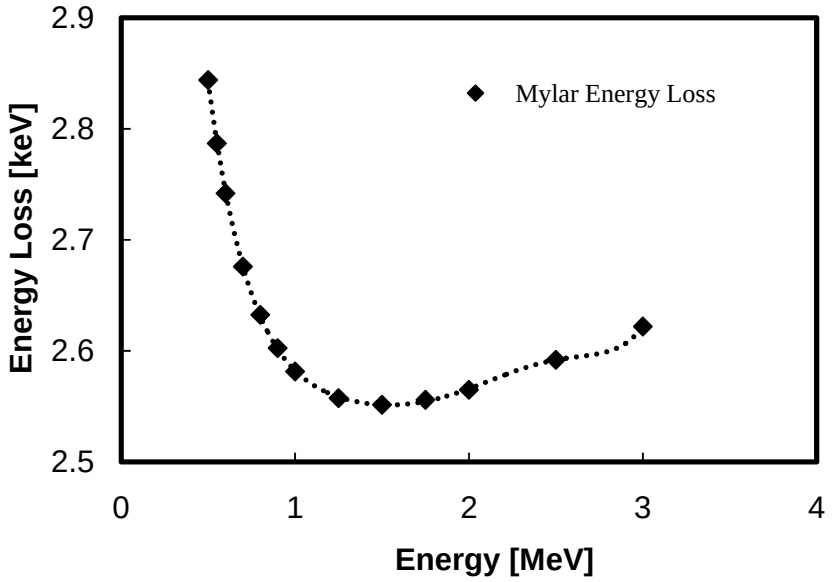

Figure 49 – Mylar Energy Absorption in 0.5-3 MeV electron beam energy range.

Electron Backscattering

When electrons are accelerated and travel towards a target, it happens that some of them are deflected, that means that the incident particles are deviated of an angle greater than 90° relative to the original propagation direction.

In evaluating the backscattering contribute we collect the data trough a Monte Carlo simulation, and we derive a fourth degree polynomial interpolation that we plot in Figure 50. Its expression is $y = 0.0407x^4 - 0.4136x^3 + 1.9788x^2 - 5.4835x + 7.9465$ (x is the electron beam energy and y is the percentage of energy loss due to backscattering events), which approximates the data state quite well, as the minimum square coefficient is $R^2 = 0.9997$. For instance for standard applications at $1\ MeV$ electron beam energy, the electron backscattering coefficient is 4% of the impinging electron energy, that constitutes the highest contribute in the energy loss, than all the other types of errors.

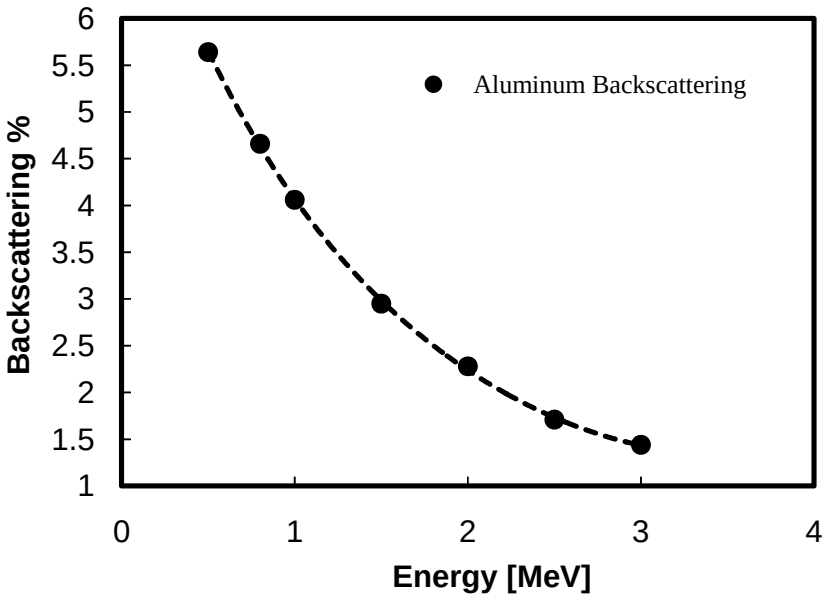

Figure 50 – Percentage Backscattered electrons in 0.5-3 MeV electron beam energy range.

Boundary Escapes

The Boundary Effect consists of electrons that for several reasons do not entirely depose their dose within the absorber. These particles are mainly: the lateral ones that arrive with an oblique trajectory and pass through the target releasing only a part of their energy, particles that may go out of the absorber because of electron path scattering through a mean, and electrons which impinge the absorber sideways.

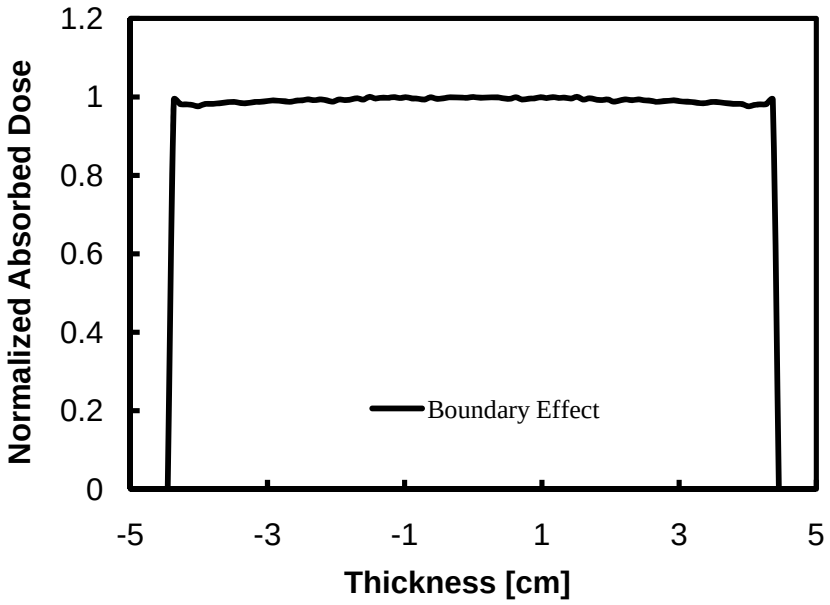

Figure 51 – Boundary Effects of the aluminum calorimeter centered in the 0 coordinate of x axis, 9 cm diameter. The y axis represent the normalized absorbed dose.

From the Monte Carlo simulation, whose data are presented in Figure 51, we estimate the boundary contribute in -1%, computing the difference between the absorbed dose at the sides and in the middle of the model. As we can see from this figure, the normalized absorbed dose has a peak on both calorimeter sides, which means that there are more electrons that enter and depose their energy at the target side, than electrons that go out of it. For this reason the evaluated boundary contribute has to be subtracted from the acquired energy value.

Bremsstrahlung Emission (Radiation Yield)

When charged particles are under acceleration it may happen that they emit X-ray radiation due to different processes that transform electrons in photons sharing energy. This coefficient is evaluated by ESTAR radiation yield and it is estimated with a 1% energy loss of the impinging electron energy.

Micro-BetaCHIP Tolerance

Our thermal sensor has a provided tolerance of $\pm$ 0.2℃ in the temperature reading, value that has to be counted as a random error for the energy evaluation.

Interpolation Error

The DAQ system acquires resistance data and then converts them into a temperature trend through equation (12). The random error that may be committed for the interpolation curve conversion is estimated in 0.4% of the impinging electron energy from internal measurements.

Chapter 5 – Experimental Results and Discussion

Data Acquisition

When we start with the calorimeter tests, we put it on the conveyor that has the function of passing under the electron beam with a constant speed of 5.5 $\frac{cm}{s}$. We prove three beam voltages, namely 0.6 MV, 0.8 MV, 1 MV, and two beam currents, i.e. 5 mA and 10 mA.

In the next graphs are shown the acquired temperature trends by the Micro-BetaCHIP sensor (solid line), and the same data corrected by the initial cooling slope (dots). We may analyze three or six passages under the accelerator, as we want to test its response (linear, non-linear, proportional).

From now on we will discuss how the different tests have been conducted and finally we summarize all the data in Table 8.

In Figure 52, Figure 53, and Figure 54 are collected the tests conducted respectively at 1 MV, 0.8 MV, and 0.6 MV electron beam voltage nominal values with the same rated beam current of 10 mA. For each test we establish three passages and from these figures we can see that each temperature step has about the same amplitude for each case, but, to render a more precise analysis, we always take the average value (ΔT_{total} divided by the number of passages). In this way we may confront the differences of temperature (in similar boundary conditions), even though the number of passages of the calorimeter under the scanner may not be the same.

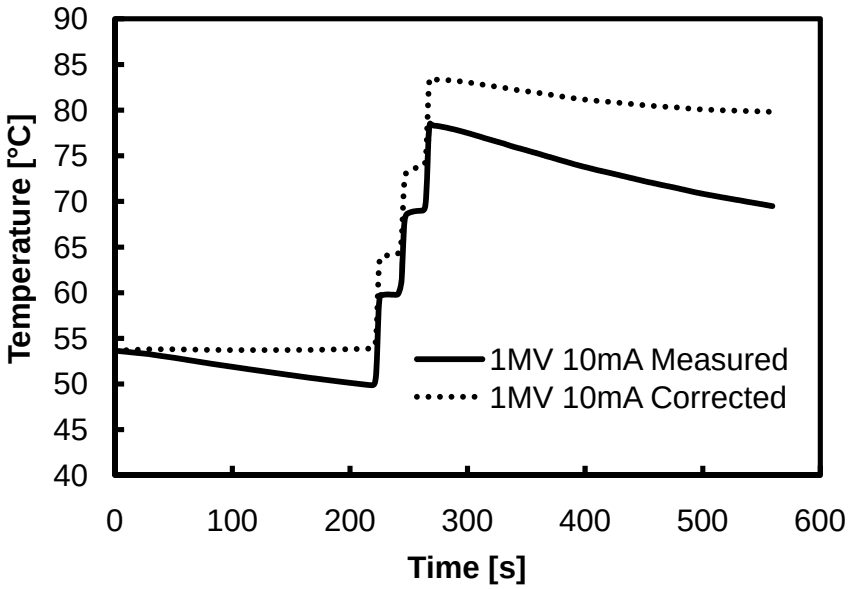

Figure 52 – Calorimeter Experiment at 1 MV beam voltage and 10 mA beam current. The experimental data are presented in solid line, while in dot line the experimental data are corrected by the initial cooling slope. The calorimeter passes three times under the electron beam, as the three steps testify.

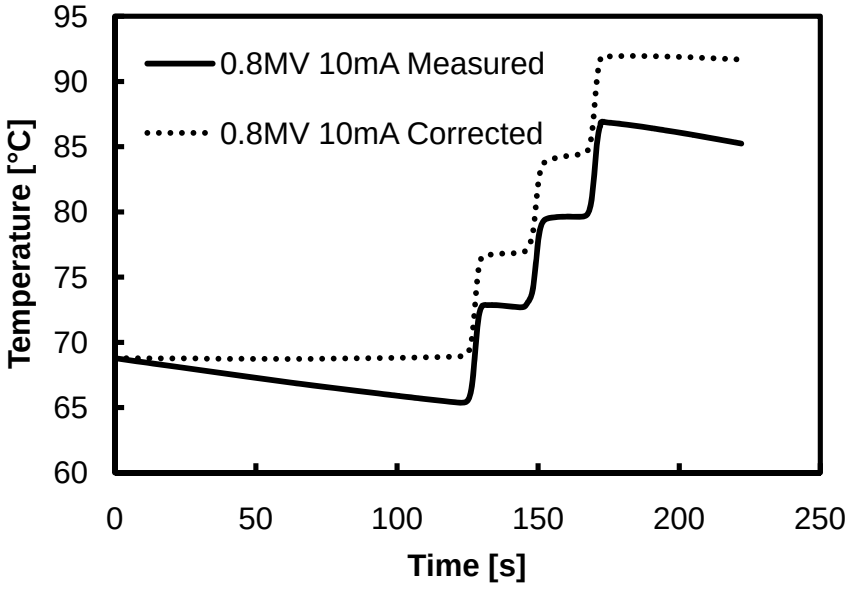

Figure 53 – Calorimeter Experiment at 0.8 MV beam voltage and 10 mA beam current. The experimental data are presented in solid line, while in dot line the experimental data are corrected by the initial cooling slope. The calorimeter passes three times under the electron beam, as the three steps testify.

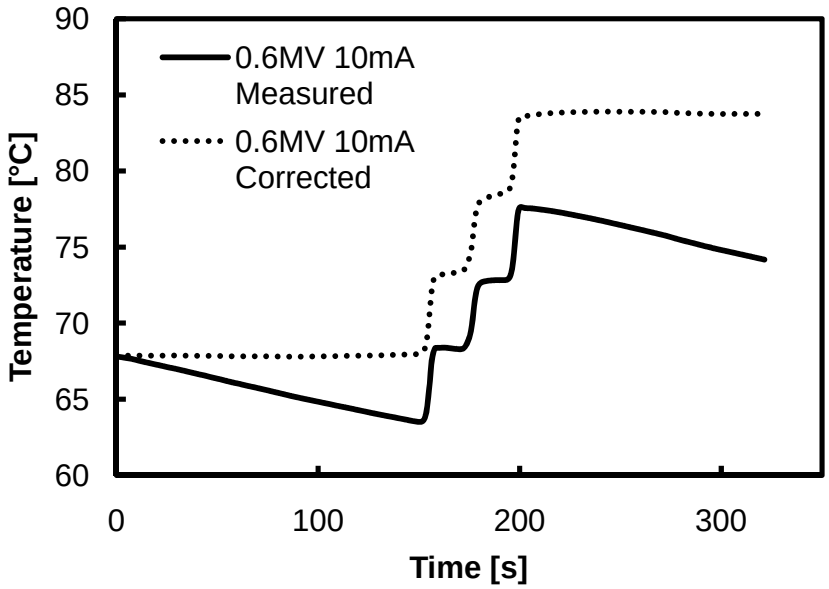

Figure 54 – Calorimeter Experiment at 0.6 MV beam voltage and 10 mA beam current. The experimental data are presented in solid line, while in dot line the experimental data are corrected by the initial cooling slope. The calorimeter passes three times under the electron beam, as the three steps testify.

In Figure 55, Figure 56, and Figure 57 are reported the tests conducted respectively at $1\ MV$, $0.8\ MV$, and $0.6\ MV$ electron beam voltage nominal values with the same rated beam current of $5\ mA$. Also in this case, in every figure the measured difference of temperature at each step consists of almost the same value. We remark that for the $1\ MV$ and $0.6\ MV$ we have chosen six passages, while for the $0.8\ MV$ case we have left three. We underline the fact that the different number of passages has been tested to prove the accelerator behavior.

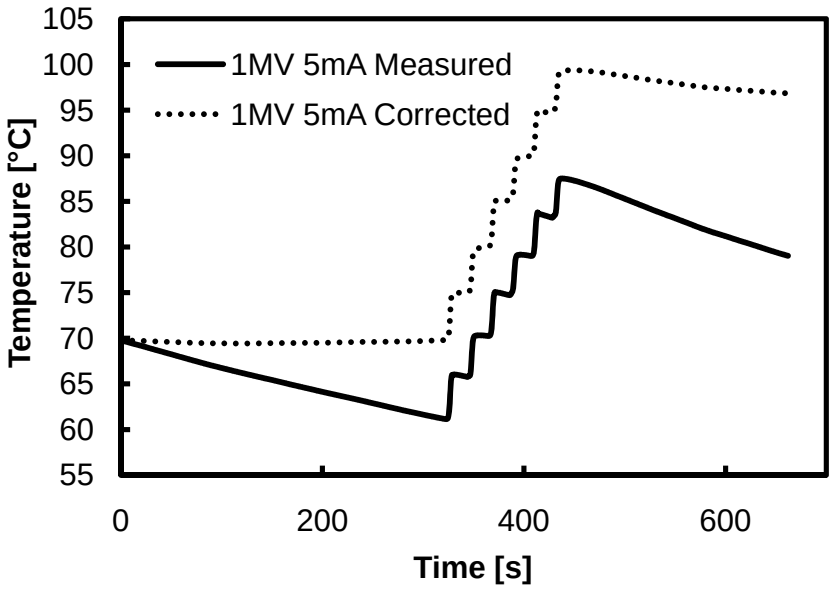

Figure 55 – Calorimeter Experiment at 1 MV beam voltage and 5 mA beam current. The experimental data are presented in solid line, while in dot line the experimental data are corrected by the initial cooling slope. The calorimeter passes six times under the electron beam, as the six steps testify.

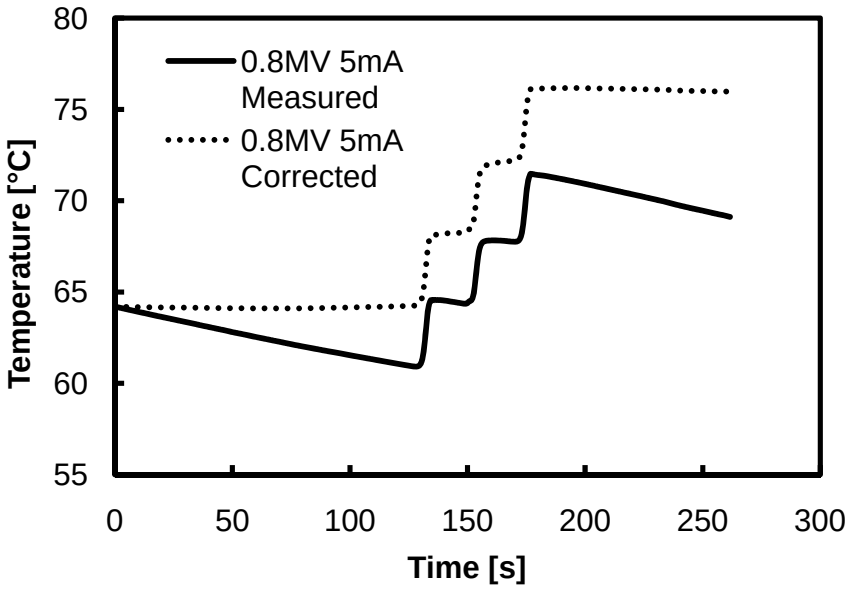

Figure 56 – Calorimeter Experiment at 0.8 MV beam voltage and 5 mA beam current. The experimental data are presented in solid line, while in dot line the experimental data are corrected by the initial cooling slope. The calorimeter passes three times under the electron beam, as the three steps testify.

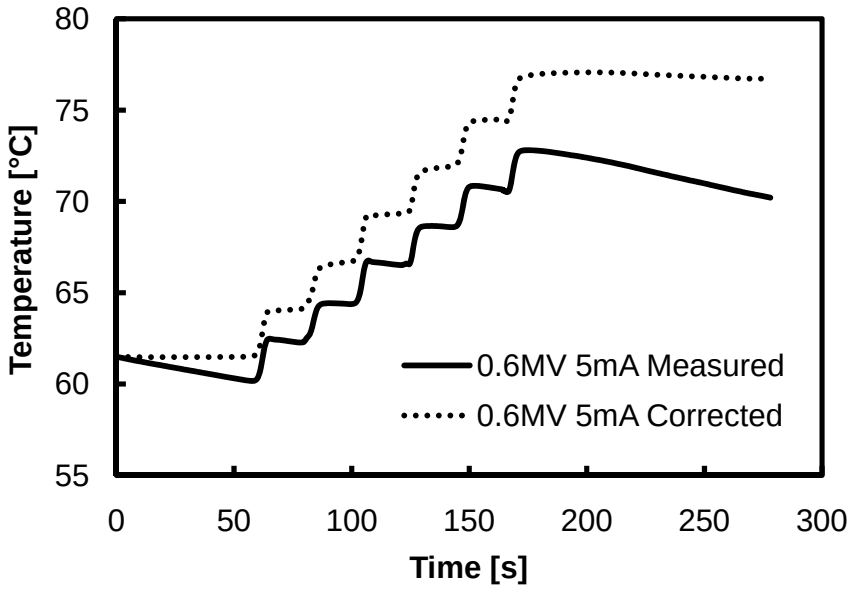

Figure 57 – Calorimeter Experiment at 0.6 MV beam voltage and 5 mA beam current. The experimental data are presented in solid line, while in dot line the experimental data are corrected by the initial cooling slope. The calorimeter passes six times under the electron beam, as the six steps testify.

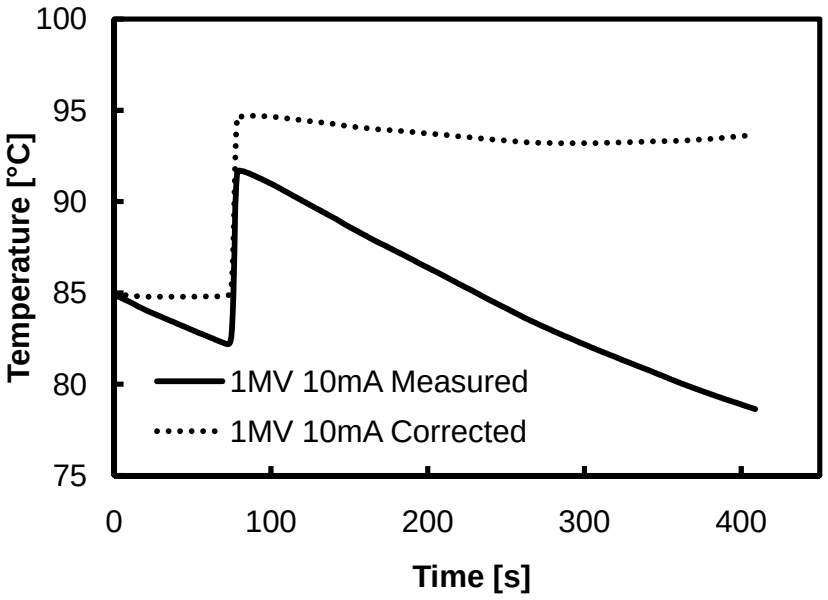

Figure 58 – Calorimeter Experiment at 1 MV beam voltage and 10 mA beam current. The experimental data are presented in solid line, while in dot line the experimental data are corrected by the initial cooling slope. The calorimeter passes once under the electron beam, as the only step testify.

In the end we decide to repeat just one passage of the calorimeter under the electron beam, as shown in Figure 58, to reveal the repeatability of the test. In fact, as Table 8 proves, the average ΔT is very close to the one of the first test with three passages in the same voltage and current conditions (rated nominal values: 1 MV, and 10 mA).

All the data collected through the experiments and the corrected beam energy values given by the elaborated Matlab file (Appendix – A.3) are reported in Table 8. The average voltage and current values of Table 8 are collected by extracting the average term while reading the nominal voltage/current values provided by the accelerator set up during each conveyor passage.

Table 8 Calorimeter first batch Experimental Data.

Test Nominal Values	Total Average ΔT	$\frac{\Delta T}{\#\ pass}$	Average Experimental Current	Average Experimental Voltage	Corrected Energy
$MV, mA, \#$	K	K	mA	MV	keV
1, 10, 3	29.65	9.88	10.27	1.0033	735 ± 17
0.8, 10, 3	23.06	7.69	10.33	0.8067	571 ± 16
0.6, 10, 3	15.74	5.25	10.37	0.6067	392 ± 15
1, 5, 6	29.64	4.94	5.18	1.0083	728 ± 31
0.8, 5, 3	11.95	3.98	5.2	0.8067	588 ± 30
0.6, 5, 6	15.55	2.59	5.18	0.6	388 ± 29
1, 10, 1	9.9	9.9	10.6	1	713 ± 16

Data Processing

In this section we collect all the data derived from the experimental tests and we discuss about the experimental results. Through these data we want to understand the accelerator properties: the effective energy of impinging electrons, and the accelerator behavior.

In Figure 59 we report all the measurements conducted during the experimental phase. At first we would like to see if there is a trendline that include all the collected data, as plotted in Figure 60, where we also compare the analytical equation (8) with the experimental data. In fact, looking at Figure 59, we can observe that there may be seen two linear trends: the first one covers the first three markers ($5\ mA$), and the second one the remaining markers ($10\ mA$), as shown in Figure 62.

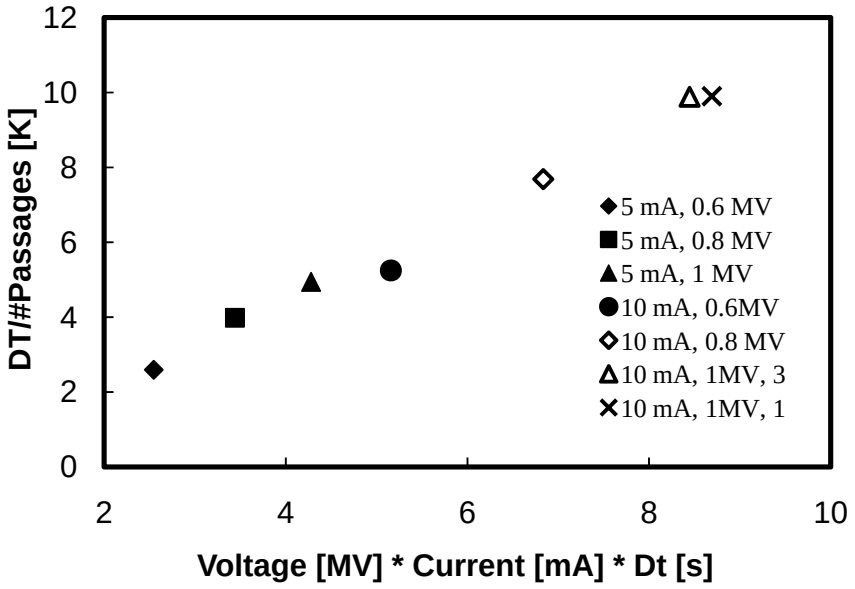

Figure 59 – Collection of the experimental data. Each test has a different marker, as shown in legend (accelerator nominal settings).

In Figure 60 we sketch the experimental data trend and the analytical one, whose expression comes from (8), where the calorimeter parameters are inserted, obtaining (16).

$$y = 1.6687x \qquad (16)$$

It is obvious from the sketch of Figure 60 that the two lines are not parallel. Nevertheless we notice that the accelerator follows a linear trend, described by equation (17):

$$y = 1.1855x - 0.3531 \qquad (17)$$

The comparison between the analytical ideal expression and the experimental data of Figure 60 shows a lower ΔT value for the real model than the predicted one. This event is due to the two different approaches: the ideal expression does not take into account air and titanium window losses, while comparing the round and square markers we could evaluate this term. We can also observe that the air and titanium energy loss contribute is not a constant, but it is different for each experimental point, and it varies over the selected nominal current and voltage values.

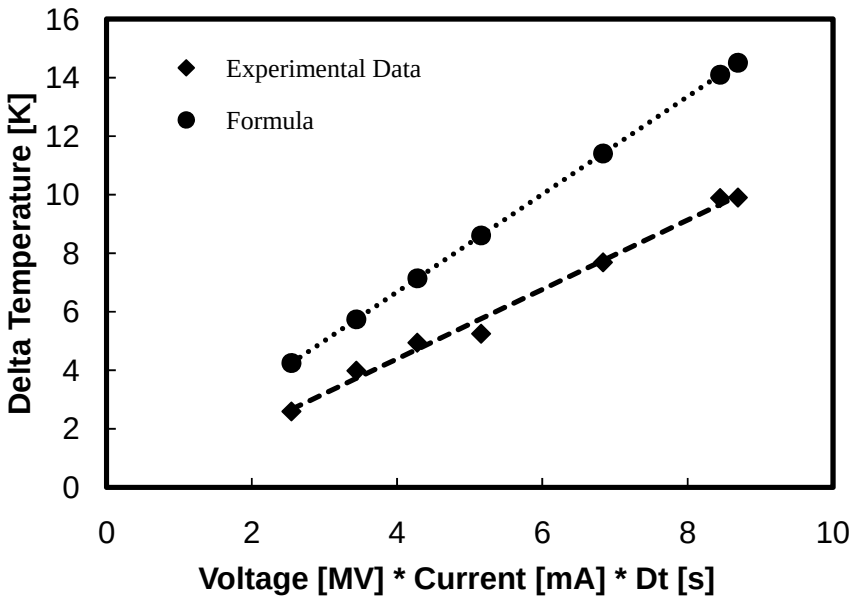

Figure 60 – Comparison between analytical ideal expression (16) and the whole experimental data trendline.

In Figure 61 we extend the experimental linear interpolation to the accelerator upper limit condition, i.e. working conditions range (70 kW). From this plot we want to highlight that once the average temperature difference is known, through equation (17), we can

extrapolate the accelerator variables product (voltage, current, time) in the case of linear precision.

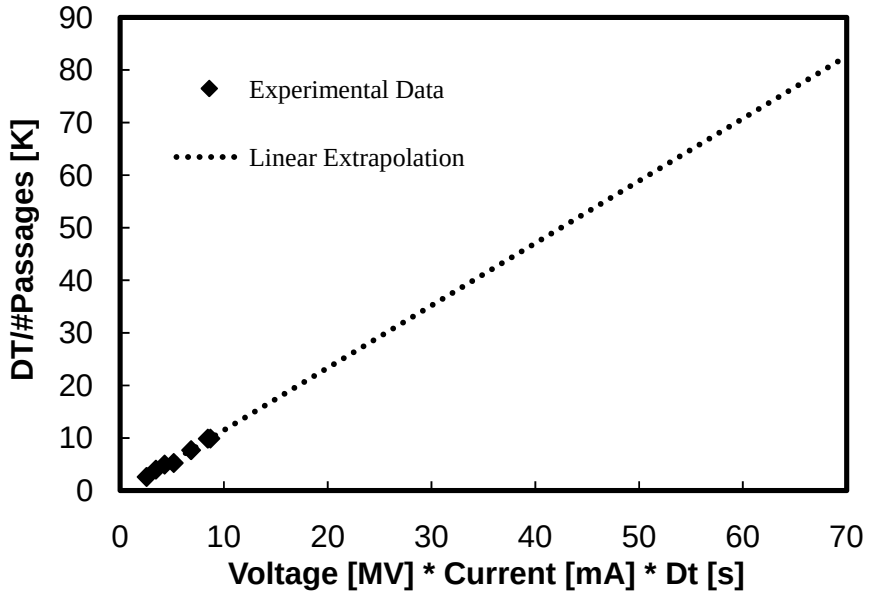

Figure 61 – Extension of the experimental data in a linear extrapolation to the accelerator upper limit condition (70 kW).

In Figure 62 we try to compare the 5 mA and 10 mA (nominal values) data together and with the analytical expression; the difference between the experimental and the analytical ΔT give an estimate of the air and titanium energy losses. As with the inclusive linear interpolation, also in this case the trends defined by the two different currents are not parallel to the mathematical expression, but we may assume that they are almost parallel to each other, as their expressions are: $y = 1.3574x - 0.8062$ (5 mA), and $y = 1.3478x - 1.6364$ (10 mA), where the slopes identify approximately the same value. With this remark we want to stress the fact that the accelerator non-linear behavior is very likely due to its unusual current regime, as the slope depends to the applied current value.

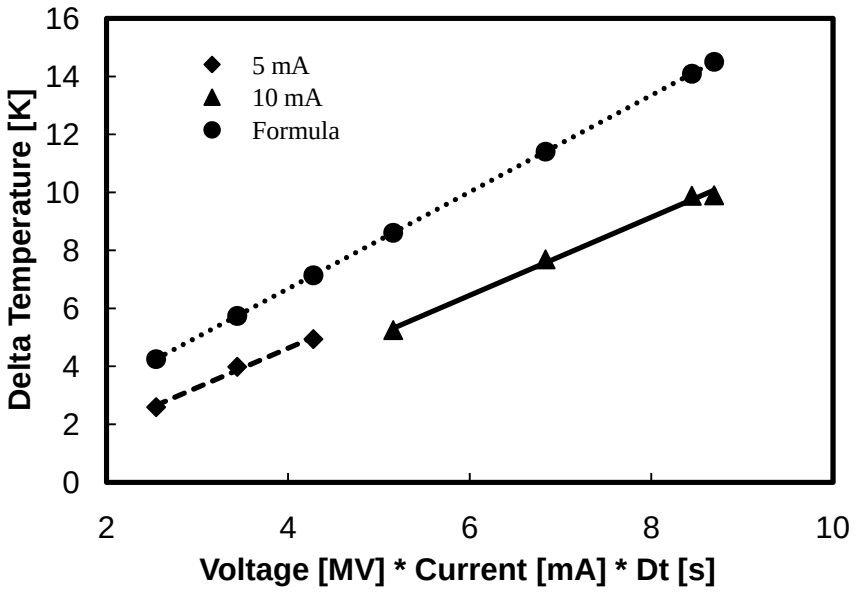

Figure 62 – Comparison between experimental data trendline and analytical ideal expression (16).

Finally in Figure 63 we plot the correlation between the imposed beam energy value and the measured one. The derived electron beam energy holds the contribute of both the directly calorimeter measurement and the estimated error corrections. The difference between the imposed and the corrected values varies from 27% (1 MeV), to 35% (0.6 MeV).

The lower evaluation of the electron beam energy is one of the most important results of the entire experiment: the imposed beam energy does not represent the same energy value at which cables are irradiated for the crosslinking processes. As a matter of fact during the tests the calorimeter is irradiated instead of cables and it detects the same electron energy that cables receive while they are irradiated. With this knowledge we are able to characterize the radiation source, so that we may possibly make more suitable corrections on the accelerator parameters to obtain expected results for the required application needs.

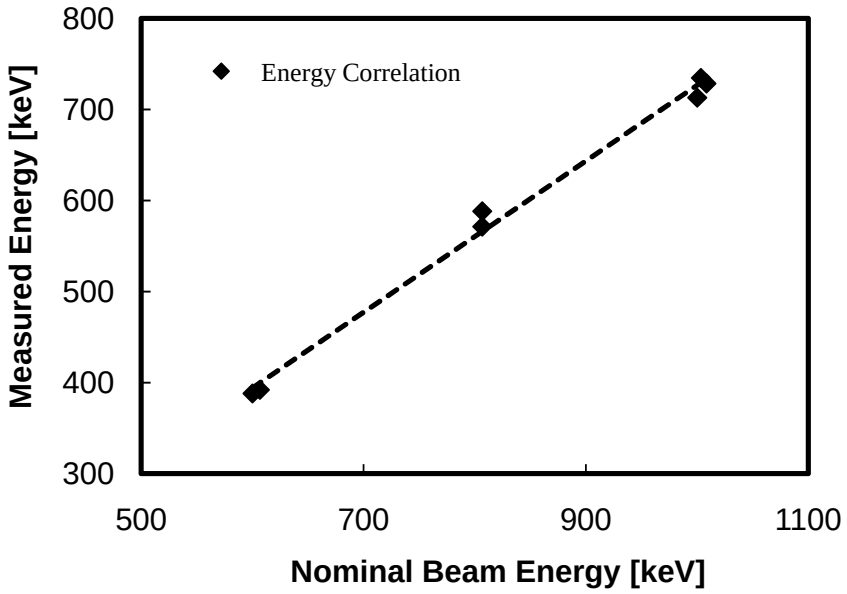

Figure 63 – Energy correlation between the imposed beam energy and the measured one (energy detected by the calorimeter and corrected through the error parameters).

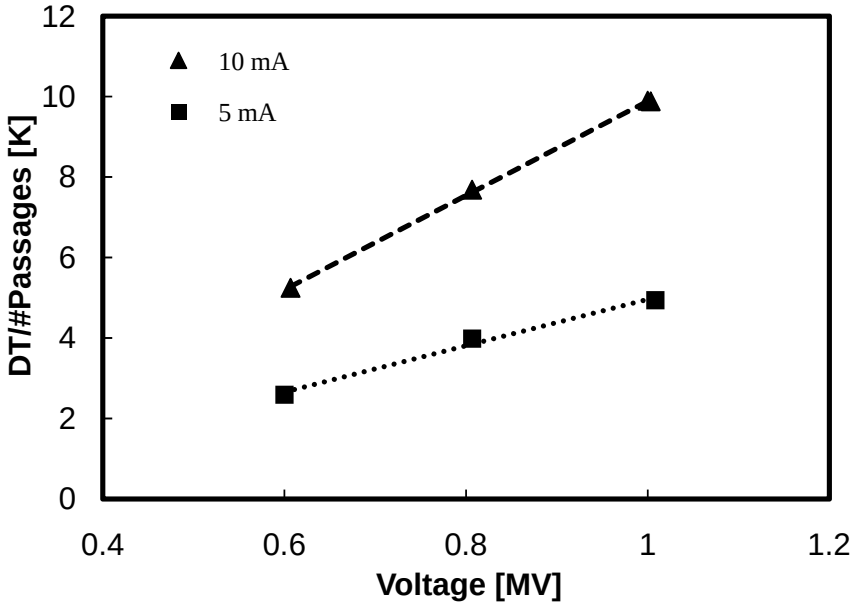

Figure 64 – Experimental difference of temperature versus the beam voltage (nominal beam currents).

In Figure 64 we represent the experimental difference of temperature versus the imposed beam voltage. The two curves describe the accelerator behavior at $5\,mA$ and $10\,mA$ (nominal values). As these current values are one the double of the other, we expect the lines to have a double slope. This event does not exactly happen, even though we may deduce that if the current doubles, the proportion becomes $1:2.0365$. The mathematical relations are: $y = 5.7551 - 0.7945$ $(5\,mA)$ and $y = 11.72x - 1.813$ $(10\,mA)$.

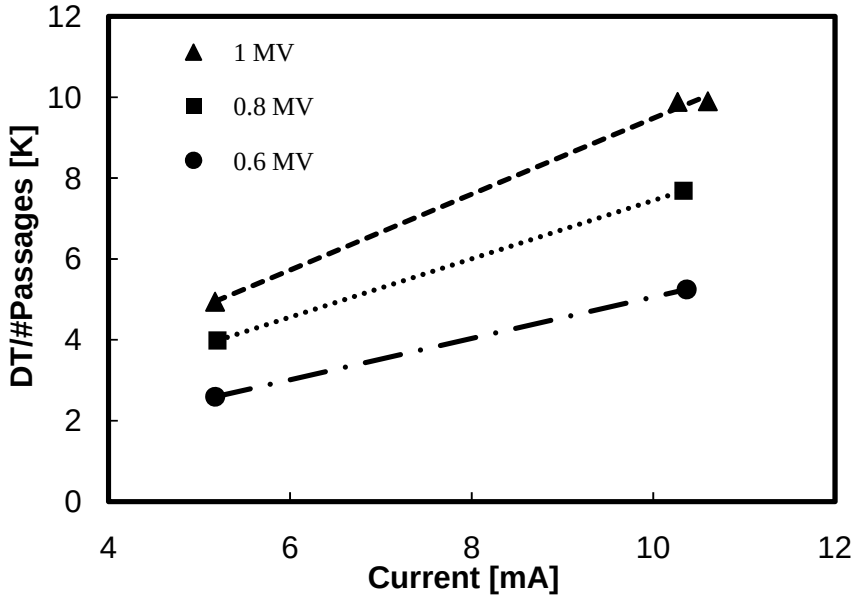

Figure 65 – Experimental difference of temperature versus the beam current (nominal beam voltages).

Eventually in Figure 65 we sketch the experimental difference of temperature versus the beam current. The mathematical expressions derived by Figure 65 are: $y = 0.939x + 0.0901$ $(1\,MeV)$, $y = 0.7214x + 0.2319$ $(0.8\,MeV)$, and $y = 0.5114x - 0.0548$ $(0.6\,MeV)$. In this case the slope is represented by a coefficient whose different parameter for each energy case is namely the beam voltage, as the other factors describe the calorimeter system (recalling analytical expression (8)). For this reason the ratios among the slopes should be the same of the ratios among the three beam voltages, if the accelerator had a defined proportional law. This proportion is not really observed, as we can see in Table 9.

Table 9 Slope ratios of Figure 65 compared to voltage ratios.

Beam Voltage MV	Slope K/A	Voltage Ratio	Slope Ratio	Difference %
1	0.939	0.8	0.7683	3.97
0.8	0.7214	0.75	0.7089	5.48
0.6	0.5114	0.6	0.5446	9.23

From Table 9 we can notice that there is not a well defined proportional law ratio that relates the voltages to the slopes, even though from Figure 65 we see the three different slopes associated to the three different applied beam voltages.

In the end we may assert the calorimeter linearity and the non-linear accelerator behavior probably due to the fact that the accelerator is working in a non usual current regime.

Experiment Reproducibility

As our calorimeter is an original tool, we want to test its reproducibility: we have repeated some experiments, and got proof that the differences between the first and the second batch of measures are almost negligible.

In Figure 66 we plot the new carried out tests: we want to highlight that we do not need to prove the accelerator linearity with different beam currents anymore, so that we only perform one measurement at 5 mA with 1 MV beam voltage; the other three measures have the same 10 mA beam current with the three different beam voltages: 0.6 MV, 0.8 MV, and 1 MV.

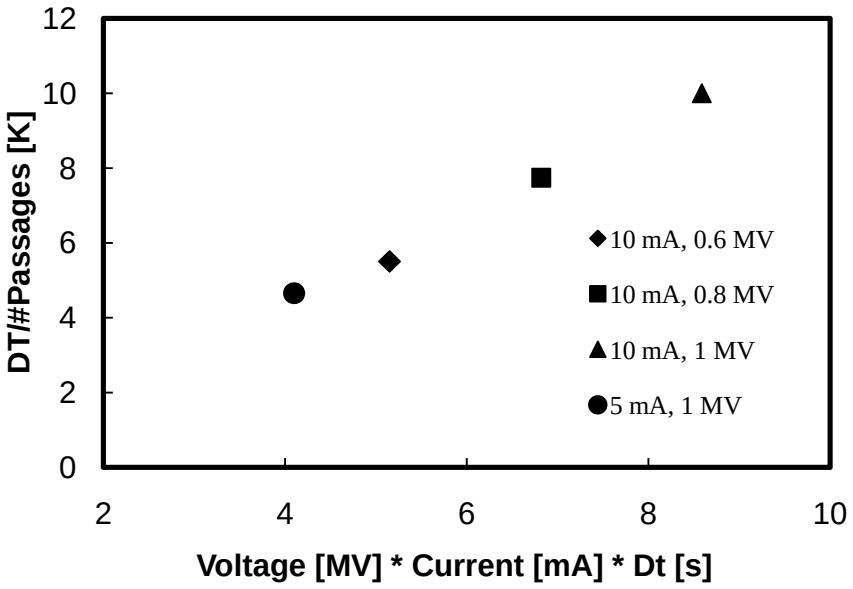

Figure 66 – Collection of the second experiment data. Each test has a different marker, as shown in legend (nominal values).

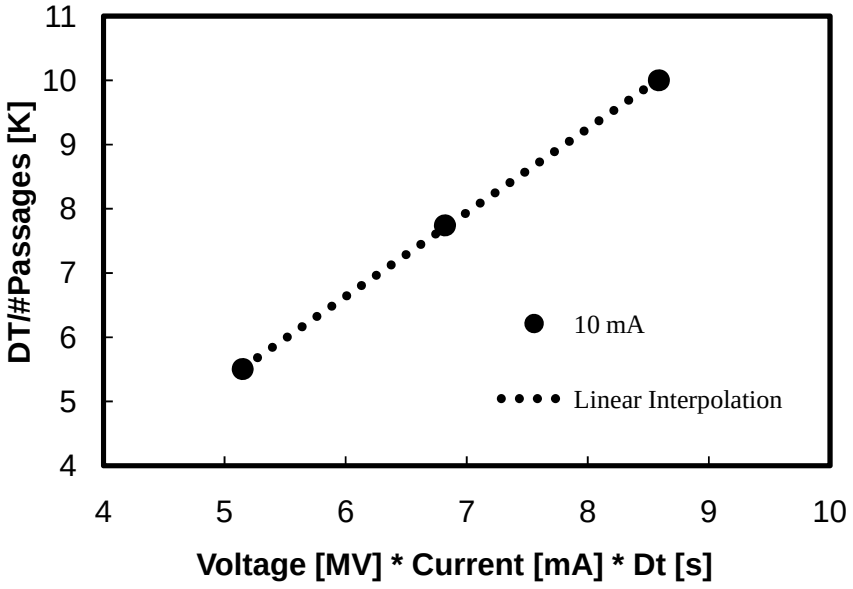

Figure 67 – Focus on the 10 mA beam current data with further representation of linear interpolation.

In Figure 67 we want to highlight the good match for the linear interpolation at 10 mA beam current. In this experiment the three markers match the linear interpolation perfectly well, confirming the calorimeter linearity.

Always focusing on the 10 mA experiments, in Figure 68 we plot the correlation between the nominal electron beam energy and the detected energy at the calorimeter surface. In Figure 68 we can deduce the detected energy from the nominal beam energy through the linear interpolation. We can also observe that the energy losses due to the electron path from the radiation source through air and titanium window let the detected energy be from 25% (1000 keV) to 31% (600 keV) less than the nominal value.

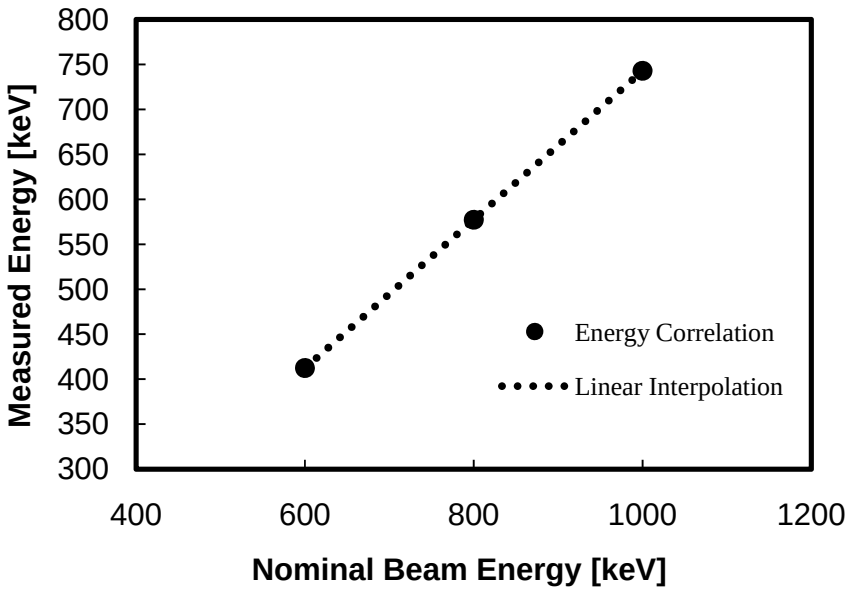

Figure 68 – Measured average electron energy at the calorimeter surface (after systematic errors correction) as a function of the nominal electron beam energy.

All the experimental data and the estimated energy values collected during the second batch of experiments are summarized in Table 10.

Table 10 Calorimeter second batch Experimental Data.

Test Nominal Values	Total Average ΔT	$\frac{\Delta T}{\#\ pass}$	Average Experimental Current	Average Experimental Voltage	Corrected Energy
$MV, mA, \#$	K	K	mA	MV	keV
0.6, 10, 4	22	5.5	10.34	0.6078	412 ± 16
0.8, 10, 4	30.97	7.74	10.3	0.8075	577 ± 16
1, 10, 3	30	10	10.27	1.02	743 ± 17
1, 5, 3	13.97	4.66	4.92	1.017	722 ± 32

Results & Discussion

The calorimeter experimental tests presented above show that our system has been successfully designed for the considered energy and current electron ranges. As seen from the previous data and graphs, the final result of the experimental phase lies in lower accelerator electron beam energies, if compared to the nominal set-up values. The reproducibility of the system has also been verified with two batches of experiments, proving the extrapolation of compatible temperatures and doses.

Through the collected temperature data and equation (7), we are able to trace back the average absorbed dose value in the aluminum calorimeter, with which we can calibrate EBXLINK 1D simulator, obtaining the real accelerator energy. After having calibrated the simulator accelerator energy through the calorimeter, energies reported in Table 11, we need a model validation, since our calorimeter has been developed with a new approach. The calorimeter measures proof has been established through data collected by the calorimeter

itself and another original tool, consisting of dedicated polyethylene tablets with thin film dosimeters. The comparison between the energy data detected by the two independent measures (integral dose calorimeter and thin film dosimeters) demonstrates an excellent agreement, as shown in Table 11, proving the calorimeter feasibility for the considered application dose range.

Table 11 Comparison of the Accelerator Electron Beam Energy among the nominal, the calorimeter and the dosimeters values.

Nominal EB Energy	Calorimeter EB Energy	Dosimeter EB Energy
keV	keV	keV
1000	860	875
800	705	700
600	555	530

In Table 11 is represented the most important result of all the measurements: the real accelerator electron beam energy has a lower value than the nominal one, whose energy difference can be estimated within 12.5%. For the optimization of wires and cables crosslinking this result must be seriously taken into account, if higher performances for special industrial applications (aero-space, solar cells, railway, automotive) must be reached.

The results of this thesis have been published in the paper "*Experimental Extraction of Accelerator Parameters for Accurate Model Calibration in the Numerical 3D Simulation of Electron Beam Crosslinking of Cables and Wires*" by M. Ciappa, L. Mangiacapra, A. Lupi, (extended abstract in Appendix – A.4) which has been accepted for presentation at the "9th Ionizing Radiation & Polymer Symposium", October 25-29, 2010, College Park (MD), USA.

Expanded Polystyrene Overheating

After several passages under the electron beam, we notice that the EPS layer in the wooden box has been modified, as we can see in Figure 69. For this reason we investigate the causes of the heating dissipation, as it seems that some EPS parts have reached a very high temperature, so that they melt and become yellow. Through Monte Carlo simulations at $1\ MeV$ beam energy and $10\ mA$ beam current, we carry out the Absorbed Dose profile in an EPS block with $30\ cm$ thickness, presented in Figure 70. As we can see from the absorbed dose trend, the dose peak value is $D_{peak} = 52.4\ kGy$, reached at $6.15\ cm$ thickness.

Figure 69 – Expanded Polystyrene melting after several passages under the electron beam. The consequences of the radiation can be seen in the yellow ocher color of EPS and in the four melted zones around the aluminum calorimeter.

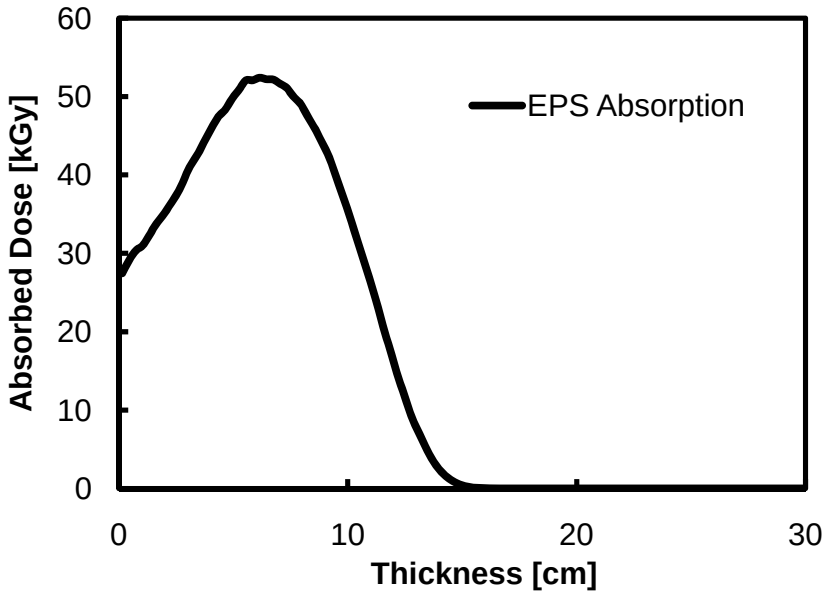

Figure 70 – EPS Absorbed Dose profile of a 30 cm thick layer at 1 MeV and 10 mA beam conditions.

Starting from the dose data we make the conversion into the punctual temperature profile (through EPS specific heat capacity), as shown in Figure 71. We can observe that the delta temperature peak is $\Delta T_{peak} = 39.1\,K$. This value is extremely important, because if the calorimeter continues to pass under the electron beam without any pauses, some plastic zones may reach very high temperatures and may melt.

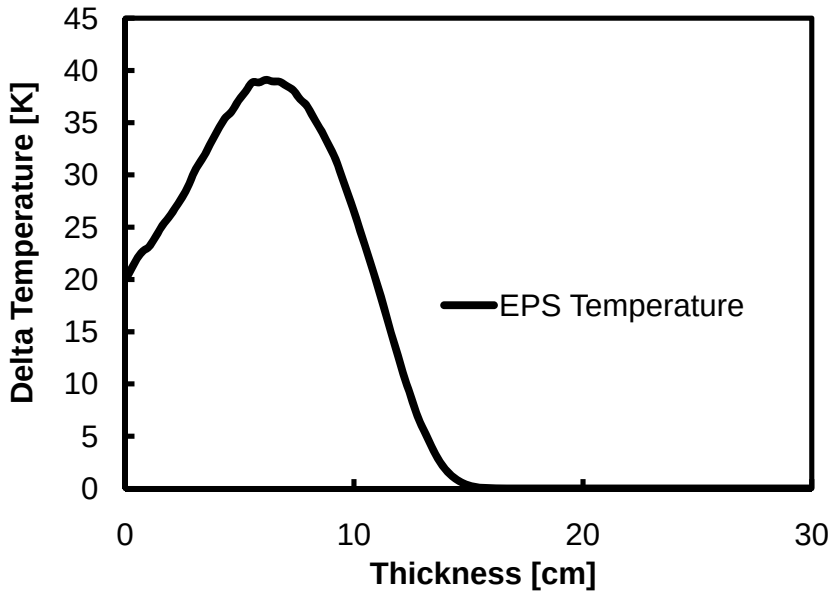

Figure 71 – EPS Temperature profile of a 30 cm thick layer.

As our model does not only consist of EPS (calorimeter sides), we run another simulation more similar to our sample: it consists of 3 cm EPS layer and 1 cm graphite layer (in the real model there is the wooden bottom box). These results are plotted in Figure 72. We choose the graphite, because it has a behavior close to wood, above all for the backscattering properties. From Figure 72 we can see that the dose peak is reached in graphite and that the EPS behavior is very similar to the case only consisting of EPS (Figure 70). In the EPS and graphite model, the dose peak in expanded polystyrene is $D_{peak} = 41.56\, kGy$, to which corresponds a delta temperature peak $\Delta T_{peak} = 31\, K$. This evaluation makes us aware that if the calorimeter box passes for instance 10 times under the accelerator, the delta temperature peak reaches $\Delta T_{peak} = 310\, K$, that means complete polystyrene melting in the interested zones.

Therefore we decide to impose a limit of almost consecutive passages under the radiation source of six times, so that the maximum temperature increase is around $200\, K$.

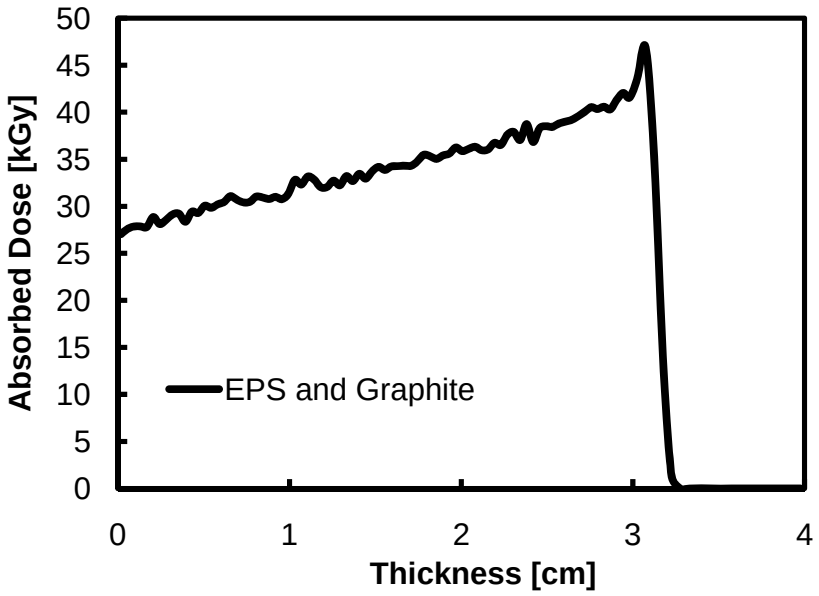

Figure 72 – Absorbed Dose profile in a 3 cm EPS layer followed by a 1 cm graphite layer at 1 MeV and 10 mA beam conditions.

Conclusions

The entire work focuses on the modeling and development of an aluminum integral dose calorimeter for polymers crosslinking, whose design and test deal with dosimetry measurements at $0.5 - 2\ MeV$ electron beam energy range.

Our investigations and analyses prove that our calorimeter has been successfully designed meeting the specifications for the examined industrial environment. The most important result consists of the quite high difference between the imposed beam energy and the detected one, meaning that the radiation energy detected by the cable during the crosslinking process is lower than the expected one, causing loss in performances, if this correction is not adequately taken into account.

To give evidence of our analyses, we compare the calorimeter measurements with another original tool composed of dedicated polyethylene tablets with thin film dosimeters. The comparison between the energy data detected by the two independent measures demonstrates an excellent agreement, proving the calorimeter feasibility for the considered application dose range and lower electron beam energy than the nominal one.

With the knowledge of the real electron beam energy value and the accelerator behavior we are able to characterize the radiation source, so that we can make more suitable corrections on the imposed accelerator parameters to obtain appropriate results for the required application field.

The prospective improvement of our calorimeter lies in solving some material and mechanical challenges to make the system more suitable to the accelerator physical characteristics: a more compact geometry, the use of screws instead of glue and the radiation resistance improvement of the insulation layer because of the high reached temperatures

(several passages under the radiation source), and a proper system for damping conveyor oscillations.

Another possible step for the calorimetric measurements enhancement consists of finalizing the water calorimeter as an absolute reference, since it has already been designed and it only requires assembly and testing.

The future development of our integral dose calorimeter may be based on analyses and tests of new radiation sources at higher beam current levels, whose properties are requested for more accurate industrial processes, such as cables and wires crosslinking.

Our integral dose calorimeter has the potential of being developed into a standard for electron accelerator characterization, performance, and maintenance in industrial environment.

The results of this thesis have finally been published in the paper “Experimental Extraction of Accelerator Parameters for Accurate Model Calibration in the Numerical 3D Simulation of Electron Beam Crosslinking of Cables and Wires” by M. Ciappa, L. Mangiacapra, A. Lupi, (extended abstract in Appendix – A.4) which has been accepted for presentation at the “9th Ionizing Radiation & Polymer Symposium”, October 25-29, 2010, College Park (MD), USA.

Appendix – A.1

CSDA Graphs

When dimensioning the calorimeter, we use as an important parameter the CSDA (Continuous Slow Down Approximation) electron range, which is a calculated quantity that represents the mean path length along the electrons trajectory. In the following graphs we plot the CSDA range for the different materials that we needed for our analysis from $0\ MeV$ to $10\ MeV$, i.e. graphite in Figure 73, aluminum in Figure 74, copper in Figure 75, polyethylene (PE) in Figure 76, polystyrene (PS) in Figure 77, and mylar in Figure 78. All the data are collected through ESTAR software developed by NIST (National Institute of Standards and Technology – Physics Laboratories).

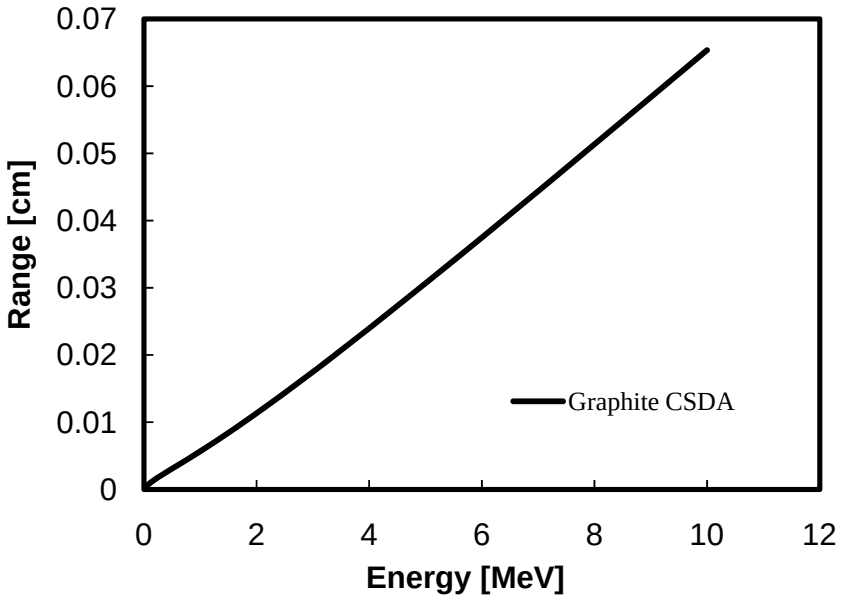

Figure 73 – Graphite CSDA electron range.

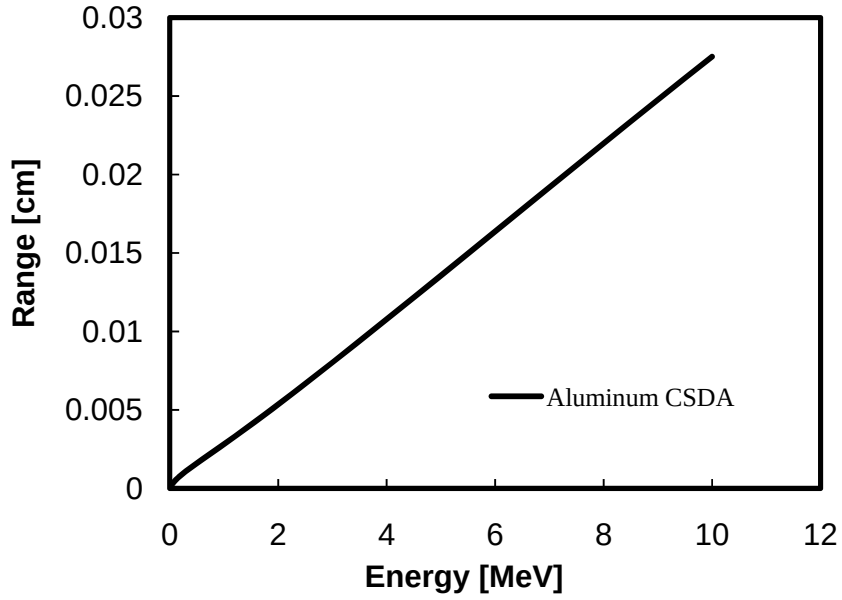

Figure 74 – Aluminum CSDA electron range.

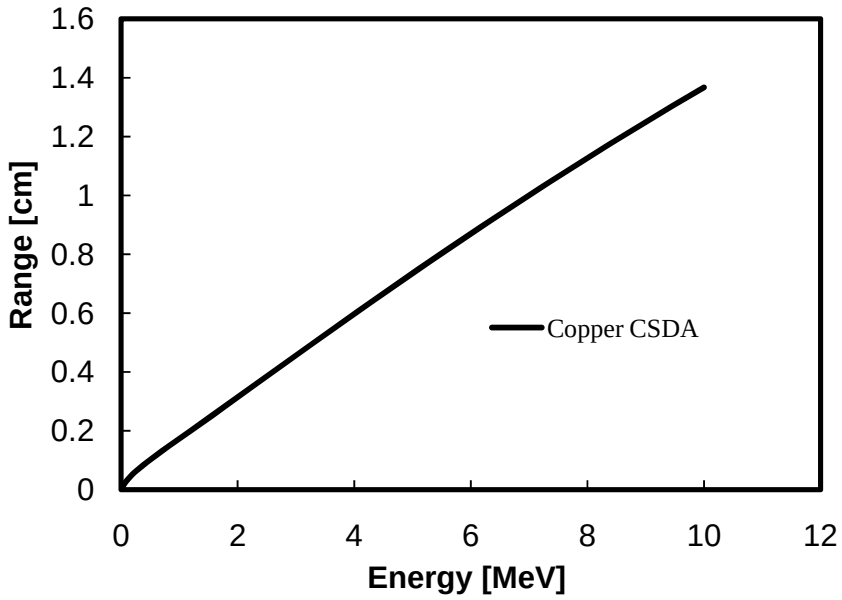

Figure 75 – Copper CSDA electron range.

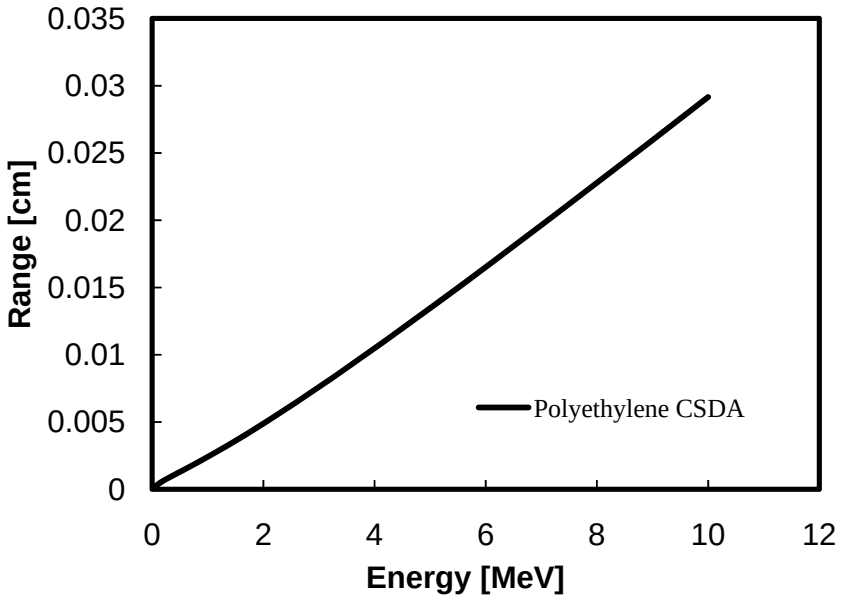

Figure 76 – Polyethylene (PE) CSDA electron range.

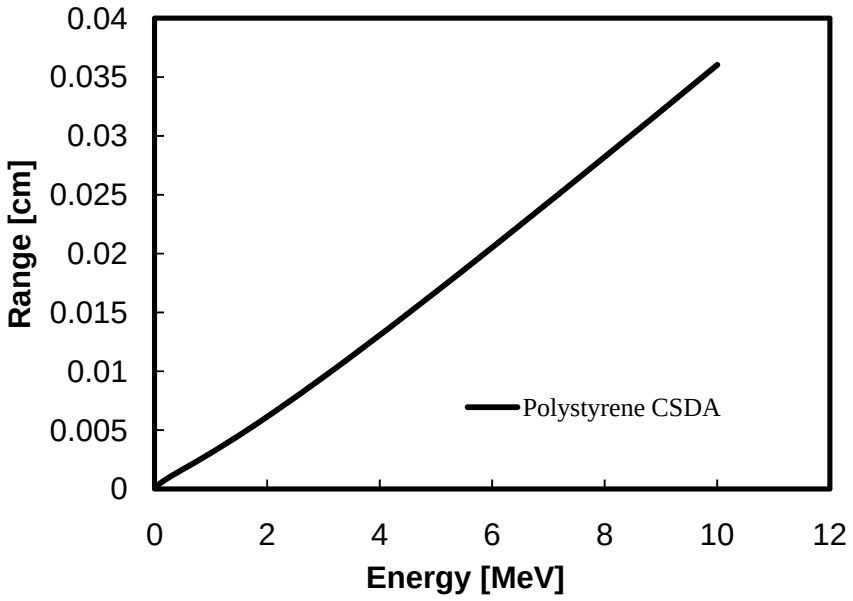

Figure 77 – Polystyrene (PS) CSDA electron range.

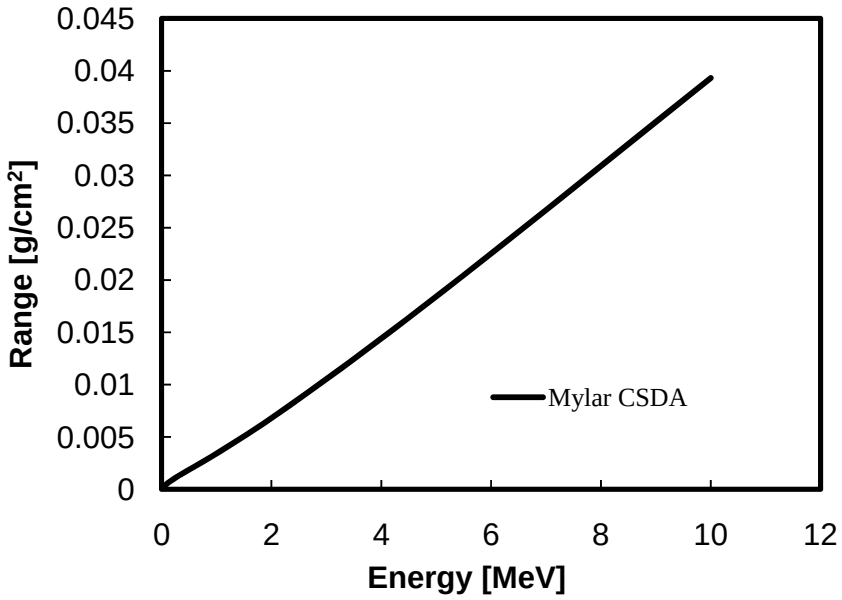

Figure 78 – Mylar CSDA electron range.

Appendix – A.2

Calorimeter Cad Plots

In this appendix we enclose all the significant sketches that we used for the calorimeter structure that has been built at the mechanical workshop. All the plots have been made through Ansys WB Design Modeler [1].

In Figure 79, Figure 80, Figure 81, and Figure 82 we give the sketches of the different model parts separately. All the measures reported are in millimeters.

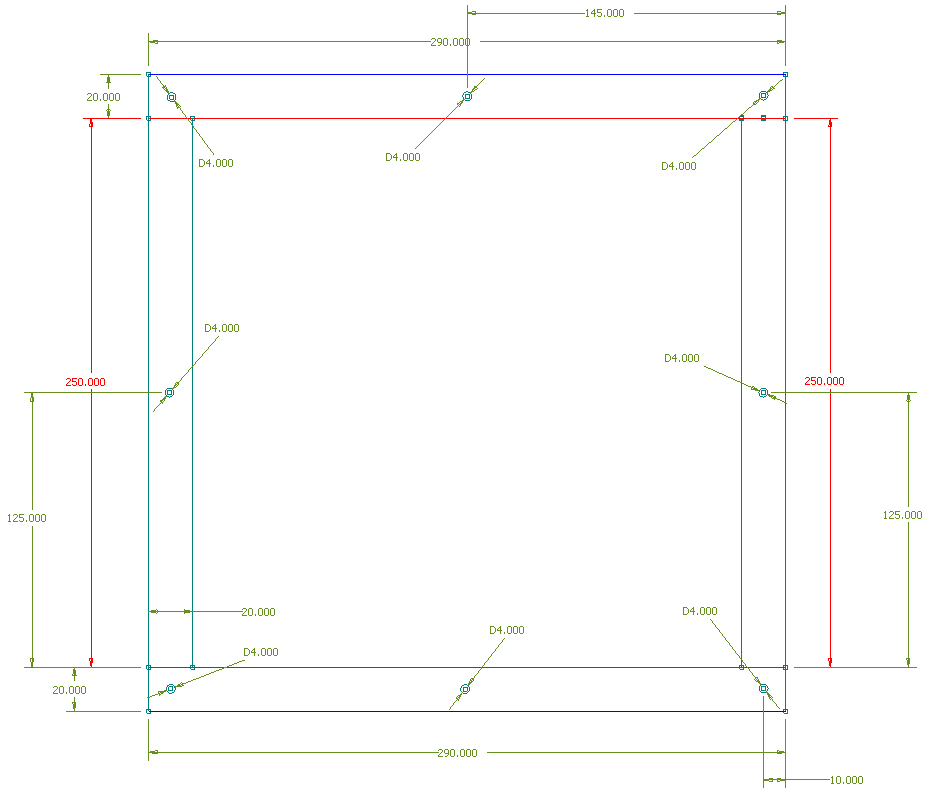

Figure 79 – Plan of the wooden box where the entire calorimeter is inserted, with all the side measures and the hole measures for the screws. This plan plot also represents the frame wooden lid.

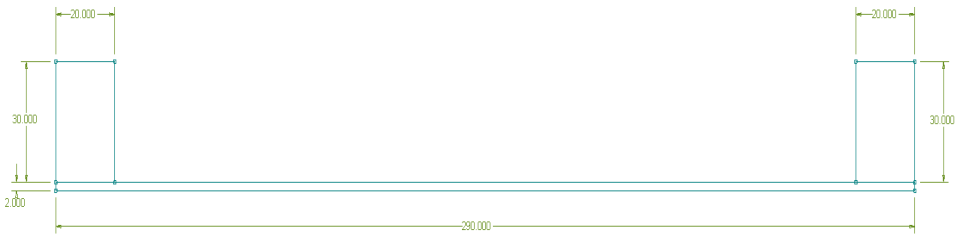

Figure 80 – Wooden box prospect.

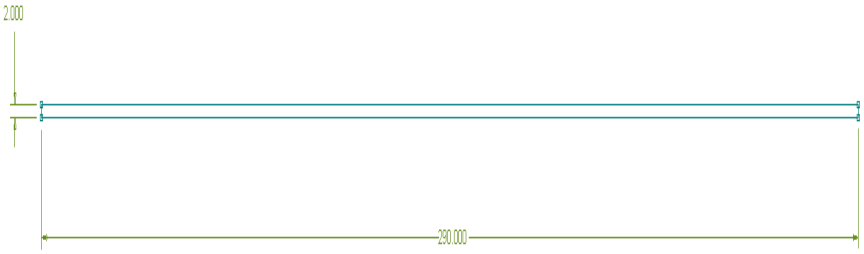

Figure 81 – Wooden frame lid prospect.

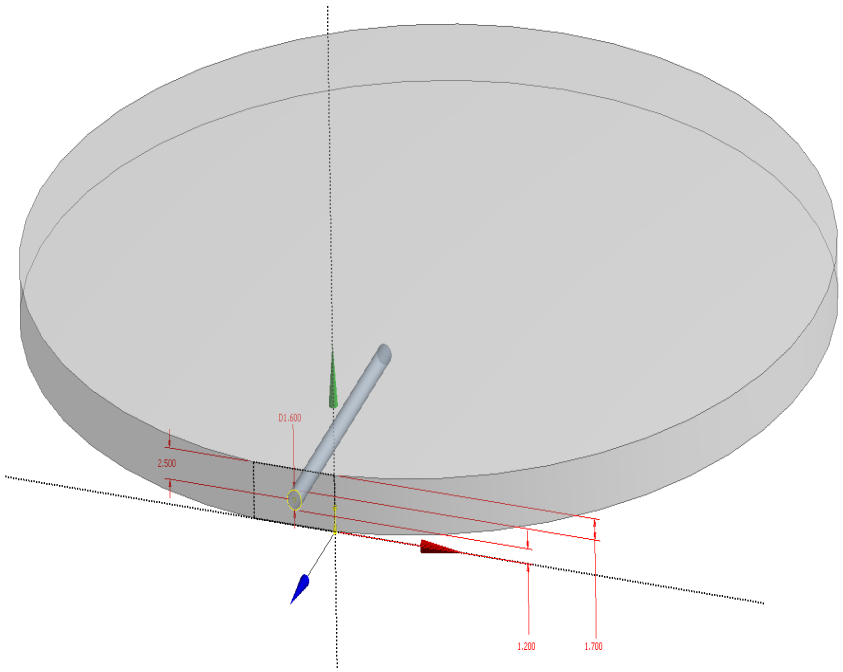

Figure 82 – Aluminum Calorimeter representation with the 3 cm length hole for the capillary where it is inserted the Micro-BetaCHIP thermistor.

In Figure 83 we report the plot of the entire calorimetric system without mylar foil cover.

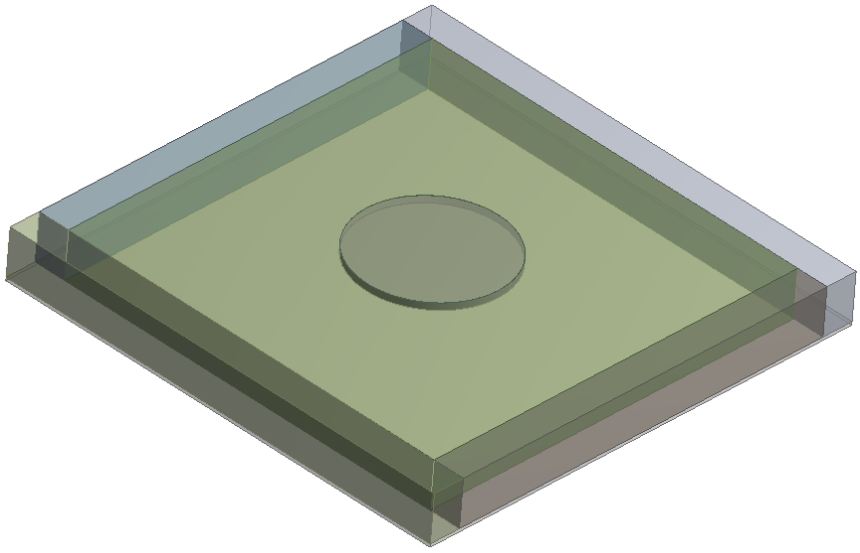

Figure 83 – Three dimensional view of the entire calorimetric system: wooden box, EPS insulation (inside the box), and the aluminum absorber, represented by the cylinder in the middle of the model.

Appendix – A.3

Matlab file

As previously written in Chapter 4, our Matlab file is a mean to establish the energy of impinging electrons taking into account energy errors and losses due to the designed system (mylar absorption, electron backscattering, boundary escapes, Bremsstrahlung emission, Micro-BetaCHIP tolerance, interpolation error).

In the Matlab file we also decide to evaluate the average dose deposed by the electron beam. As the dose is entirely deposited within the CSDA range, we need to rearrange equations presented in Chapter 1, as follows in equation (18):

$$\Delta T_{CSDA} = \Delta T_{TOT} \cdot \frac{t_{TOT}}{t_{CSDA}} \qquad (18)$$

where ΔT_{CSDA} is the difference of temperature within the CSDA range $[K]$, ΔT_{TOT} is the total difference of temperature $[K]$, t_{TOT} is the total calorimeter thickness $[cm]$, and t_{CSDA} is the calorimeter CSDA thickness $[cm]$.

And the average dose is given in (19).

$$\overline{D}_{CSDA} = \frac{E_{TOT}}{m_{CSDA}} = \frac{C_p \cdot t_{TOT} \cdot \rho \cdot \Delta T_{TOT}}{\rho \cdot t_{CSDA}} = \frac{C_p \cdot t_{TOT} \cdot \Delta T_{TOT}}{t_{CSDA}} \qquad (19)$$

where $\overline{D}_{CSDA}$ is the average dose value within the CSDA $[kGy]$, E_{TOT} is the total absorbed energy $[J]$, m_{CSDA} is the mass defined by CSDA range $[g]$, C_p is the material specific heat capacity $\frac{J}{g \cdot K}$, and ρ the material density $\frac{g}{cm^3}$.

In Table 12 we collect all the dose data derived by (19) for the different experiments.

Table 12 Average Absorbed Dose values of the experimental tests.

Test	Average Dose
$MV, mA, \#$	kGy
1, 10, 3	29.06
0.8, 10, 3	31.46
0.6, 10, 3	36.26
1, 5, 6	14.68
0.8, 5, 3	15.68
0.6, 5, 6	18.17
1, 10, 1	30.26

In the following lines we attach the Matlab script.

```
clc
clear all;


% Program to compute the Absorbed Energy value within the Aluminum
Calorimeter

%************************************************************************
% INPUT Measured Temperature Difference
%************************************************************************

delta_T = 9.9;                                  % Temperature Difference [K]

%************************************************************************


%************************************************************************
% INPUT Electron Beam Parameters
%************************************************************************

E_acc = 1;                                       % Energy Accelerator [MeV]
t_tran = 0.82;                                   % transit time [s]
beam_curr_mA = 10.6;                             % beam current [mA]
A_irr = 540;                                     % Irradiated Area [cm2]

%************************************************************************
```

```
%************************************************************************
% INPUT Calorimetric System Parameters
% ************************************************************************

roAL = 2.71;                                % density [g/cm3]
CpAL = 0.9;                                 % spec. heat Aluminum [J/(g K)]
t_cal = 0.45;                               % cal thickness [cm]

% ************************************************************************


% ************************************************************************
% OUTPUT: Measured Energy without corrections (Ideal)
% ************************************************************************

display('*****************************************************************');
display('Non Correctrd Acceleration Energy from Calorimeter [keV]');
display('*****************************************************************');

E_cal_ideal = delta_T* roAL * t_cal * CpAL *A_irr/ ( beam_curr_mA * t_tran
)   % [keV]

% ************************************************************************


% ************************************************************************
%  Mylar films Correction
% ************************************************************************

display('*****************************************************************');
display('Correction for Mylar Absorption [keV]');
display('*****************************************************************');

E_Loss_M_6um  =  0.0502*E_acc^6  -  0.5607*E_acc^5  +  2.5471  *  E_acc^4  -
6.0688*E_acc^3 + 8.1083*E_acc^2 - 5.851*E_acc + 4.357    % Energy Loss in
mylar [keV]

% ************************************************************************


% ************************************************************************
% Backscattering Correction
% ************************************************************************

display('*****************************************************************');
display('Correction  for  Energy  Loss  due  to  Electron  Backscattering
[keV]');
display('*****************************************************************');

E_backsc_per  =  0.0407*E_acc^4  -  0.4136*E_acc^3  +  1.9788*E_acc^2  -
5.4835*E_acc + 7.9465;                  % %Backscattering energy loss [%]

E_backsc_p = E_backsc_per/100;          % %Backscattering energy loss [%]
```

```
Backscattering_Loss_keV = E_backsc_p*E_cal_ideal   % Backscattering energy
loss [keV]

% ************************************************************************


% ************************************************************************
% Boundary Correction
% ************************************************************************

display('************************************************************');
display('Correction for Energy Loss due to Boundary Escapes [keV]');
display('************************************************************');

E_bound_p = -0.01;                                  % -1% Boundary Energy
Loss [%]
Boundary_Loss_keV = E_bound_p*E_cal_ideal          % Boundary energy loss
[keV]

% ************************************************************************


% ************************************************************************
% Bremsstrahlung Correction
% ************************************************************************
display('************************************************************');
display('Correction for Energy Loss due to Bremsstrahlung [keV]');
display('************************************************************');

E_brems_p = 0.01;                                    % 1% Bremsstrahlung
Energy Loss [%]
Bremsstrahlung_keV = E_brems_p*E_cal_ideal        % Bremsstrahlung energy
loss [keV]

% ************************************************************************


% ************************************************************************
% Total percentage Energy Loss
% ************************************************************************
display('************************************************************');
display('Total Energy Correction [keV]');
display('************************************************************');

Total_Energy_Loss    =    E_Loss_M_6um    +    Backscattering_Loss_keV    +
Boundary_Loss_keV + Bremsstrahlung_keV

display('Total Energy Correction [%]');
tot_p = Total_Energy_Loss / E_cal_ideal * 100        % %Total energy loss
[%]

% ************************************************************************
```

```
% ************************************************************************
% OUTPUT: Final Energy Value
% ************************************************************************

display('************************************************************');
display('Corrected Beam Energy Value without statistical errors [keV]');
display('************************************************************');

E_cal_final = E_cal_ideal + Total_Energy_Loss     % Corrected Energy [keV]

% ************************************************************************

%************************************************************************
% Betatherm Energy Loss
%************************************************************************

display('************************************************************');
display('Stocastic Betatherm Error [keV]');
display('************************************************************');

T_err = 0.2;                              % Temperature error thermistor [K]
E_betatherm = T_err* roAL * t_cal * CpAL *A_irr/ ( beam_curr_mA * t_tran )
% [keV]

% ************************************************************************



% ************************************************************************
% Interpolation Correction
% ************************************************************************

display('************************************************************');
display('Stocastic Interpolation Error [keV]');
display('************************************************************');

E_interp_p = 0.004;                                  % 0.4% Interpolation
Energy Loss [%]
Interpolation_keV = E_interp_p*E_cal_ideal

% ************************************************************************

display('************************************************************');
display('Stocastic Sum Error [keV]');
display('************************************************************');
sum = Interpolation_keV + E_betatherm

% ************************************************************************
% OUTPUT: Final Average Dose CSDA
% ************************************************************************

display('************************************************************');
display('Electron Beam Energy [MeV]');
display('************************************************************');
```

```
Eb = E_cal_final/1000                          % Energy beam [MeV]

CSDA_Energy_trasp = [3.000E-01 1.083E-01,
3.500E-01 1.361E-01,
4.000E-01 1.652E-01,
4.500E-01 1.952E-01,
5.000E-01 2.260E-01,
5.500E-01 2.575E-01,
6.000E-01 2.894E-01,
7.000E-01 3.545E-01,
8.000E-01 4.206E-01,
9.000E-01 4.874E-01,
1.000E+00 5.546E-01,
1.250E+00 7.231E-01,
1.500E+00 8.913E-01,
1.750E+00 1.058E+00,
2.000E+00 1.224E+00,
2.500E+00 1.550E+00,
3.000E+00 1.869E+00,
3.500E+00 2.183E+00,
4.000E+00 2.491E+00,
4.500E+00 2.794E+00,
5.000E+00 3.092E+00];

CSDA_Energy = CSDA_Energy_trasp';

CSDA_Energy(2,:) = CSDA_Energy(2,:) ./ roAL;

display('************************************************************');
display('CSDA Evaluated Thickness [cm]');
display('************************************************************');

CSDA_Eb = interp1(CSDA_Energy(1,:),CSDA_Energy(2,:),Eb)


display('************************************************************');
display('Average CSDA Dose CSDA Value [kGy]');
display('************************************************************');

D_CSDA = CpAL * delta_T * t_cal / CSDA_Eb             % Average Dose [kGy]

% ************************************************************************
```

Appendix – A.4

Extended Abstract

The results of this thesis have been published in the paper "*Experimental Extraction of Accelerator Parameters for Accurate Model Calibration in the Numerical 3D Simulation of Electron Beam Crosslinking of Cables and Wires*" by M. Ciappa, L. Mangiacapra, A. Lupi, which has been accepted for presentation at the "9th Ionizing Radiation & Polymer Symposium", October 25-29, 2010, College Park (MD), USA.

In this section we attach the extended abstract of the paper.

Experimental Extraction of Accelerator Parameters for Accurate Model Calibration in the Numerical 3D Simulation of Electron Beam Crosslinking of Cables and Wires

Mauro Ciappa [a], Luigi Mangiacapra [a], Alexandra Lupi [a], Maria Stangoni [b], Stefan Ott [b]

[a] **Integrated Systems Laboratory, ETH Zurich, Zurich, Switzerland**
[b] **Wire+Cable Division, R&D, HUBER+SUHNER AG, Pfaeffikon, Switzerland**
Corresponding author: ciappa@iis.ee.ethz.ch

Thanks to the increasing computing power, three-dimensional (3D) numerical simulation tools can be used to define the optimum process conditions in electron beam crosslinking of cables and wires. Nowadays, such complex dosimetry problems are tackled by 3D Monte Carlo simulation techniques, whose accuracy strongly depends among other on the calibration of the models for the final stage of the electron beam accelerator. This paper presents experimental tools and procedures, which have been developed to calibrate the simulation models for applications up to 3 MeV and 70 mA. The considered parameters are the *beam energy*, the *electron fluence*, and the *beam shape*.

The average *electron beam energy* is measured both by comparison of the measured with the simulated electron range and by calorimetry. For this scope, two original tools have been conceived. Dedicated polyethylene tablets have been machined for accurate measurement of the electron range by thin film dosimeters (Fig.1a) and an integral dose calorimeter has been designed for operation in the 0.5-3 MeV energy range (Fig. 1b). The full paper will provide the details about the construction, statistical accuracy, performance, and cross comparison of the measurement results.

The *fluence* along the beam scanning direction has been acquired by thin film dosimeters, which have been mounted at regular spacing on the top of a metal bar. The metal bar has been inserted by a step motor into the irradiation area at constant velocity and perpendicularly to the beam scanning direction. The final paper will provide details about the accuracy of the measurements results, as well as the dependency of the spatial distribution of the fluency on the beam energy.

Finally, the *beam shape* has been characterized by the knife-edge technique. The beam has been swept along the sharp edge of a metal plate and the current flowing to ground has been converted in a time-dependent voltage signal acquired and stored by an oscilloscope. The full paper will present the details about the procedure for extraction of the beam shape from the leading edge of the oscilloscope signal and the dependency of the shape on beam energy and distance from the scanner.

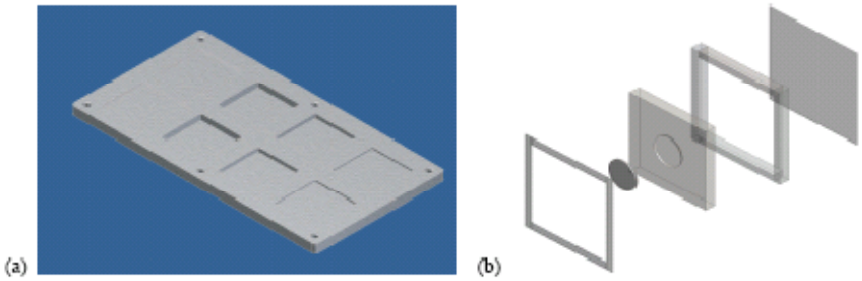

Fig. 1 (a) CAD sketch of the polyethylene tablet machined for the measurement of the average beam energy. (b) Exploded view of the integral dose calorimeter. Both tools are inserted into the irradiation area at constant velocity and perpendicularly to the scanning direction of the beam by a motorized platform.

Bibliography

[1] F. Dadkhah, J. Zecher. *ANSYS Workbench Software Release 12, Tutorial with Multimedia CD.* SDC Publications, 2009.

[2] *Radiation Dosimetry: Electron Beams with Energies Between 1 and 50 MeV.* ICRU Report 35, International Commission on Radiation Units and Measurements, 1984, 14-15, 77-80, 92-95.

[3] *ISO/ASTM 51631 Practice for use of calorimetric dosimetry system for electron beam dose measurements and dosimeter calibrations.* International Standard ISO/ASTM 51631, ISO/ASTM International 2003, 2003.

[4] *Dosimetry Systems.* Report 80, Journal of the ICRU, Vol 8, No 2, 2008, 33-37.

[5] J. S. Laughlin, S. Genna. "Calorimetry." In *Radiation Dosimetry Instrumentation, Vol 2*, by W. C. Roesch F. H. Attix, 389-439. 1966-1972.

[6] A. Miller, A. Kovacs. "Calorimetry at industrial electron accelerators." *Nuclear Instrumentation and Methods in Physics Reseach* B10/11 (1985): 994-997.

[7] I. Janovsky, A. Miller. "A Calorimeter for Measuring Energy Deposition in Materials and Calibrating the Response of Dosimeters Irradiated by Low-Energy Industrial Electron Accelerators." *Applied Radiation and Isotopes* 38, no. 11 (1987): 931-937.

[8] A. Miller, A. Kovacs, F. Kuntz. "Development of a polystyrene calorimeter for application at electron energies down to 1.5 MeV." *Radiation Physics and Chemistry*, 2002: 739-744.

[9] Miller, A. "Polystyrene Calorimeter for Electron Beam Dose Measurements." *Radiation Physics and Chemistry* 46, no. 4-6 (1995): 1243-1246.

[10] A. Miller, A. Kovacs. "Application of Calorimeters for Routine and Reference Dosimetry at 4-10 MeV Industrial Electron Accelerators." *Radiation Physics and Chemistry* 35, no. 4-6 (1990): 774-778.

[11] J. C. Humphreys, W. L. McLaughlin. "Calorimetry of Electron Beams and the Calibration of Dosimeters at High Doses." *Radiation Physics and Chemistry* 35, no. 4-6 (1990): 744-749.

[12] J. Helt-Hansen, A. Miller, S. Duane, P. Sharpe, M. McEwen, S. Cluasen. "Calorimetry for dose measurement at electron accelerators in the 80-120 keV range." *Radiation Physics and Chemistry* 74 (2005): 354-371.

[13] Micro-BetaCHIP Thermistor Probe. "http://www.meas-spec.com/product."

[14] NI ENET-9219. "http://sine.ni.com/nips/cds/view/p/lang/en/nid/205700." *http://www.ni.com/.*